Development of a Magnesium Semi-solid Redox Flow Battery

Matthew McPhail
Vivek Subramanian, Ed.

Electrical Engineering and Computer Sciences
University of California, Berkeley

Technical Report No. UCB/EECS-2022-241
http://www2.eecs.berkeley.edu/Pubs/TechRpts/2022/EECS-2022-241.html

December 1, 2022

Development of a Magnesium Semi-solid Redox Flow Battery

by

Matthew McPhail

A dissertation submitted in partial satisfaction of the

requirements for the degree of

Doctor of Philosophy

in

Engineering - Electrical Engineering and Computer Science

in the

Graduate Division

of the

University of California, Berkeley

Committee in charge:

Professor Vivek Subramanian, Chair
Professor Bryan McCloskey
Professor Ali Javey

Fall 2020

Development of a Magnesium Semi-solid Redox Flow Battery

Abstract

Development of a Magnesium Semi-solid Redox Flow Battery

by

Matthew McPhail

Doctor of Philosophy in Engineering - Electrical Engineering and Computer Science

University of California, Berkeley

Professor Vivek Subramanian, Chair

To combat the effects of global warming, renewable energy sources are desirable but produce power intermittently, greatly limiting their ability to fulfill electricity demand on the grid. Storing energy produced for the grid and dispensing it at a later time would remove a major obstacle in the adoption of renewable energy sources. However, grid scale energy storage must be inexpensive to be cost-competitive with existing energy sources such as coal and natural gas. Batteries have been widely considered due to their energy storage capabilities, but existing technologies are too expensive, often limited by raw material cost and difficulty scaling to high capacity installations. Flow batteries are designed for scaling to high capacities, but existing materials remain too costly for widespread adoption.

Semi solid flow batteries (SSFB) are developed by forming suspensions of electrochemically active and conductive particles for use as an anolyte or catholyte in a flow battery. By utilizing micron-scale powders from mature battery chemistries in a flowable suspension, the benefits of energy-dense intercalation chemistries with the scalability of flow battery architectures can be combined for low cost electrochemical storage. Presently, a narrow set of materials has been explored, focusing on chemistries with a lithium anode. In this work, a magnesium SSFB with an optimized MoS_2 cathodic slurry is demonstrated as a low cost and high material abundance alternative to lithium-based chemistries.

In this work, a mixed ionic-electronic conductive network is designed around a dual-ion (Mg^{2+}, Li^+) electrolyte, by combining the all-phenyl complex electrolyte (APC) with LiCl. MoS_2 and Ketjenblack (KB) are dispersed in the APC+LiCl electrolyte to form the cathodic slurry. The rheological, electrical, and electrochemical properties of APC-MoS_2-KB slurries with varying compositions have been measured. Full cells, with a Mg foil anode and MoS_2 slurry cathode, are shown to cycle reversibly in a non-flowing and flowing configuration, reaching 225mAh/g discharge capacity. LiCl concentration and KB concentration are identified as critical to high capacity slurry cathodes. The relative impacts of Mg^{2+} and Li^+ are quantitatively analyzed, showing that both ions are active and reversible during cycling.

The rate capability of the optimized slurry is characterized and discussed, and long term cycling tests are presented, showing non-flowing and flowing slurry batteries for 135 cycles. This work provides experimental data and insight into how existing low cost material sets can be utilized in a semi solid flow battery architecture.

Nobody cares
Work harder
- Lamar Jackson

Contents

List of Figures

List of Tables

Acknowledgments

It is my honor to acknowledge the support of the countless people who supported me and my work.

Vivek- your willingness to let students explore new areas within your group has blossomed every project that I've been a part of, and is exactly the type of environment that I wanted for my PhD. Your support has never gone unnoticed, and my growth as a scientist is the evidence of your support.

My family- you have been a part of every high and low during my graduate career, and your patience apparently knows no bounds. Every good quality I have as a scientist can be traced to each of my parents, and the other qualities can all be traced to Jenna. You are the reliable and loving people that I aspire to be, and are the reason I have even made it to this point.

Jas- meeting you and having you as a part of my life has changed my life immeasurably, for the better in every way. Your constant support, compassion, and personality have transformed the second half of my PhD, and has resulted in some of the best years of my life.

My lab group- I look back with fondness on all of the members of our group, and feel grateful to have had supportive, fun, interesting people around me throughout my PhD. Your contributions to my work are numerous, and I am very lucky to have built lasting friendships. I would like to especially highlight the contributions from Carlos to my perovskite work, and Raj to my battery work. It is no exaggeration to say that I wouldn't have finished either research project without your help, and each of you made even the most difficult stretches of my work enjoyable. Thank you both for taking a genuine interest in my work- your work ethics, selflessness, and friendship changed the course of my research for the better.

My friends- I have cherished every opportunity to spend time with each of you, both here in the Bay and at home on the East Coast, and these memories are some of the best I have from my PhD years. All of you bring a vibrancy and familiarity that never fails to make me laugh and feel at home, and this brought me relief during difficult times more than you may realize.

To the Marvell Nanolab, Cory Hall Machine Shop, Cory Hall and Sutadja Dai Facilities Team, and LSA Storeroom- you all have been the backbone of my lab research at Berkeley, and through your professionalism and wealth of knowledge have provided lab space, guidance, parts, and chemicals that are the foundation that my work stands on. Your contributions to my time at Berkeley are underrated but not forgotten.

My previous mentors- Logan Liu, Umberto Ravaioli, Eric Wong and Cherie Kagan- thank you for welcoming me into your labs and helping me become the researcher I wanted to be. Your guidance early in my career helped me to find my path, and I am forever grateful for that.

I would also like to acknowledge the guidance and feedback from the members of my prelim exam, qualifying exam, and dissertation committees. I am deeply grateful for your insights and suggestions.

Chapter 1

Introduction to Flow Batteries

1.1 Introduction

The effects of climate change have spurred research into energy storage technologies that can store the intermittent production from renewable energy sources. Batteries have distinct advantages for large scale storage, but cost targets remain unmet. This chapter contains a review of the economic motivations for grid scale storage, a review of flow batteries as an emerging energy storage technology, and concludes with the state of the art for slurry redox flow batteries.

1.2 Motivation for Grid Scale Storage

As the damages of climate change increase, low carbon emission energy sources have received increased interest. Many low carbon energy sources, namely solar, wind and wave power, produce energy intermittently, as they depend on time-varying factors such as sunlight, wind, and tide patterns. The intermittency of renewable energy is a severe obstacle to its adoption.

Presently, any demand for power on the electricity grid must be met in real time. Grid operators are challenged with purchasing electricity that will meet their grid's time-varying demand but are limited to the energy sources that are available at the time of the demand [1]. Because renewables do not provide steady power throughout the day and cannot be switched on suddenly to match spikes in demand, the maximum output of renewable energy sources is limited to the demand present at the hours that renewables produce electricity[2]. Peak electricity demand commonly occurs in the afternoon and evening times, while renewable output is typically concentrated in morning and afternoon hours in most locations [3]. This leads to renewables being severely limited in their overall contributions to power demand on the grid.

Nuclear power is a low carbon energy source with a different output pattern than time-varying renewables. Nuclear power plants are designed for infrequent maintenance and are not operated to respond to sudden changes in demand [4]. Due to its continuous power

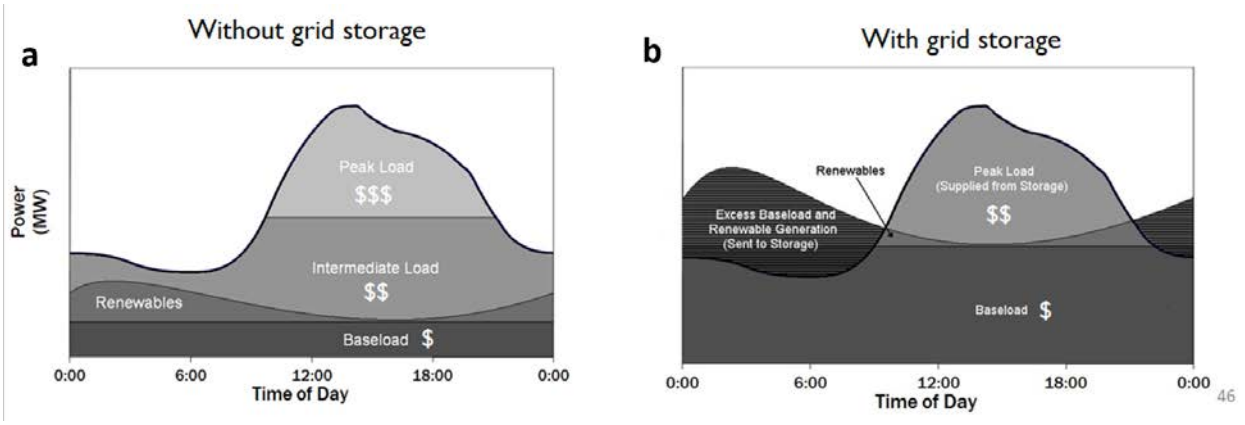

Figure 1.1: Grid-level electricity demand over 24hrs, with color representing the source of electricity, in the case of **a)** no grid storage **b)** with grid storage available. Adapted from [2]

output over long time periods, nuclear power is well suited for baseload power generation. Baseload power is the portion of electricity demand that is constant throughout the day and is typically supplied by low-cost power plants whose output needs to be continuous over long time periods [5]. Baseload is desirable due to its low cost and predictable output, and nuclear is desirable as a baseload technology because of its low carbon emissions. As demand varies substantially throughout the day, the inability of nuclear power to respond to immediate changes limits the maximum amount of nuclear power to the amount of baseload.

As illustrated in Figure 1.1**a**, intermediate and peak demand are presently beyond what baseload or renewables can currently provide. In order to meet this demand, energy sources that respond rapidly to changes in demand are deployed. Natural gas and coal fired power plants can be switched on almost immediately and are run for short periods of time until a spike in demand subsides. Short-term generator plants commonly produce high carbon emissions and are expensive to operate as they run infrequently [6].

The desire to increase the contributions of renewable and baseload energy, and reduce the amount of high cost and high carbon sources, has motivated a new class of energy storage technologies, commonly referred to as "grid scale storage". Grid scale storage refers to energy storage technologies that store energy, typically from power plants, and use it to meet demand on the power grid at a later time. Energy storage connected to the grid allows energy supply and demand to be decoupled; any excess energy produced at a certain time can be stored and used to fulfill unmet grid demand at a later time. Grid scale storage enables two pathways that can increase the utilization of low-carbon energy sources: peak shaving and increasing baseload. Peak shaving is illustrated in Fig. 1.1**b** and occurs when the peak electricity demand is supplied by energy that was produced at an earlier time and stored. Peak shaving is possible because grid scale storage decouples when energy is produced from when it is used. Solar energy from the early morning can be stored, then dispensed to meet

demand during the evening peak. Storage can also increase the amount of baseload that is usable, even above the demand level that is constant throughout the day (see Fig. 1.1**b**). Grid storage stores the baseload at times when baseload exceeds demand and supplies the power back into the grid to address demand peaks at a later time. These pathways solve technical constraints of integrating low cost, low carbon energy sources into the grid.

1.3 Target Metrics and Options for Grid Scale Storage

To help researchers working on various grid scale storage technologies guide their efforts, the US ARPA-E GRIDS (Grid-scale Rampable Intermittent Dispatchable Storage) program has established the following target technical metrics for grid scale storage, at which it is estimated that grid scale storage will be commercially viable:

Cost	$< \$100$/kWh
Durability	> 5000 cycles
Efficiency	$> 80\%$ round trip
Minimum Time at Rated Power	60 mins

Table 1.1: US ARPA-E grid scale storage target metrics [7]

The cost, durability, and efficiency metrics, taken in combination, represent an estimated \$0.025/kWh storage cost over the lifetime of the battery. This storage cost puts the total cost of energy production and storage below total electricity cost targets. Utility-scale storage technologies are expected to last at least 10 years in the field, and the 5000 cycle target is derived from an expected 10 year operation lifetime. The minimum time at rated power metric demonstrates that storage technologies that operate for seconds or a few minutes are not sufficient to smooth the production variability of renewable sources, and that at least one hour is required for a storage technology to be feasible [8].

Cost estimates for various energy storage technologies, as calculated by ARPA-E, are shown in Figure 1.2.

Pumped hydroelectric and underground compressed air energy storage are the two technologies currently below the \$100/kWh energy-related cost threshold, as shown in Fig. 1.2. Due to its low cost and technological maturity, pumped hydroelectricity constitutes 96% of worldwide energy storage [9]. Both pumped hydroelectricity and compressed air energy storage are geologically limited to sites that either have a large dam or a large underground cavern, respectively. Neither technology can be scaled up, as the capacity of each site is limited by the size of the dam or cavern. The limited number of suitable sites and lack of scalability for hydroelectricity and compressed air make them insufficient to meet the growing needs of grid storage.

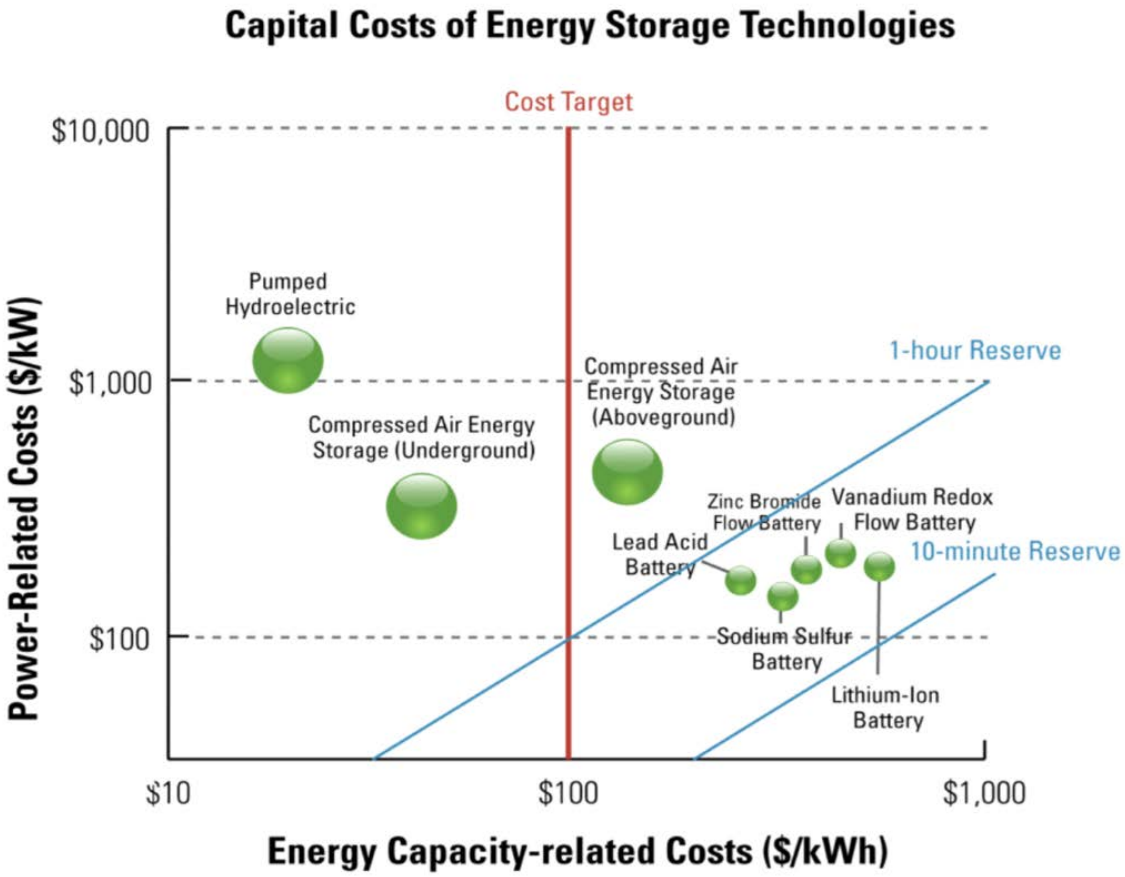

Figure 1.2: Energy and power costs of leading grid scale storage technologies. Adapted from [7]

1.4 Flow Batteries for Grid Scale Storage

Flow batteries are a particularly well suited technology for grid scale storage, as they have been developed specifically for the constraints and target metrics of large scale energy storage. This section will discuss the basic components and operating principles of flow batteries, cover the vanadium redox flow battery in some detail, and then highlight the state-of-the-art redox flow batteries and their advantages/disadvantages.

Principles of Redox Flow Battery Operation

A traditional redox flow battery consists of two tanks, two pumps, and an electrochemical cell (see Figure 1.3). Each tank stores an electrolyte, either the catholyte or anolyte, and a mechanical pump is operated to flow these electrolytes through each side of the electro-

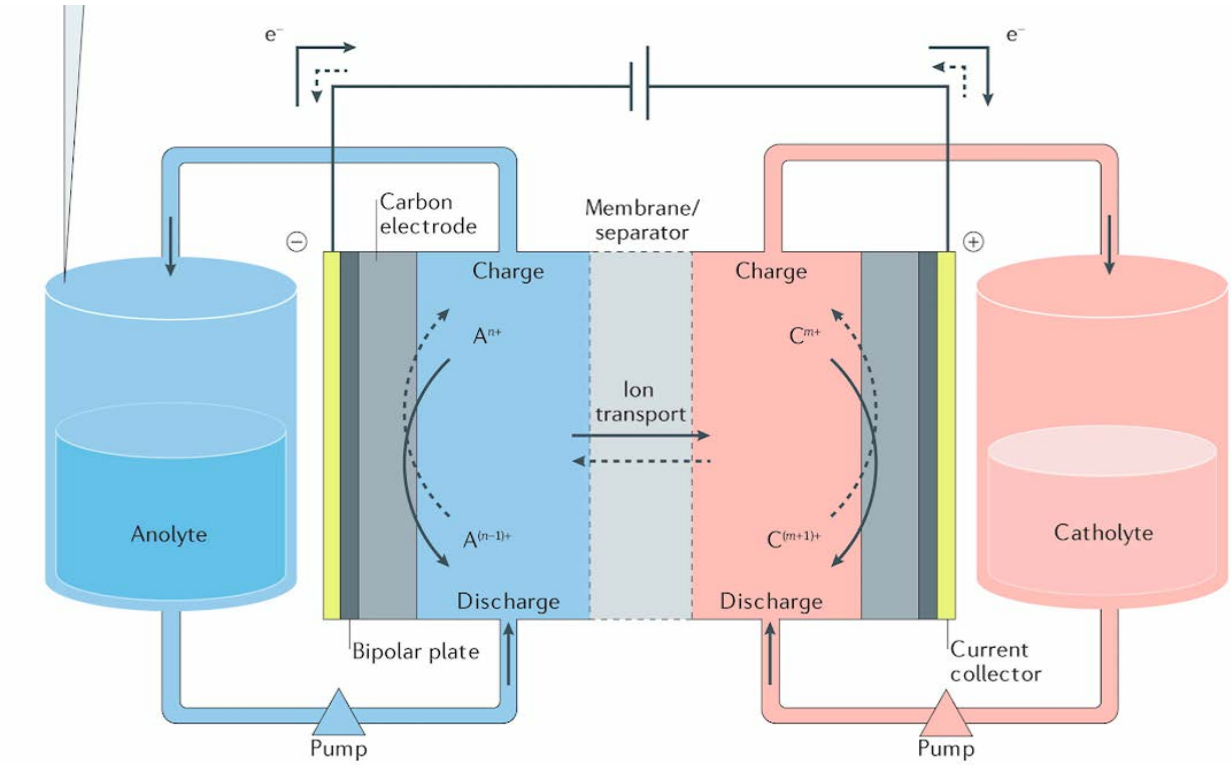

Figure 1.3: Schematic diagram of traditional 2-tank flow battery, depicting key components and general ion/electron motion within a flow cell. Adapted from [12]

chemical cell. A catholyte is an electrolyte with a cathode material dissolved or suspended within and operates as the cathode half reaction of the cell [10]. Anolytes are analogous to catholytes, for the anodic half cell. The catholyte and anolyte are pumped into the electrochemical cell and undergo redox reactions, which produce a cell voltage and generate ions or electrons. Within the electrochemical cell, the catholyte and anolyte are separated by a membrane (also referred to as a separator) which permits a flow of ions across it, allowing charge to balance as electrons flow from the anode to cathode side of the cell. Carbon electrodes are in contact with the catholyte and anolyte, and serve as the sites of redox reactions, with the carbon electrodes then conducting generated electrons and transporting them to the external circuit. Bipolar plates are rigid, conductive plates placed between the current collector and electrolyte to increase mechanical strength of the cell and reduce corrosion of the current collectors [11].

Commonly, the electrolytes in redox flow batteries are salt-in-electrolyte, where a salt with multiple valence states is dissolved into a liquid electrolyte. In Section 1.5, the example of a vanadium redox flow battery, a chemistry explained in more detail later, illustrates how anolytes and catholytes behave during cycling. The catholyte is vanadium oxide (dissolved

in an aqueous electrolyte, sulfuric acid), and can exist reversibly in the VO_2^+ and VO^{2+}; the anolyte is vanadium, which can exist in the V^{2+} and V^{3+} states. As the cell is charged and discharged, the vanadium compounds change oxidation states, and produce a redox pair. This redox pair, with a potential difference between the half cells and free electrons, is where the charge/discharge capacity of the cell originates.

Scalability Advantages of Redox Flow Batteries

The cathode and anode material in a traditional coin or cylindrical cell are sintered into solid films that are contained within the battery casing. For these battery cell formats, the capacity is limited by the size of the electrochemical cell. To increase the capacity, multiple cells can be attached in an array, or each cell can be made larger. Both of these methods require additional cell casing, electrodes, separator and current collectors to increase capacity; in a coin or cylindrical cell, the cell cost is scaled with both the active and inactive materials. The liquid catholyte/anolyte in a flow battery has the advantage of decoupling the capacity of the battery from the size of the electrochemical cell. In a flow battery, the cathode and anode material are stored in tanks, not within the electrochemical cell. By increasing the size of the storage tanks, the flow battery has more active material available-without having to increase the area of the electrochemical cell. In a flow battery, the energy stored is proportional to the storage tank size, not the cell volume or area, and removes the cost of additional casing, separators, and current collectors when producing a large scale flow battery [13].

Within a traditional 18650 battery cell, less than 50% of the volume is used for active materials; the majority of cell volume is taken up by binder, additives, the separator, and the casing. Flow cells have less volume dedicated to inactive battery material, allowing for an increased vol% of active material and greater volumetric density [14].

As the catholyte and anolyte are flowable, the flow rate of the electrolytes offers additional flexibility during operation. By flowing the electrolytes at a higher rate, the power output of the cell can be increased, because fresh active material is entering the cell as the electrolyte flows in. Flow batteries offer decoupled control over energy and power output, allowing their output to be tailored for a variety of different usages.

To meet the capacity needs of grid scale storage, a range of hundreds to thousands of cylindrical or pouch cells need to be connected in an array. To distribute electrical load between cells and identify potential thermal runaway, each individual cell must be monitored using a battery management system (BMS). This introduces additional cost and complexity to large arrays of battery cells. Flow cells avoid this issue, as many chemistries are made with non-flammable materials, eliminating concerns over thermal runaway, and substantially fewer flow cells are required to achieve the same capacity, reducing the amount of BMS-related electronics.

1.5 State-of-the-Art in Redox Flow Batteries

A wide array of chemistries have been explored in flow battery systems, each trying to leverage unique benefits of their own materials while improving on the limitations of previous designs. In this section, the most significant flow battery chemistries are reviewed. Table 1.2 lists the main chemistries reviewed in this chapter (in order of appearance), and the primary advantages and disadvantages of each.

Chemistry	**Key Advantages**	**Disadvantages**
Vanadium	Durability, low crossover	Material cost, low solubility
Organic	Tunable molecules, durability	Energy density, low solubility
Sulfur	Material cost, capacity	Side reactions, low conductivity
Metal-air	Material cost, low weight	Side reactions with CO_2 + H_2O

Table 1.2: Flow battery chemistries reviewed in this section

Vanadium Redox Flow Batteries

Redox chemistry

The dominant flow battery technology is the vanadium redox flow battery. The vanadium chemistry was selected because vanadium serves as the active material in both half cells, which minimizes the negative effects of crossover seen in early iron/chromium flow batteries. Crossover occurs when chemical species from one half cell mix with the other half cell, leading to unwanted side reactions, inseparable byproducts, or unwanted capacity loss [15]. The first vanadium flow cell work from 1985 leverages the fact that vanadium exists in multiple redox states, using V^{2+} / V^{3+} in the anodic half cell and V^{4+} / V^{5+} in the cathodic half cell [16]. In the +4 and +5 oxidation state, vanadium produces $VO_2{}^+$ and VO^{2+} ions, respectively, so the $V^{2/3+}$ / $V^{4/5+}$ chemistry is commonly expressed as V / VO_2, shown in Figure 1.4. The vanadium half cell reactions are expressed in Equations 1.1-1.3 [14].

$$VO_2^+ + 2H^+ + e^- \longleftrightarrow VO^{2+} + H_2O \tag{1.1}$$

$$V^{2+} - e^- \longleftrightarrow V^{3+} \tag{1.2}$$

$$VO_2^+ + V^{2+} + 2H^+ \longleftrightarrow VO^{2+} + V^{3+} + H_2O \tag{1.3}$$

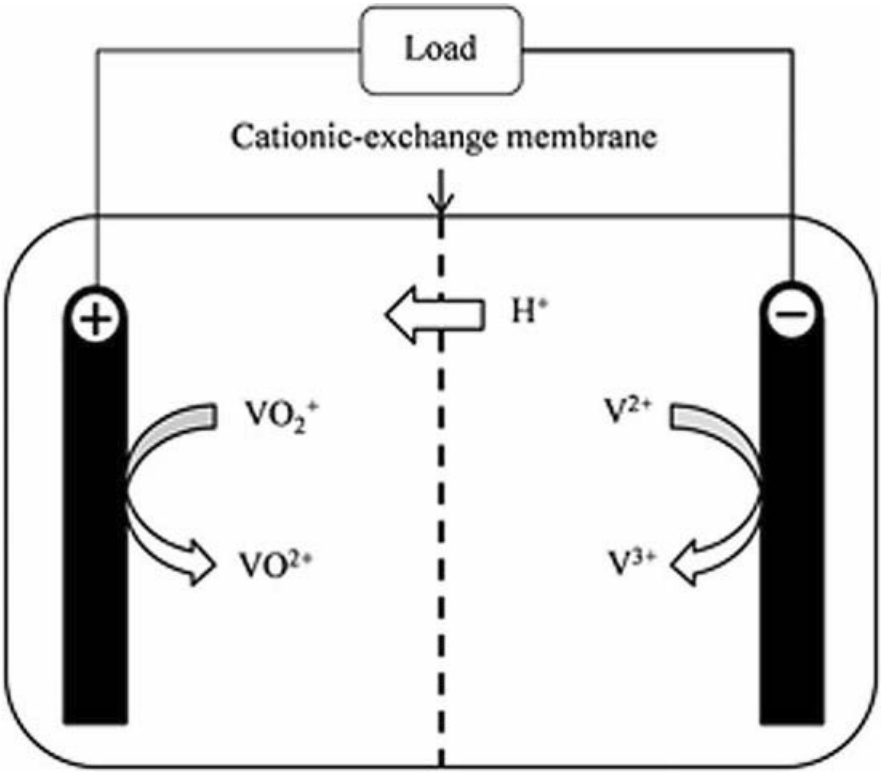

Figure 1.4: Schematic of vanadium flow cell. Adapted from [17]

Electrolyte

Vanadium redox flow batteries commonly use an aqueous electrolyte of concentrated sulfuric acid. In aqueous systems, voltages of >1.25V decompose H_2O into O_2 and H_2 gases, a reaction known as electrolysis. In flow battery systems, electrolysis should be avoided to prevent electrolyte decomposition. Figure 1.5 shows the standard potential of common electrochemical redox couples, and illustrates the boundaries (vs SHE) at which the anode evolves oxygen (0.815V) and the cathode evolves hydrogen (-0.414V). By choosing a pair of redox reactions, each with a standard potential within the electrolysis boundaries, the evolution of both H_2 and O_2 gas is avoided. The V^{2+}/ V^{3+} and $VO_2{}^+$ / VO^{2+} redox reactions are near the theoretical limits for aqueous reactions, forming a redox couple with an open circuit voltage of 1.25V [18].

In flow batteries, the electrolyte serves as a host medium, in which the redox-active materials are dissolved and flowed throughout the electrochemical cell via mechanical pumps. The electrolyte for the vanadium redox flow battery system is most commonly a highly concentrated sulfuric acid/water solution [19]. In traditional flow battery systems, active materials are dissolved in the electrolyte, creating the anolyte and catholyte. (Other systems

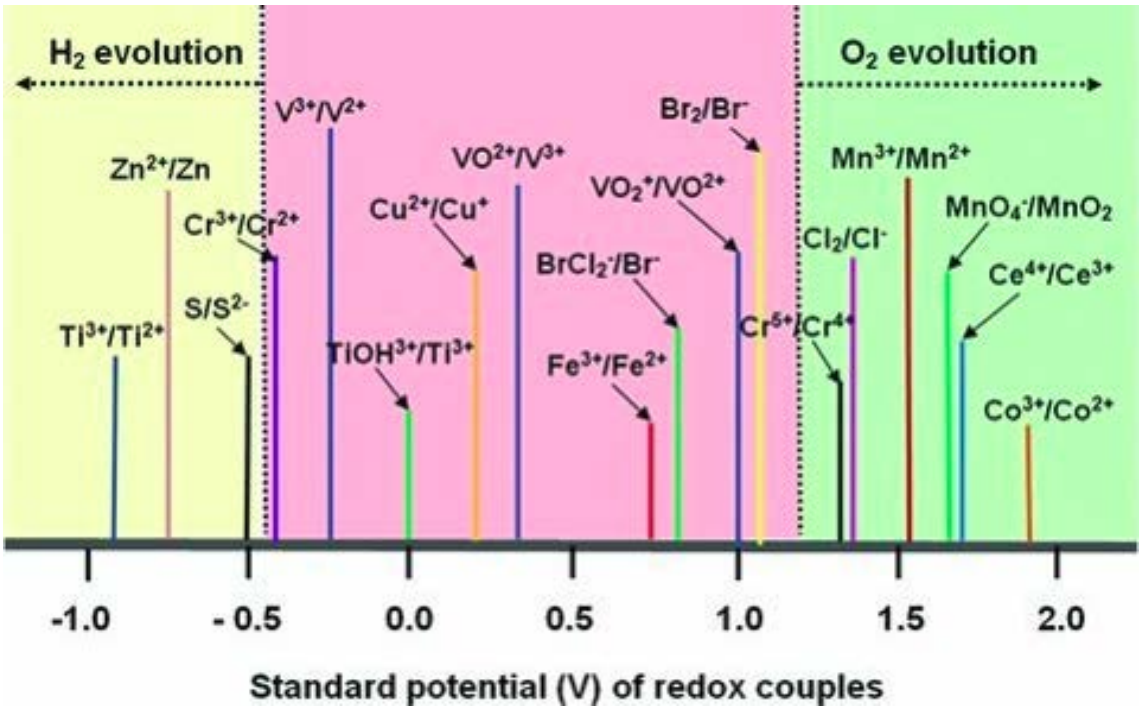

Figure 1.5: Standard potential of redox couples commonly found in electrochemical literature. Adapted from [14]

in which the active material is not dissolved in the electrolyte are discussed later in this section) Commonly, the active materials in a flow battery are salts that are dissolved in the electrolyte. The solubility of the salt in the electrolyte is a critical parameter that determines the amount of redox-active species per unit volume in the flow battery, or the volumetric energy density. For vanadium salts in sulfuric acid, the solubility limit is around 2M, leading to a volumetric energy density of <25 Wh/L [19] [20] [21]. This solubility limit is widely acknowledged as the main bottleneck to increasing the energy density of vanadium flow batteries.

An important consideration for vanadium systems is the operating temperatures that the electrolyte will be exposed to during the cell lifetime. Vanadium electrolytes have shown to be stable between 10-40°C. Outside of this range, the solubility of vanadium salts decreases and active material precipitates out of the catholyte and anolyte, leading to capacity loss [18]. For many practical applications, temperature control is required to keep the stack temperature between 10-40°C, which can significantly increase costs and reduce round trip efficiency [22]. The use of additives has been explored, with polyacrylic acid helping to impart stability on all 4 valence states of vanadium up to 2M. However, temperatures greater than 40°C remained unstable [23]. Work at Pacific Northwest National Lab into mixed-acid electrolytes, namely sulfuric acid and hydrochloric acid, showed stability at a higher concentration (2.5M) and

across a wider range of temperature (-5-50°C) [18].

Membrane

Vanadium flow batteries require an ion exchange membrane (IEM), as the soluble vanadium ions are sub-nanometer in diameter and would not be filtered by size selective membranes. Nafion remains the most widely studied and highest performing IEM, with high performance shown in a range of vanadium systems [24]. However, the high cost of Nafion represents a bottleneck for flow batteries and is cited as one of the largest single costs in a flow battery stack [25]. Research on less expensive membranes has focused on non-fluorinated membranes and sub-nanometer size selective porous membranes [14].

Electrode

The redox reactions occurring in a vanadium flow battery occur on the surface of the electrodes, making electrode design a vital component of flow battery development. Typically, carbon materials, such as carbon felts or glassy carbon, are used as VRFB electrodes, as they are low cost, conductive, and suitable for a variety of surface treatments and modifications [26]. Vanadium conversion reactions on the surface sites of the carbon electrodes cause no degradation of the vanadium compounds or the carbon electrodes, and has led to cycle life demonstrations of over 10,000 cycles [27]. There is on-going work to elucidate rate limiting steps and understand the exact surface site chemistries of electrodes in VRFBs [26].

Cost

The high cost of vanadium precursors remains the greatest limitation for widespread adoption of VRFBs. Raw material costs for vanadium redox flow batteries are approximately $120/kWh, surpassing the total system cost target for grid scale storage (Figure 1.6) [28]. Total system costs, for 4-8 hr storage time frames, are predicted to reach $200-300/kWh, still well short of the $100/kWh grid level target [29]. This inherent materials limitation of VRFBs has ignited research into lower cost precursor materials for flow batteries (see Sections 1.5.2-1.5.4). The solubility limits of vanadium salts, which limit volumetric energy density, have spawned interest in chemistries that are not constrained by solubility (see section 1.5.4 on semi-solid flow batteries).

Organic redox flow batteries

Organic redox flow batteries utilize organic molecules that are redox-active, and are of interest to the flow battery community due to their high structural tunability and low precursor cost [30]. The field of organic flow batteries can be divided into metal-containing (organometallic) and metal-free (all organic) chemistries.

Metal-containing organic redox chemistries show high chemical stability, high redox potential (3.44V vs Li), and stable cycling. However, the high cost of cobalt and ruthenium, the

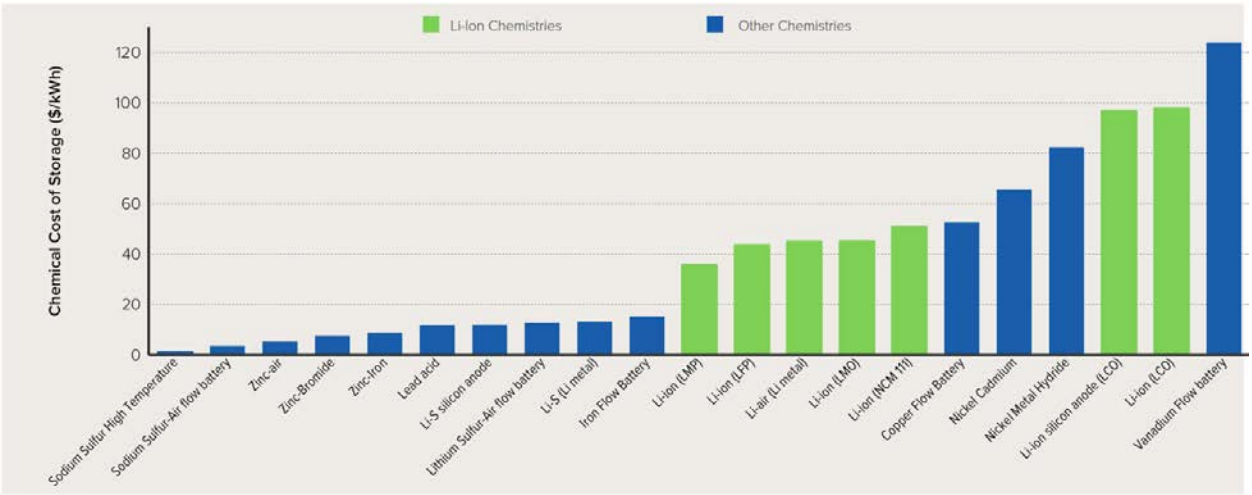

Figure 1.6: Chemical cost of storage for grid scale technologies (2019). Adapted from [28]

most common metals used in these systems, and their low solubilities in suitable electrolytes are ongoing barriers for organometallic systems. These challenges led to the development of all-organic redox systems without metals [31] [32].

All-organic flow batteries are based on either an aqueous or non-aqueous electrolyte. The energy density of aqueous electrolytes is limited by low open circuit voltages of ≈1.5V due to H_2/O_2 evolution (electrolysis) but exhibits less toxicity/flammability and lower material costs. The low solubility of organic materials in aqueous electrolytes is an additional bottleneck [31] Cost modeling by Dmello et al. shows the route to lowering costs in an aqueous organic flow battery is to integrate less expensive active materials, as the operating voltage is constrained, and electrolyte materials are already low cost due to high volume production for other applications [33].

Non-aqueous all-organic flow batteries are not limited by electrolysis voltages and can show open circuit voltages of ≈3V. Irreversible reactions due to radical generation during redox reactions have caused diminished cycling efficiency, but additives have been employed to mitigate those concerns in some chemistries [12]. Organic solvents used in non-aqueous systems are more expensive than in aqueous systems, so the high solubility of the active compounds in non-aqueous systems is required to achieve lower costs. The most promising route to lowering cost for non-aqueous systems is to increase the voltage of the redox couple, as the materials costs are not too high and solvents are known to be relatively expensive [33].

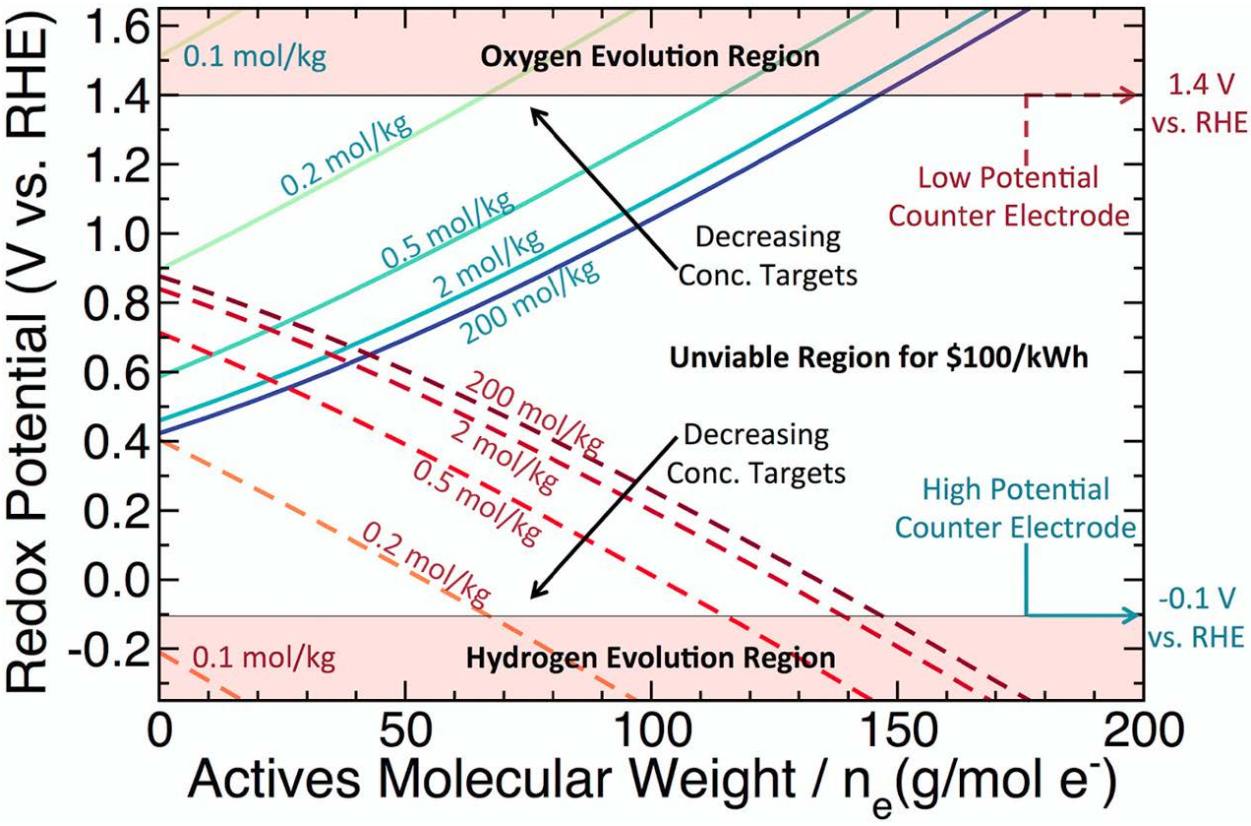

Figure 1.7: Economically viable technical parameters for aqueous and non-aqueous electrolytes, highlighting the effect of solubility and voltage. Adapted from [33]

Sulfur-based flow batteries

Sulfur is a highly suitable material for batteries, with a high energy density (2200 Wh/L) [12] and low cost ($0.20/kg) [33]. These characteristics have attracted significant attention to lithium-sulfur batteries as outlined in several review papers [34, 35]. The main issue limiting Li-S batteries is polysulfide dissolution, when highly soluble intermediate redox states of lithium-sulfur (Li_2S_4, Li_2S_8) are created and migrate towards either the anode or cathode. This migration, known as "shuttling", is a form of self discharge that reduces the coulombic efficiency of the cell and leads to irreversible Li_2S/Li_2S_2 solid deposition on the current collectors [12]. In most Li-S literature, strict voltage limits are set, which limits sulfur to the solid state to avoid generating soluble polysulfide species. As shown in Figure 1.8, these voltage limits severely hamper sulfur capacity [12].

Pan et al. capitalized on the high solubility of the polysulfide species and designed a Li-S flow battery with lithium polysulfide species as the redox active material. With soluble polysulfide species now a desirable feature in the cell, a DMSO-solvent was chosen

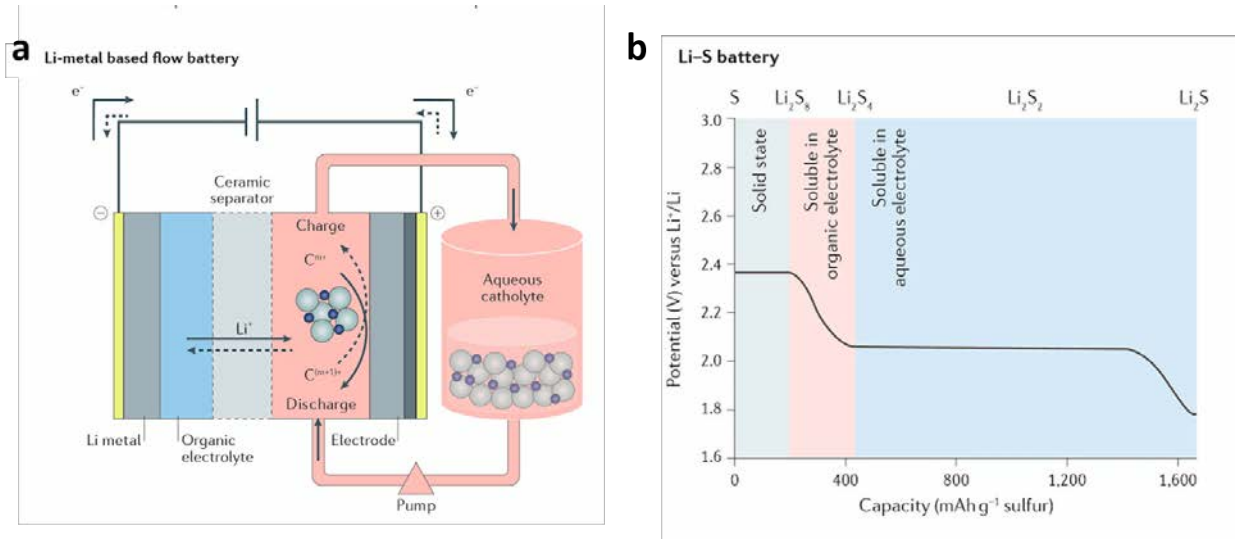

Figure 1.8: (a) Schematic of Li metal-sulfur flow battery (b) Capacity diagram for different states of lithium-sulfur compounds. Adapted from [12]

to maximize polysulfide solubility. The operating voltage was restricted to a range where sulfur existed only in the liquid state, greatly increasing the theoretical capacity of their system over standard Li-S systems that used solid-state sulfur voltage limits [12]. Evidence of any shuttling mechanisms was not found, and high capacity retention (85% retention over 50 cycles) was demonstrated [36].

Fan et al. used a flow battery architecture to address two prominent limitations of coin cell sulfur-based batteries. Sulfur is known to suffer from low utilization due to its insulating properties, and many strategies to mix in conductive additives have been employed in the coin cell literature [37]. Fan et al. mixed solid state sulfur particles with carbon black and suspended the mixture in the liquid electrolyte, forming a flowable percolating conductive network. This flowable suspension promotes high sulfur utilization via chains of conductive carbons that contact each sulfur particle and transport redox charge to the current collectors. The sulfur-carbon suspension was cycled over the full voltage window of sulfur to include solid state and liquid state sulfur. In this flow system, sulfur precipitates out of solution as a solid onto the carbon particles at high voltages and solubilizes into the electrolyte as a liquid at low voltages. This study highlights how flow batteries can accommodate precipitation-dissolution redox reactions while retaining reversibility [38].

Metal-air flow batteries

Metal-air batteries offer an ideal combination of high theoretical energy density and low material cost, as the air half cell is compact, low weight, and offers unlimited material

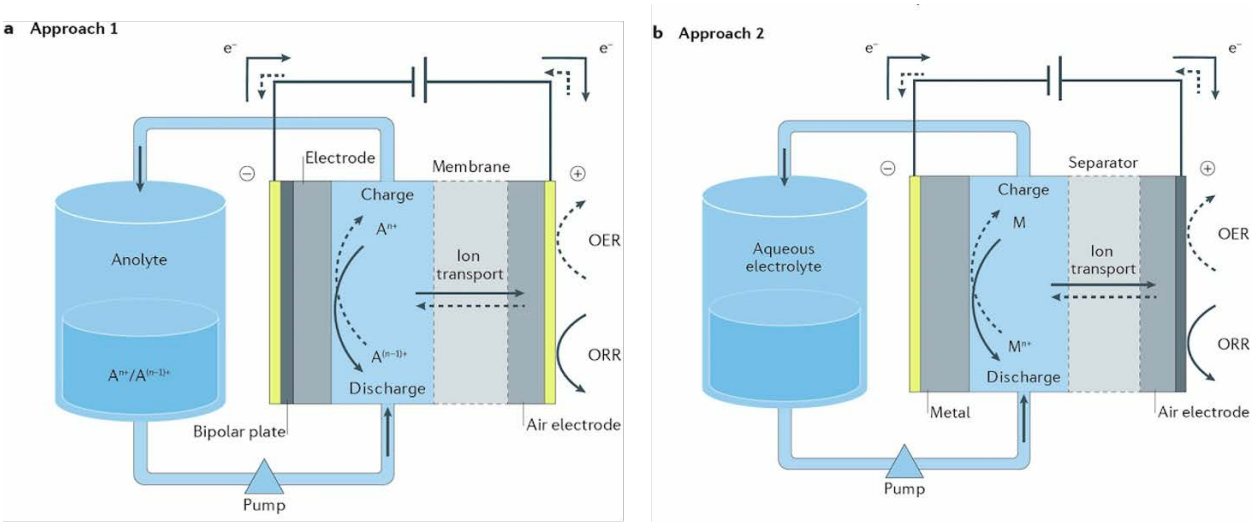

Figure 1.9: Types of metal-air flow battery: (a) Anolyte-flowing (b) Electrolyte-flowing. Adapted from [12]

supply (oxygen) at no cost. As the air half cell has virtually no weight, metal-air chemistries have the potential to reach the theoretical gravimetric energy density of the metal half cell. In a lithium-air battery, the theoretical limit of lithium metal is 11,700 Wh/kg, close to the energy density of gasoline [39]. As shown in Figure 1.9, metal air batteries have an oxygen evolution reaction (OER) or oxygen reduction reaction (ORR) as one half cell, and a metal-based redox reaction as the other half cell. Zinc-air [40], vanadium-oxygen [41], and lithium-air are common oxygen-based battery chemistries [42]. Cells combining air/sodium/sulfur, and using OER/ORR and polysulfide oxidation/reduction to combine 3 inexpensive materials, brought materials cost for both half cells to ≈$1/kWh [29].

Metal air flow batteries have two variations: flowing an anolyte (Fig 1.9a), or flowing the liquid electrolyte across an anode foil (Fig 1.9b) [12]. Similar to traditional vanadium flow batteries, vanadium-oxygen flow cells operate by flowing the anolyte solution but replace the catholyte with an air cathode. An air cathode doubles the theoretical gravimetric energy density compared with the traditional liquid VRFB, as the cathode half cell is replaced with only a thin membrane [43]. In Zn-air flow batteries, controlling anodic Zn deposition morphology is critical to long term operation. Studies have shown that flowing the electrolyte in a Zn-air system suppresses dendrite formation, as it is predicted that refreshing the electrolyte provides uniform ion transfer at the Zn surface, leading to uniform Zn plating on the anode [40]. In Zn-air flow batteries, flowing the electrolyte across a solid anode is used to improve performance.

Slurry Flow Batteries for Grid Scale Storage

Slurry flow batteries, also known as "semi-solid" batteries, are classified as flow batteries that include either an active or conductive material in the solid phase. In liquid flow batteries, the active material is fully dissolved in the electrolyte, whereas in a slurry flow battery either the active or conductive material is insoluble in the electrolyte and is instead suspended within the liquid electrolyte. As described in the next several sections, there are a variety of advantages to incorporating solid materials into a flow battery- most notably that it allows high energy density materials to be exploited in the scalable architecture of a flow battery.

Qi et al. classify the various types of flow batteries involving solid electroactive materials into four groups, depending on which components (conductive or active) are suspended in the electrolyte (flowing), or are solid and non-flowing (static) [44]:

- Type 1: Flowing conductive material, static active material
- Type 2: Flowing conductive material, flowing active material
- Type 3: Static conductive material, flowing active material
- Type 4: Static conductive material, static active material, flowing chemical redox mediators

Type 1

In Type 1 flow cells (Figure 1.10a), the conductive material (carbon) is suspended in the electrolyte and flows through the cell, while the active material exists either as a solid electrode or is dissolved into the electrolyte. As the electrolyte-carbon suspension flows through the cell, redox reactions occur on the surface of the conductive material. The charge from the redox reactions is transported to the current collector when the carbon particle hosting the reaction is in physical contact with the current collector, or when electrically connected to the current connector via a chain of carbon particles/aggregates. In some architectures (Type 2, Type 4), large pumping forces are required to flow the anolyte or catholyte, leading to a large pressure drop in the channel and high energetic losses via the mechanical pump. Flowing only the conductive material reduces the viscosity of the electrolyte and reduces the pumping losses for Type 1 cells [44].

Ruggeri et al. adapted the Li-O_2 chemistry into a Type 1 cell (Figure 1.11), and outlined several advantages of flowing the conductive additive in their design compared with a traditional non-flowing coin or cylindrical cell [45]:

1. No redox mediators are needed
2. ORR reactions can take place on dispersed carbon particles, which prevents them from passivating the current collector

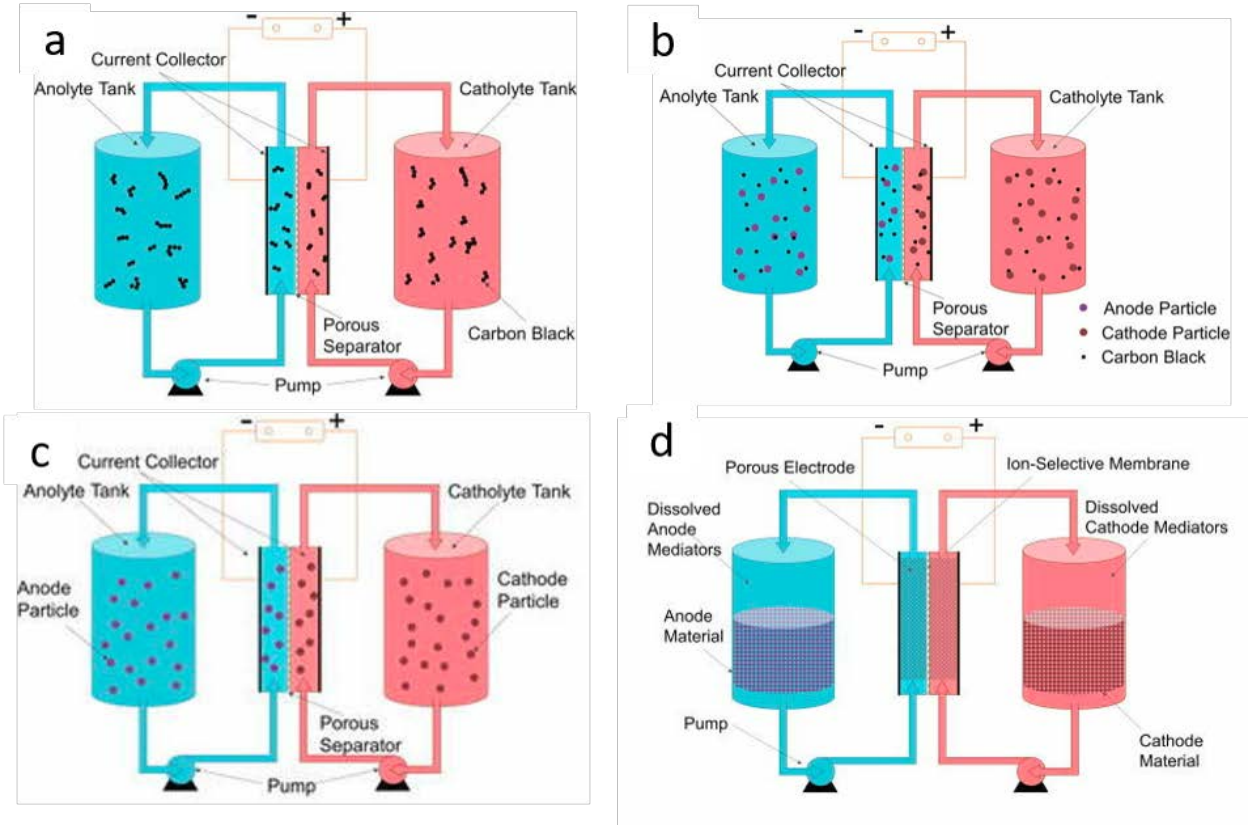

Figure 1.10: Types of semi-solid flow batteries (a) Type 1 (b) Type 2 (c) Type 3 (d) Type 4. Adapted from [44]

3. Flowing carbon particles offer high surface area

4. ORR products can be deposited on the carbon, stored in the tank, then reoxidized later, without affecting the active materials/surfaces within the electrochemical cell

In Type 1 cells, reactions take place on carbon surfaces, which avoids passivation of current collectors, allows soluble species in the electrolyte to precipitate as solids onto the carbon, and can be reversibly solubilized when reversing the reaction. Ruggeri et al. leveraged these unique advantages of Type 1 cells to remove the cathode (O_2) discharge products from the Li-O_2 system. The suspension provided sites for redox reactions, then, by pumping out the discharge products, the current collector and separator were kept safe from passivation. [45].

Mubeen et al. explored zinc, manganese, and copper as deposition metals in their Type 1 flow battery design, plating these earth-abundant materials onto the surface of carbon particles. Figure 1.12a shows the overpotential and current produced for each metal, and

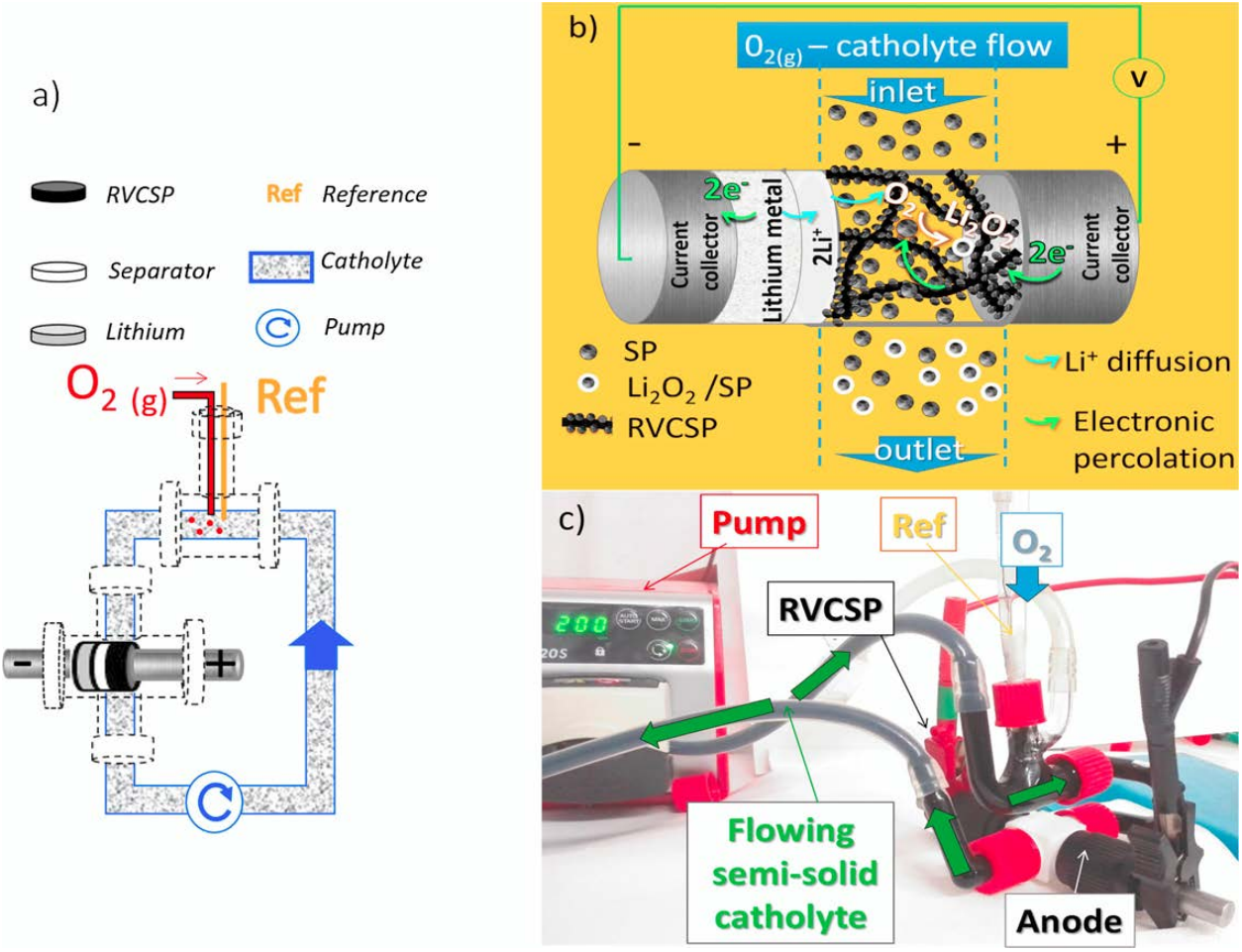

Figure 1.11: (a) cell schematic of Li-O_2 system (b) system diagram of Li-O_2 system (c) picture of lab setup for Li-O_2 system. Adapted from [45]

Figures 1.12c and 1.12d highlight that only when the carbon particles are incorporated does this cell format show any electrochemical activity [46]. Their work shows explicitly that micron-scale carbon particles act as hosts for redox reactions and can subsequently transfer the redox charge through a percolating network.

Type 2

Type 2 flow batteries are the most common type throughout the semi-solid flow battery literature and will be the subject of the work presented in later chapters. In Type 2 flow batteries, both the active and conductive material are suspended in the electrolyte. Generally, the active materials are intercalation compounds, selected for their high energy density. Ions from the electrolyte intercalate into the active material, and the charge generated by

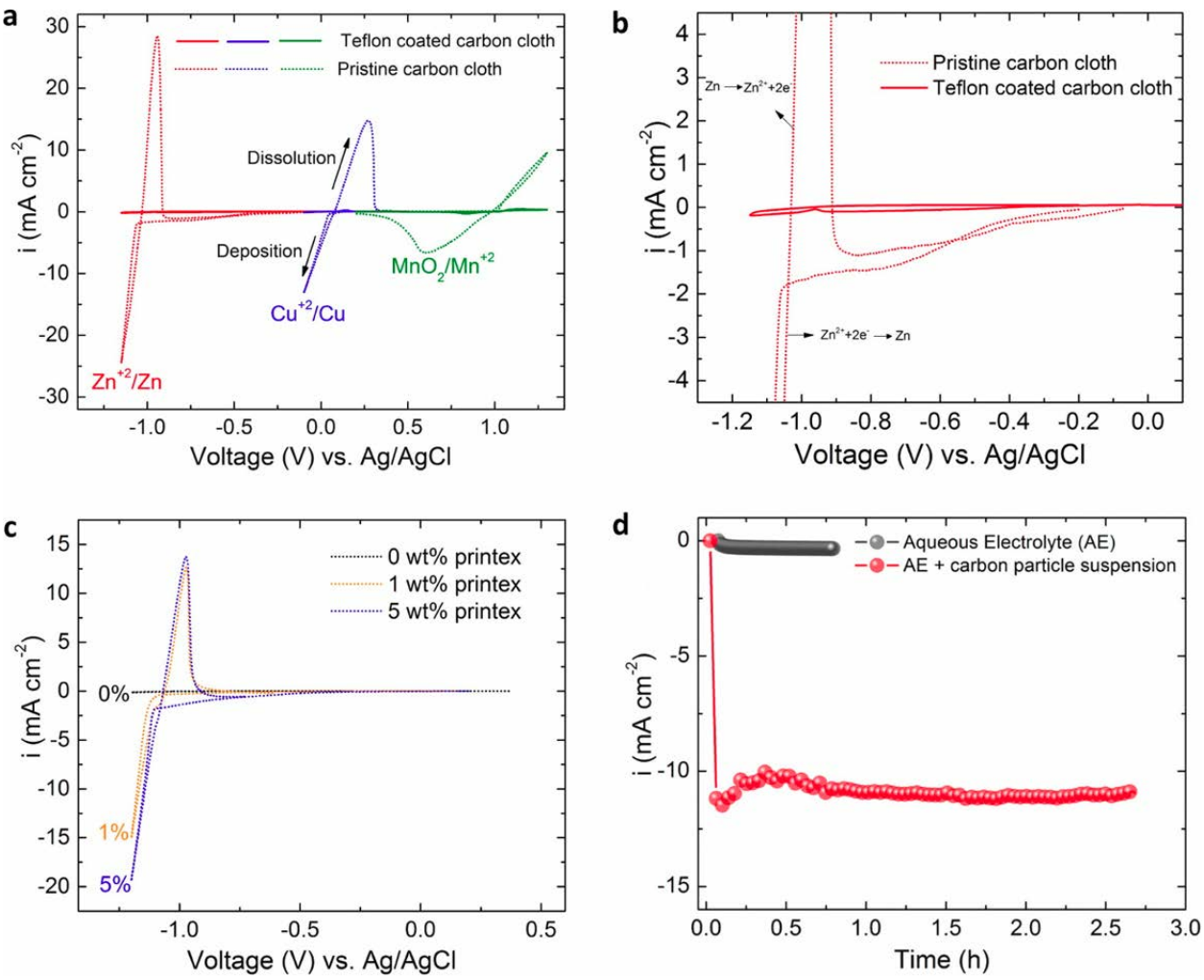

Figure 1.12: Cyclic voltammetry results of plating Zn, Cu, and MnO_2 on carbon particles. Adapted from [46]

this redox reaction is transported to the current collector via a conductive network of the conductive carbon particles.

Material design: Type 2 semi-solid batteries were developed to combine existing low cost, high energy density materials with the scalable architecture of flow batteries. The slurry in a Type 2 cell contains both the active and conductive materials, and, therefore needs to transport ions and electrons, host redox reactions, and be flowable.

The critical innovation in Type 2 cells is using a suspension of solid active particles in a liquid electrolyte, to avoid the constraint of solubility limit present in liquid flow batteries. Solubility limits have limited energy densities in most existing flow battery designs, and by creating a suspension in which solubility is not a factor, the active material density in Type 2 cells is only limited by flowability through the channel.

Type 2 battery research has predominantly focused on intercalation materials as the active material for their high energy density and well studied properties in existing battery literature. Lithium compounds are the most commonly studied, such as LCO [13], LFP [47], LTO [13, 47, 48], and LMO [13]. Sodium-based compounds have also been studied via the $NaTi_2(PO_4)_3$ cathode [49]. Ketjen black (KB), a type of carbon black, has been the near exclusive choice as a conductive additive in semi solid systems due to its high surface area and electrical conductivity [50, 51].

An important material design consideration for semi-solid flow batteries is the concentration of active material. Initial estimates from Dudata et al. suggested that semi solid batteries could achieve concentrations of 10-40M of active material (compared with 2-3M in vanadium systems), assuming that 50%vol solid loading is achievable [13]. They note that 70%vol solid loading had been achieved in similar flowable systems. Active mass loadings of 15-25%vol [13, 47, 48] have been explored, while scaling to higher loadings has not yet been shown. Madec et al. highlight the challenge of increasing active particle loading in a slurry, and show that at 25%vol LTO, that particle utilization and gravimetric capacity was lower than at 15 or 20%vol for a fixed amount of ketjen black [48]. Estimates from Dudata et al. suggest a material cost of \$40-80/kWh for a lithium intercalation compound/KB slurry in nonaqueous electrolyte, with roughly \$10-14/kg active material, and \$14/kg for the electrolyte components [13]. This cost is well below that \$100/kWh target for widespread grid scale storage.

A key advantage of using insoluble, micron-scale powders in a Type 2 battery is that microporous polymer membranes can be used as the separator. Other flow systems require expensive ion exchange membranes to separate the anode and cathode half cells, as the ions in the anolyte and catholyte are dissolved compounds that are subnanometer in size. In Type 2 systems, inexpensive and widely available polymer membranes such as Celgard have been used throughout the literature with high success [44].

Rheology: The rheology of the catholyte/anolyte suspension is critical to cell performance, and is the most important and novel technology within the cell. A conductive network of conductive particles must exist within the suspension that connects each active particle to the current collector, such that the charge from redox reactions can be injected/collected during charging/discharging of the cell. This network is designed to be percolating, with

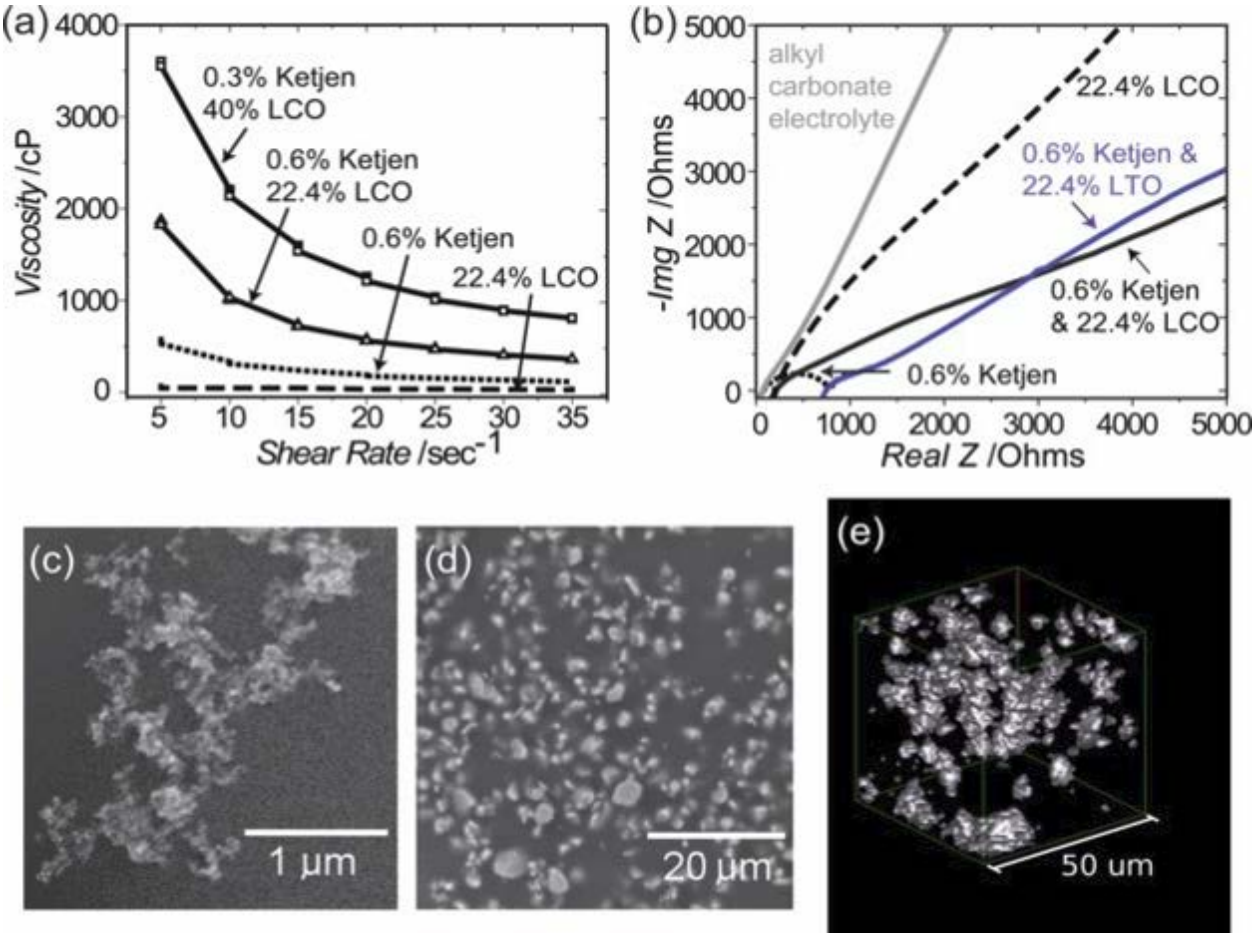

Figure 1.13: (a) shear rate vs viscosity curves (b) EIS impedance curves (c) SEM images of various LCO suspensions. Adapted from [13]

clusters of conductive particles in contact to form many conductive pathways spanning the full volume of electrolyte.

The percolation threshold for carbon black networks, in which they begin to show non-negligible electronic conductivity, has been measured to be ≈1%vol [13, 47]. It has also been reported that the addition of 0.6%vol carbon black led to 10-fold increase in viscosity of a 22.4%vol LCO slurry [13]. Establishing a balance between high particle loading for high conductivity and energy density, and decreasing particle loading to reduce slurry viscosity and decrease mechanical pumping losses remains a central challenge to understanding and optimizing Type 2 flow battery systems.

Dudata et al published the first characterization of Type 2 slurry rheology in 2011, shown in Figure 1.13. In Fig 1.13a, the existence of shear thinning behavior in all LCO-KB slurries is shown, with shear thinning used as an indicator of the existence of particle

network formation within the slurry. This data, coupled with the EIS plots shown in Fig 12b, showed that an ionically + electronically conductive network was formed. Figure 1.13a also highlights the high viscosity (2000-4000cP) nature of the slurries that are typical for a Type 2 cell when both conductive and active materials are co-suspended. Later in the work, they show activity from a static and intermittently pumped cell of LCO/LTO at a discharge capacity of 127 mAh/g, the first example of a Type 2 flow battery in operation [13].

Additives are commonly employed to tune suspension rheology in other fields, and the use of additives has been explored for Type 2 flow batteries. Wei et al. used polyvinylpyrrolidone (PVP) as a steric stabilizer, to control the rheology of their LFP-KB slurries. PVP was introduced to help control agglomerate formation and drive homogenous distribution throughout the particle network. PVP was shown to reduce viscosity (Fig 1.14a) and shear yield stress (Fig 1.14b) of the slurry, while maintaining high electronic conductivity. Static and flow cells showed high capacity (>131 mAh/g) over 100 cycles [47]. Figure 1.14a shows the decrease in viscosity by an order of magnitude with the LFP-KB-PVP blend (labeled Biphasic) compared with the pure LFP-KB suspension (labeled Attractive).

Cell design: In addition to the materials within the cell, the design of the cell hardware presents a new set of challenges for slurry batteries. Two types of cell hardware have emerged from early work on Type 2 flow batteries: a static cell and a flow cell. The static cell is used for testing the properties of the slurry in a battery cell without the slurry being flowed. This design, as shown in Figure 1.15a, is commonly housed in a chemically-resistant polymer Swagelok cell, with stainless steel current collectors on either end for electrical contacts. Anode foils, as well as Celgard separators, can be punched to the appropriate size, and held under pressure via a spring. The slurry needs to be held in a conductive well, to confine it to a well-defined active area and to prevent the compression of the cell from spreading the slurry. This design will be discussed more in a later section. For designs where no separator is desirable, such as only measuring the properties of the slurry via EIS, a design with Teflon walls separating the two current collector is used (Fig 1.15b).

The flow cell, shown in Figure 1.15c, shows an inlet and outlet, to which either a syringe or peristaltic pump are connected, and a syringe filled with slurry is loaded into. The flow channel is machined out of a metal block, which is contacted perpendicularly by a current collecting metal rod. As with the static cell, metal and separator foils are cut/punched out to the appropriate geometry, and the cell is fabricated by stacking the layers of the cell and holding them under pressure via threaded screws.

The thickness of the channel (also thought of as the channel diameter) has shown to be a critical variable in the performance of a Type 2 flow battery. The thickness of the channel sets the thickness of the active layer in the battery. To transport the electrons needed for a redox reaction, a conductive pathway must exist from each active particle to the current collector. Necessarily, there must be a chain or network of carbon that creates this transport pathway. This requirement suggests the farther distance the conductive pathway must span, the greater chance exists of the pathway being incomplete, thereby leaving out active particles from the network. Because this layer is a suspension, electrical conductivity needs to be maintained across the full thickness of the suspension to maintain capacity.

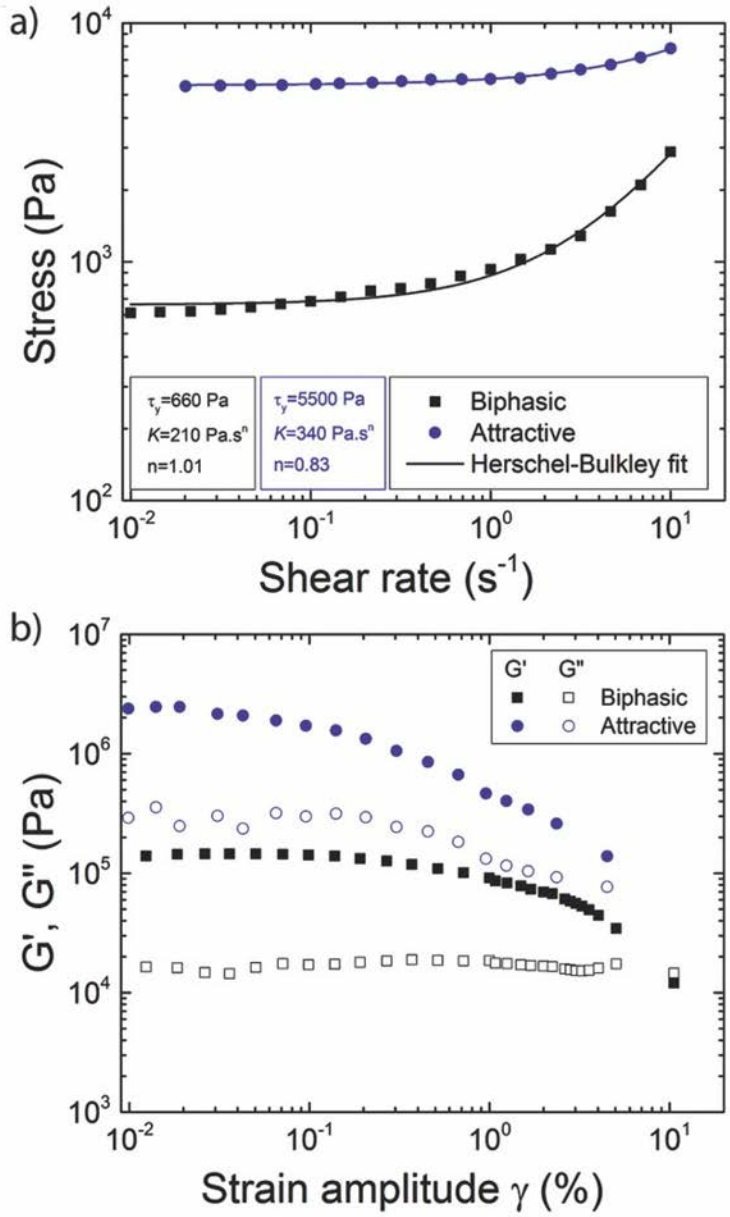

Figure 1.14: Rheological data comparing LFP slurry with (Attractive) and without PVP (Biphasic) additives. Adapted from [47]

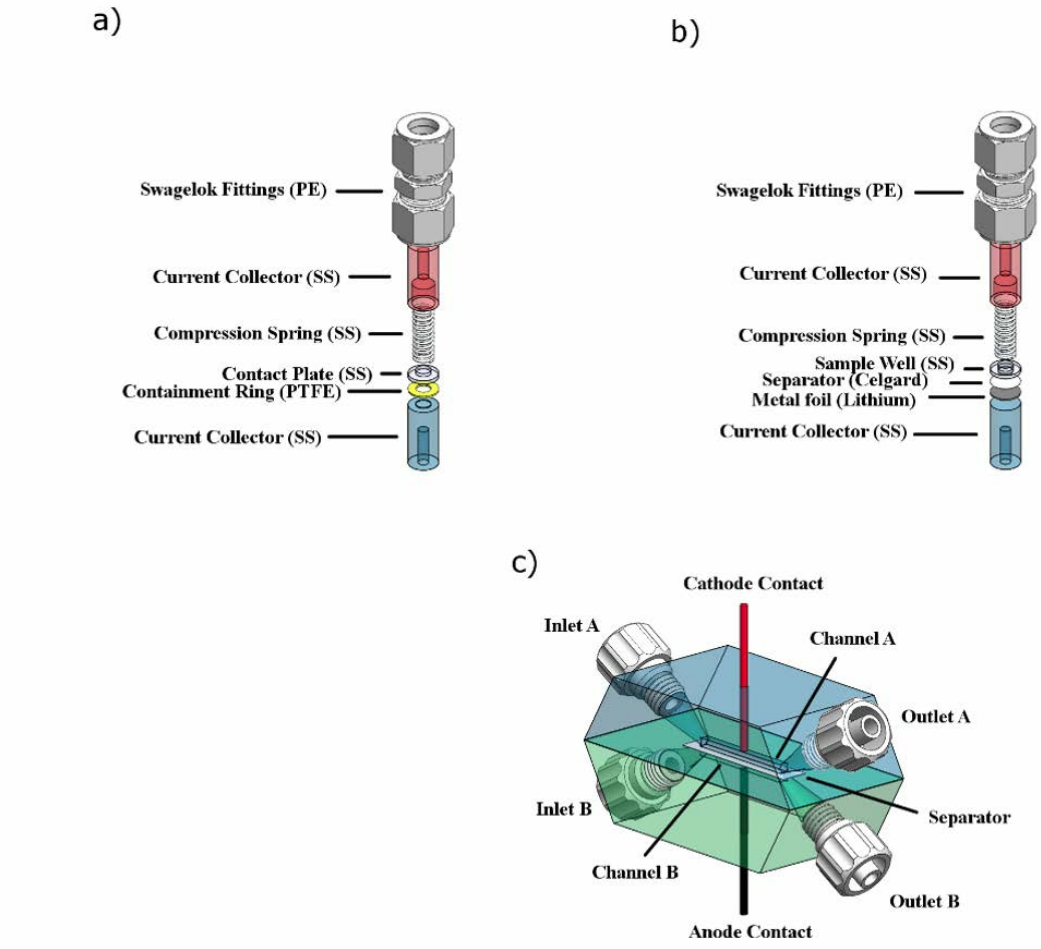

Figure 1.15: (a) Static (b) Conductive/EIS (c) Flow cell hardware designs. Adapted from [47]

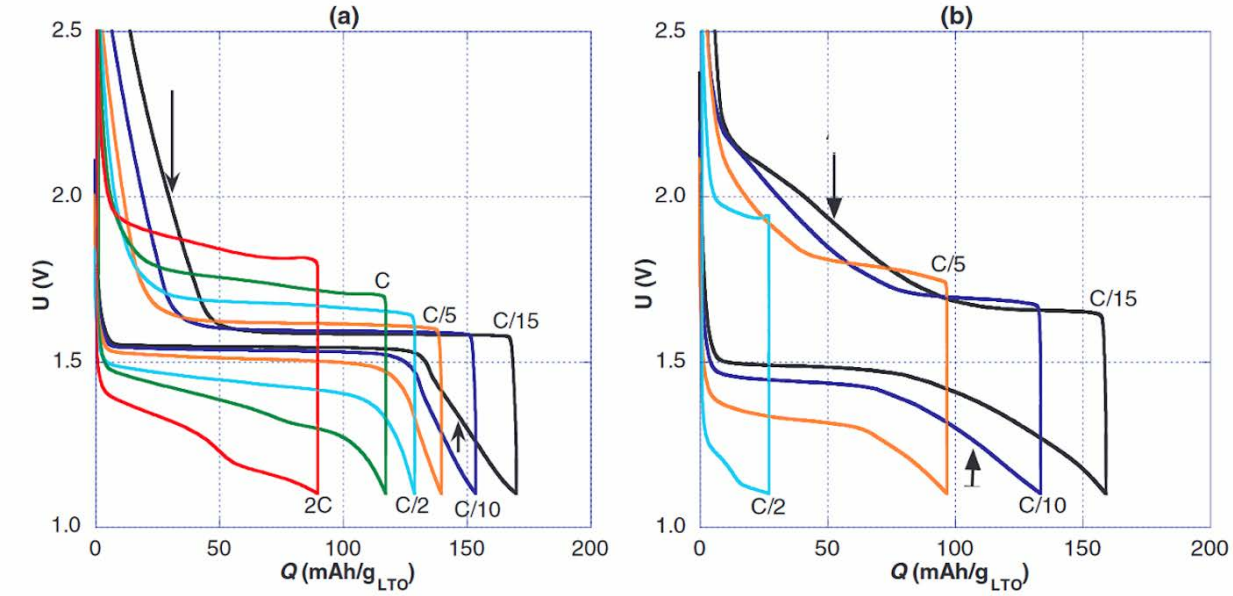

Figure 1.16: Charge/discharge curves of an LTO semi solid suspension at (a) 0.5mm and (b) 1.0mm slurry thickness. Adapted from [48]

Figure 1.16 shows the same LTO/KB slurry being cycled at various C-rates, with a channel diameter of 0.5mm (Fig 1.16a) and 1.0mm (Fig 1.16b). At moderate and high discharge rates, a severe drop in capacity is observed, with 0.5mm showing notably higher capacity in all cases, with the capacity at C/2 rate being 6 times lower for 1.0mm compared with 0.5mm. This result was attributed to a carbon black network that incompletely filled the full volume of the 1.0mm diameter channel, and highlights the difficulty of maintaining a suspended conductive network over large distances [48].

In traditional flow batteries, the spatial extent of the reactions is limited to the solid electrodes and is well defined. In a Type 2 flow battery, the electrode is instead defined by the space over which the conductive network is continuous (the electroactive zone) and could therefore theoretically extend past the edges of the flow channel. Additional particles/agglomerates beyond the edges of the current collector may be electrically wired to the slurry within the current-collector defined flow channel. Smith et al. studied the effect of channel length and discharge rate, and showed that longer channels and higher C-rate discharge (>C/11) minimize the parasitic effect of this additional electroactive zone to <1% total capacity in the LTO system [52].

Performance under flow / pumping: For flow batteries, the effect of flow can be understood through its impact on capacity (performance) and on required pumping energy (loss). Selecting the optimum flow rate highlights the tradeoff between capacity and loss: higher flow rates bring new material or ions into the flow cell at a high rate and can potentially

increase capacity, but high flow rates require more energy to be consumed through pumping, decreasing the energy efficiency of the overall system [53].

The effect of flow and shearing-related phenomena on the capacity of a Type 2 flow battery have not been directly studied. However, work on the effects of shearing in carbon black suspensions in nonaqueous electrolytes suggests important effects of flow rate on electroactive suspensions. Hipp et al. use the inverse Bingham number Bi^{-1}, the ratio of applied shear stress to yield stress, as a metric for how much shear is applied to the slurry under flow. Their work shows that for $Bi^{-1} > 1$, the high flow regime, the applied shear breaks up large carbon black agglomerates and more homogeneously disperses the carbon particles throughout the network. This led to higher conductivities, lower viscosity, and strongly reduced sedimentation of the carbon particles [54]. Connecting the principles explored in their work to the electrochemical metrics of a full battery would help inform future Type 2 flow battery research about how to tune rheology to better apply the effects of flow during cycling.

Brunini et al. suggested that for flow cells which are continuously pumping new material into the channel, the optimum flow rate would cause the material to be fully charged or discharged within one pass through the channel, which they denote as "stoichiometric flow". During stoichiometric flow, a gradient can form across the flow channel, as the state of charge (SOC) varies throughout the channel with new material entering one end of the channel and cycled material exiting the other end. Their electrochemical modeling found that utilizing redox materials with a flat discharge profile eliminated the current density variation in a flow channel during discharging and pumping, and that cells with flat discharge voltage profiles more closely matched their theoretical capacities [55].

The potential losses due to pumping a high viscosity fluid through flow battery are a primary concern for this flow battery variation and were estimated by Dudata et al. in their original Type 2 flow battery paper. For their work, Dudata et al. proposed two pumping methods: continuous and intermittent. Continuous pumping circulates slurry through the flow channel without interruption. Intermittent pumping fills the channel with fresh slurry, stops pumping while the slurry in the channel is discharged or charged, and then once the discharging or charging is complete, pumps just enough slurry to refill the channel with fresh material. The authors calculated that at a 15 mL/min flow rate, 44.12% of the energy produced by the battery would be used for pumping in a continuous pumping scheme, but merely 0.6% of the energy would be lost with intermittent pumping protocol [13]. This result has served as a proof of concept that pumping high viscosity slurries is not energy-cost prohibitive, and has been widely cited throughout the flow battery literature. This has led to intermittent pumping being exclusively used in subsequent Type 2 flow battery cycling protocols.

Type 3

Carbon additives are included in semi-solid flow cells to increase conductivity and ensure pathways for electrons to travel from active particles to current collector, but they can have

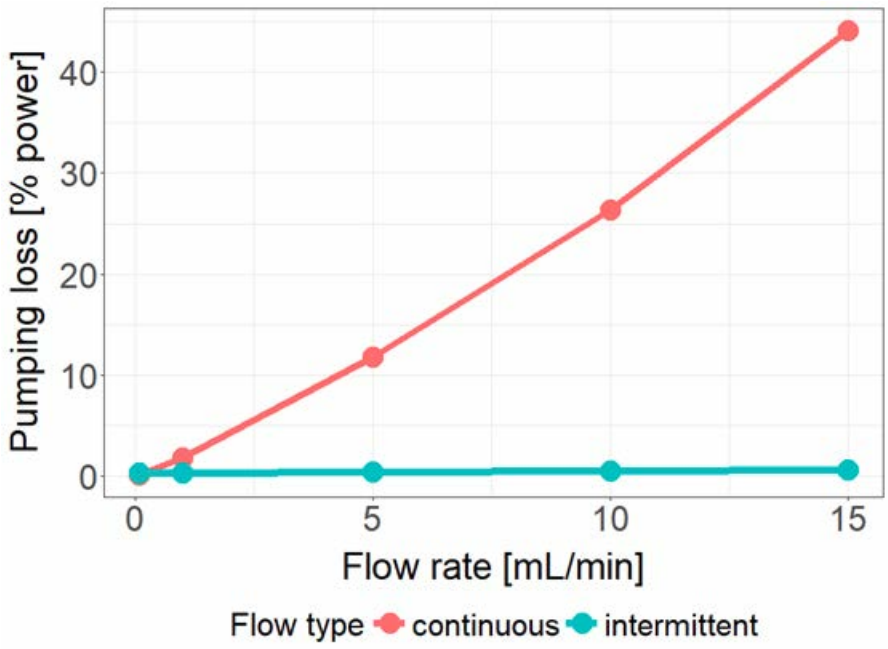

Figure 1.17: The effect of flow rate on estimated pumping loss, for intermittent and continuous pumping protocols. Data plotted from [13]

adverse impacts on the rheology of the flowing media in a flow battery. As noted earlier, the addition of 0.6%vol carbon black to a 22.4%vol LCO suspension increased the viscosity of the suspension by 10-fold [13]. Decreasing the volume of carbon additive is favorable, to reduce suspension viscosity and decrease the volume of inactive material in the cell. In Type 3 flow cells (Figure 1.10c), redox active particles are dispersed in the electrolyte, and no conductive materials are added to the suspension. This suspension architecture seeks the benefits of a flowing active material like in Type 2 systems, without the high viscosity imparted from carbon additives. Without a percolating carbon network to conduct electrons from active particles, Type 3 cells require the active particles to be in physical contact with the current collectors in order to transfer charge [44].

Work from Qi et al. uses the LTO chemistry to demonstrate Type 3 flow cells. As shown in Figure 1.18, their work successfully demonstrates this type of charge transfer but only for short time periods (10 mins), low power densities (0.01 mW/cm) and at low coulombic efficiency (45%) [56]. Similar results were reported in the LCO chemistry [56]. Work on Type 3 cells with redox active colloids demonstrated 21% of theoretical capacity at a low concentration (0.01M) [57]. While Type 3 cells aim for lower viscosity and less inactive material than other solid-containing flow batteries, engineering suspensions and reactor design to increase particle utilization and long-term power output remain substantial obstacles to this new form of redox flow battery.

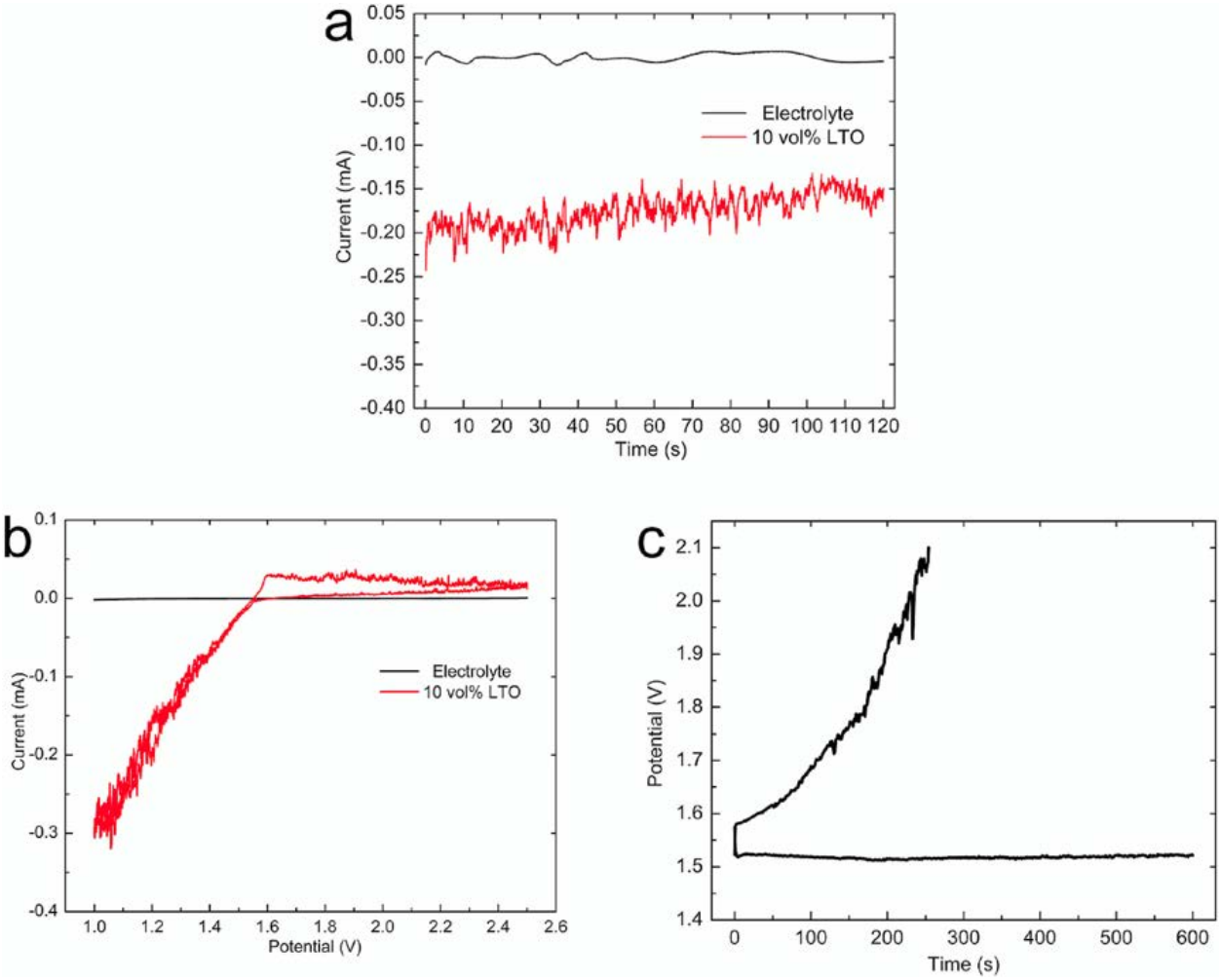

Figure 1.18: (a) discharge (b) cyclic voltammetry (c) cycling behavior of LTO particles in a Type 3 flow cell. Adapted from [58]

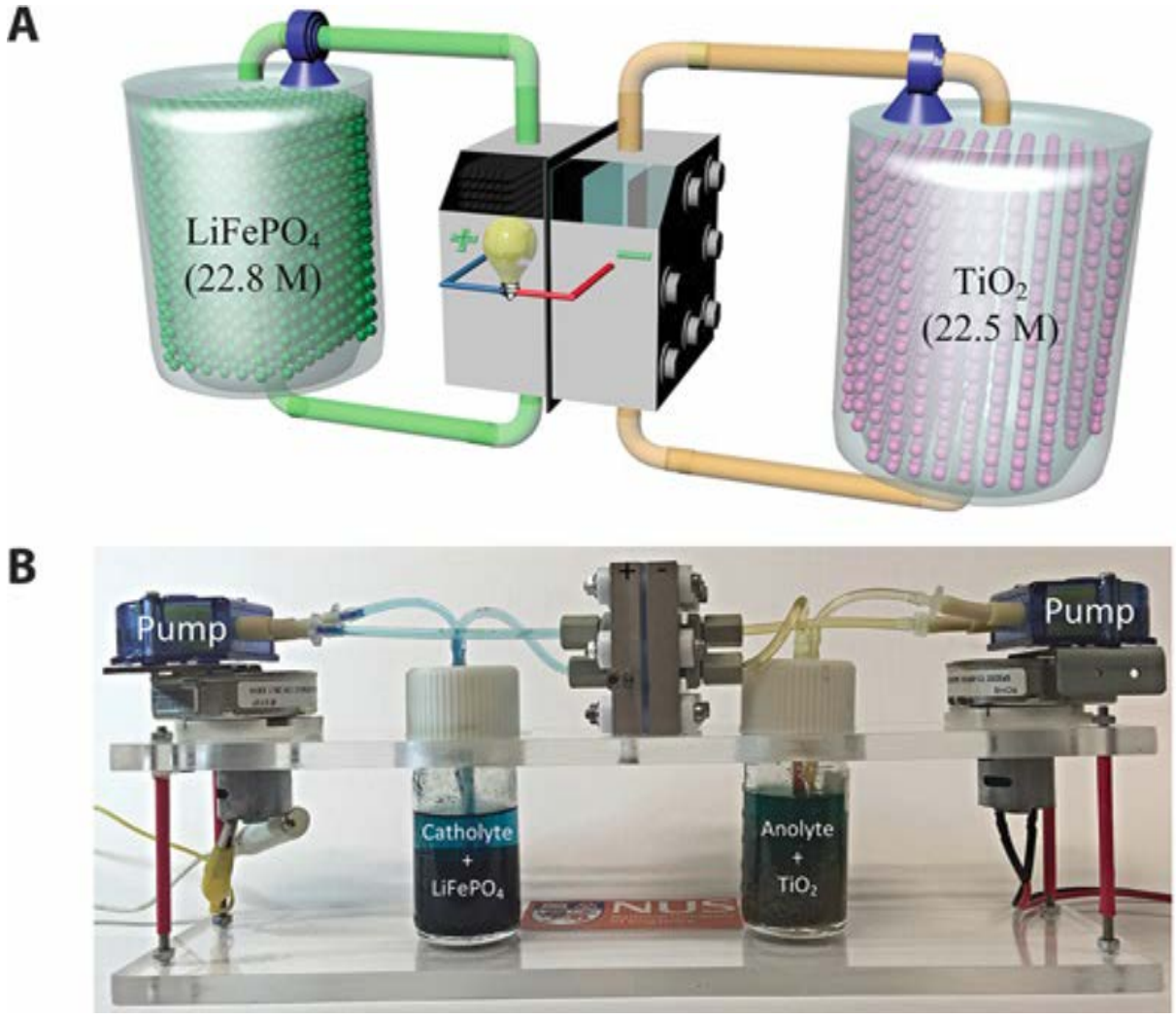

Figure 1.19: (a) System level schematic and (b) Picture of lab setup for Type 4 LFP-TiO_2 flow cell. Adapted from [59]

Type 4

Type 4 flow batteries do not flow suspensions of solid particles in a liquid electrolyte, but instead flow liquid electrolytes through a tank packed full with solid active particles. The electrolyte flowing through the particle bed contains dissolved redox mediators, which are chemical compounds used to shuttle charge between the current collector and active material. Redox reactions occur on the active particle surface, and the resulting charge is transported via mediators through the electrolyte without relying on networks of conductive carbon particles like in Type 2 flow batteries.

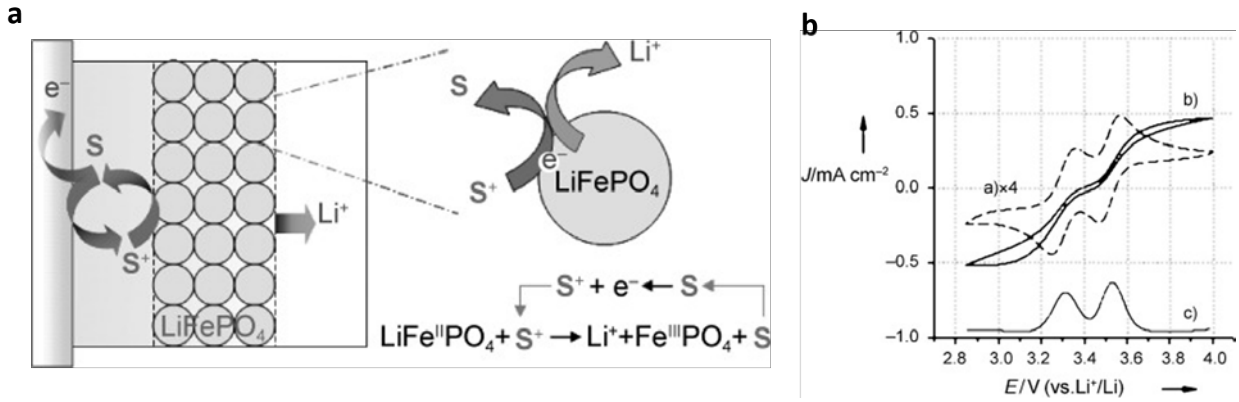

Figure 1.20: Schematic of the redox reactions in Type 4 LFP flow system. Adapted from [60]

Wang et al. first demonstrated the dissolved redox mediator approach via the LFP chemistry [60]. Figure 1.20a illustrates the reaction scheme present in the LFP system, with **S** demarcating the redox mediator. The mediators are chosen such that their energetic alignment with the active material produces charge transfer upon contact, in this case finding that osmium-based had proper energetic alignment [60]. This was confirmed in Figure 1.20b, which shows the cyclic voltammograms of a pristine FTO electrode in electrolyte (solid line, b)) and an LFP-coated FTO electrode in electrolyte (dashed line, a)). Upon adding the redox mediators, new, reversible peaks appear on the LFP-FTO voltammogram that confirm their role in facilitating charge transfer. The authors noted that developing a separator that excluded the mediating species would be challenging and was a limitation in their initial work.

The porosity of the particle bed needs to be controlled to allow electrolyte to flow through. If liquid cannot flow through the powder bed, then a high pressure drop across the tank will be created, and high pumping losses will be incurred to flow the electrolyte. Porosity control is essential for Type 4 systems and may limit the maximum powder loading within the tanks to ensure sufficient porosity [44]. Additionally, as mentioned by Wang et al., redox mediator flow batteries cannot use size exclusion membranes, which are inexpensive and commonly used in other solid-containing flow batteries. The mediator species are dissolved into the electrolyte and, therefore, can only be separated by an ion exchange membrane. Currently, all redox mediator flow batteries use organic solvents, necessitating that the IEM is stable in organic solvents. This is not common, as IEMs have been almost exclusively designed for aqueous and acidic environments such as vanadium flow batteries, and may require substantial research to develop for Type 4 cells [44].

Conclusion

Despite focused efforts to avoid expensive vanadium salts and ion exchange membranes, realizing high solubility and low cost active materials remains a challenge for redox flow batteries. Solubility remains a limitation for vanadium and organic systems, while the intrinsic materials challenges of sulfur and metal-air systems threaten their usability in flow systems. The novel approach of semi-solid flow batteries offers a route around solubility limits, but low cost materials are not well explored. In the remainder of this work, we focus on designing and demonstrating low cost materials for semi-solid flow batteries- as a route to low cost, high energy density redox flow batteries.

Chapter 2 establishes the criteria for material selection for our low cost slurry flow battery. A theoretical basis for a general slurry battery is developed, and the requirements and desired traits of each component are explained. The rationale for the active materials used in our system, a metal foil Mg anode, MoS_2-KB cathode slurry, dual-ion Mg/Li electrolyte, and Celgard polymer separator, is explored in this chapter. The specialized cell hardware for a non-flowing and flowing cell is described and illustrated.

Chapter 3 outlines the core suspension characteristics needed for semi-solid battery operation, and presents relevant rheological, electrical, and electrochemical measurements used to investigate those characteristics. These results are used as evidence of particle-to-particle contact within the formed suspension, and to quantify both ionic and electronic conductivity within the suspension. Cyclic voltammetry measurements show the role of Li intercalation in this dual ion system, and begin to justify the performance difference observed in low-KB and high-KB systems. The charge-discharge capacity measurements presented in this chapter are the first ever demonstrations of a magnesium semi-solid battery.

Chapter 4 focuses on quantifying the role that Mg and Li ions have in providing reversible capacity in a Mg/MoS_2 slurry battery. Cells with either Li or Mg ions are shown to have negligible reversible capacity, solidifying the need for a dual-ion system. ICP measurements establish Li as the ion responsible for the majority of capacity, but show that Mg is actively participating in the cathode-side reaction. An optimal level of Li ions in the electrolyte is characterized and presented.

Chapter 5 characterizes the performance of the optimal MoS_2 slurry, at varying discharge rates and in both non-flowing and flowing hardware. The measurements shown in this chapter benchmark the performance capabilities and limitations of this slurry flow battery system. Relevant C-rates for practical applications are discussed. Cycle life measurements are provided to gauge the ability of the MoS_2-KB slurries to withstand repeated charge-discharge cycles. Contrasts between the non-flowing and flowing cells are drawn and examined.

Chapter 6 provides a review of the results presented in this work, as well as a discussion of potential future research directions.

Chapter 2

Designing an Intercalation-based Redox Slurry

2.1 Overview of semi-solid (slurry) battery design

The operation and structure of semi-solid batteries show several analogous properties to standard coin/cylindrical cells: ion and charge transport to the active material must be simultaneously achieved to deliver reversible capacity. In traditional cells, electrodes are formed from slurries, consisting of active, conductive, and binder materials mixed in a solvent. These electrode slurries are then cast, dried, sintered, and calendared- leading to compact, freestanding electrode films [61]. Figure 2.1 shows the steps in a traditional electrode fabrication process. The electrode films can be thought of as a particle network that is both sintered and compacted. The challenge for semi-solid (slurry) batteries is achieving ionic and electronic conductivity from a particle network that is suspended in a liquid, and does not have sintering or calendaring mechanisms to promote particle-particle contact.

In order to host redox reactions, electrons and ions must be transported to the active particles within a battery electrode. Ion conduction occurs from electrolyte-active particle contact; electrode films are wetted with electrolyte during cell fabrication to enable ionic conductivity throughout the film (see the final step in Fig. 2.1). Electron conduction is possible when an active particle is electrically connected to the external circuit via a current collector. Electrical connection to the current collector occurs under two conditions: 1) direct active particle-current collector contact 2) via chains/networks of conductive particles that are in contact with both the active particle and the current collector. As a low percentage of active particles are able to be in direct contact with the current collector simultaneously, chains of conductive particles are the most common route to electrically connecting active particles to the current collector. Conductive materials, typically carbon blacks, are added to the electrode to form conductive chains/networks [62].

Electronic conductivity in an electrode occurs when the percolation threshold is reached. The percolation threshold of a particle network is the mass/volume concentration of a particle

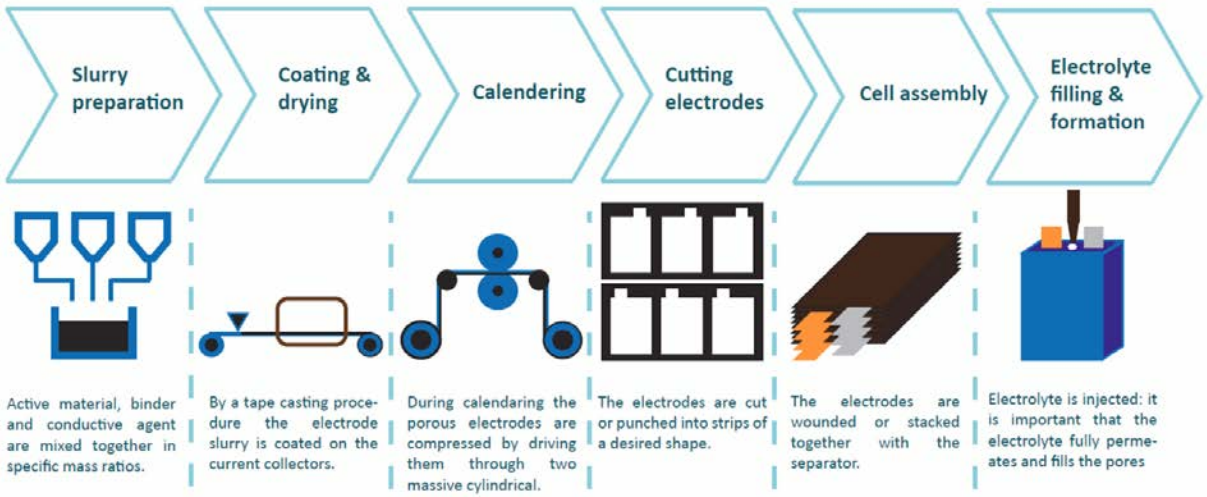

Figure 2.1: Fabrication steps for mass-produced traditional battery electrodes. Adapted from [61]

at which long range connectivity begins to be exhibited within the particle network. For particle networks of conductive materials, the percolation threshold refers to the mass/volume concentration of the conductive material at which non-negligible conductivities are measured in a particle system [63]. The mass/volume loading at which percolation is reached is typical around 1-5 wt%/vol% [64], and is known to vary by particle size, aspect ratio, and material choice [65, 66]. Percolation represents the minimum threshold at which non-negligible conduction is measured; additional increases in conductivity are observed with the addition of conductive material above the percolation threshold. Fig 2.2 illustrates various states of a dispersed carbon black particle network. The percolation threshold is expected to exist between Fig 2.2a and Fig 2.2b, where long range connectivity is formed. In a slurry flow battery electrode, conductive pathways like shown in orange in Fig 2.2b or Fig 2.2c are required to transport electrons from active sites to current collectors.

Slurry electrodes also require ionic and electronic conduction. Ionic conduction to the active material occurs via the electrolyte in which the particle network is suspended. Slurry electrodes are believed to rely on suspended networks of conductive particles for electron conduction between active particles and current collectors [13, 67]. Electronic conduction is more challenging, as particle-particle contact is not developed via sintering/compression as in traditional battery electrodes.

To form a suspension of active and conductive materials, the active and conductive particles are dispersed in the battery electrolyte. Dispersion can be accomplished via a variety of mixing methods, with probe-tip sonication, bath sonication, and ball milling among the most common [68]. Each dispersion process induces collisions between particles, with a

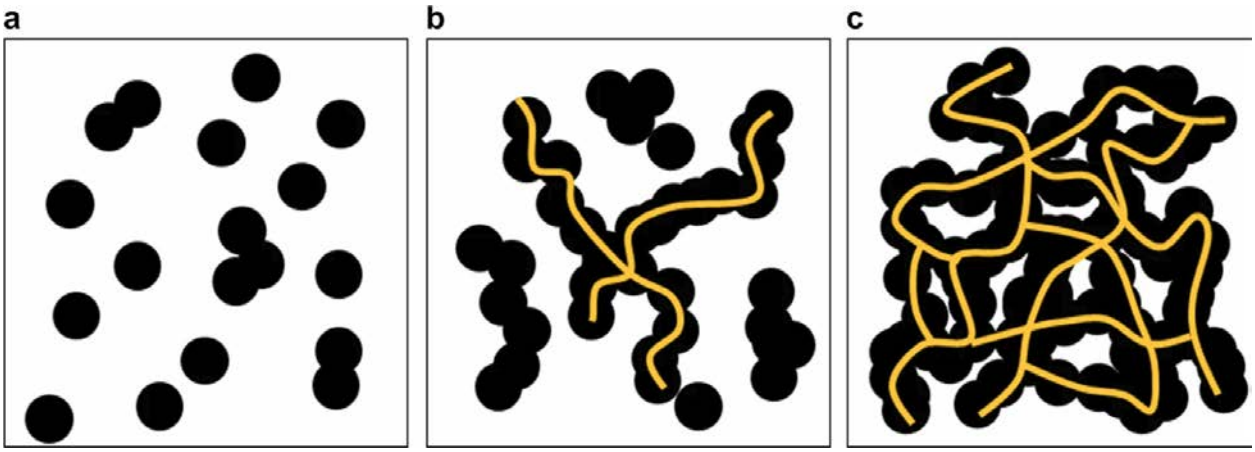

Figure 2.2: Different states of carbon black network (a) disconnected (b) partially connected (c) fully connected. Adapted from [63]

fraction of these collisions leading to "hit-and-stick" behavior, where particles coalesce into groups (known as agglomerates) that maintain contact after the collision occurs [69]. Ideally, these agglomerates are also connected to other agglomerates, and these large networks of active and conductive particles then allow ion and electron conduction to/from each active particle.

The remaining sections of this chapter detail the design and material selection of the anode, cathode, electrolyte, current collector, separator, and cell hardware used in this work to create a novel semi-solid flow battery system.

2.2 Anode

In previous slurry flow battery work, both anodic and cathodic slurries have been developed [13]. Figure 2.3a illustrates a slurry flow battery with anodic and cathodic slurries, labeled as anolyte and catholyte as is conventional in flow battery literature. For this project, the anode was chosen to be a metal foil, to simplify the cell design and maintain focus on the cathodic slurry. Metal foils are attractive in half cell assemblies, as they provide an excess of ions for the other half cell redox reaction, and are easily integrated during cell fabrication. Figure 2.3b illustrates the cell architecture used in this work.

Prior work has investigated slurry flow batteries with lithium redox couples, with some work using Li metal foil anodes and several works developing Li anodic slurries [13, 70, 71]. Lithium metal foils are ≈10x more expensive than alternative anode materials such as Na or Mg [72, 29, 73]. In an effort to use low cost materials, while simultaneously expanding the material catalog that has been explored with slurry flow batteries, the anode selection was limited to non-Li metals.

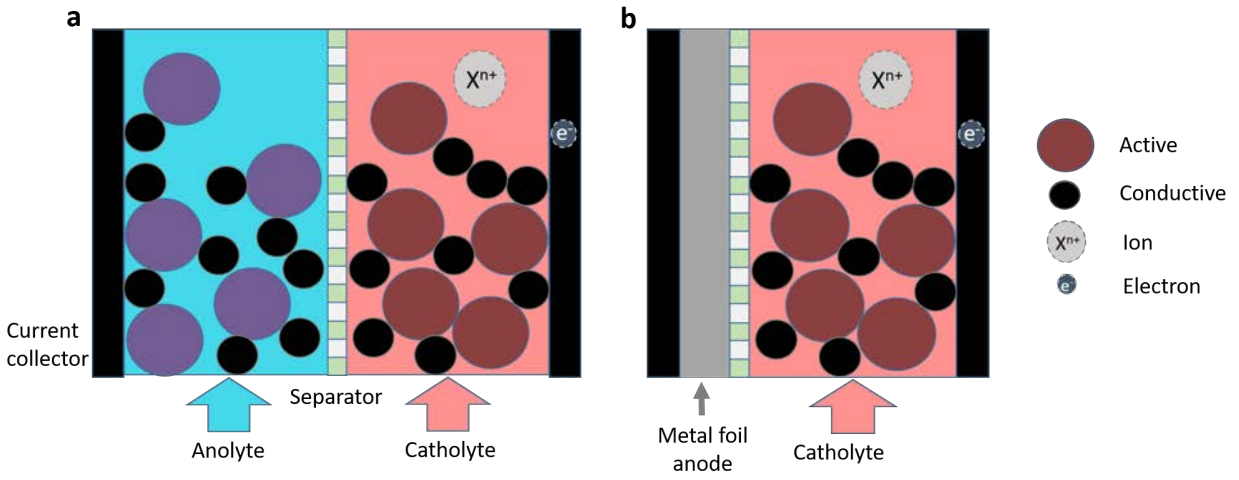

Figure 2.3: Illustration of semi-solid (slurry) flow battery with (a) slurry anode (b) metal foil anode

Magnesium metal foil anodes

Magnesium has undergone extensive research for decades, as an alternative to lithium as a battery anode material. Magnesium is highly abundant, with an abundance in the earth's crust that is ≈1000 times greater than lithium [74]. Its lower raw material cost reflects this increased supply, with prices currently at \$2-5/kg for Mg metal and \$50-80/kg for Li metal [72, 29, 73]. When incorporating the theoretical capacity of both materials, the cost-per-charge, or \$/kAh, still compares favorably: \$2/kAh for Mg, \$13/kAh for Li. The material characteristics for both Mg and Li are summarized in Table 2.1 below.

	Magnesium (Mg)	Lithium (Li)
Abundance (per 10^6 atoms Si)	10^5	10^2
Annual production (kg/yr) [75]	6.3 x 10^9	2.5 x 10^7
Price (\$/kg)	2-5	50-80
Theoretical capacity (mAh/cm^3)	3833	2061
Theoretical capacity (mAh/g)	2062	3861
Cost per charge (\$/kAh)	2	13
Voltage (V)	-2.37	-3.04

Table 2.1: Key battery material metrics for Mg and Li metals

Magnesium metal has a high volumetric energy density (Table 2.1), allowing it to deliver a high capacity for a relatively small volume of material. Magnesium metal foils have also

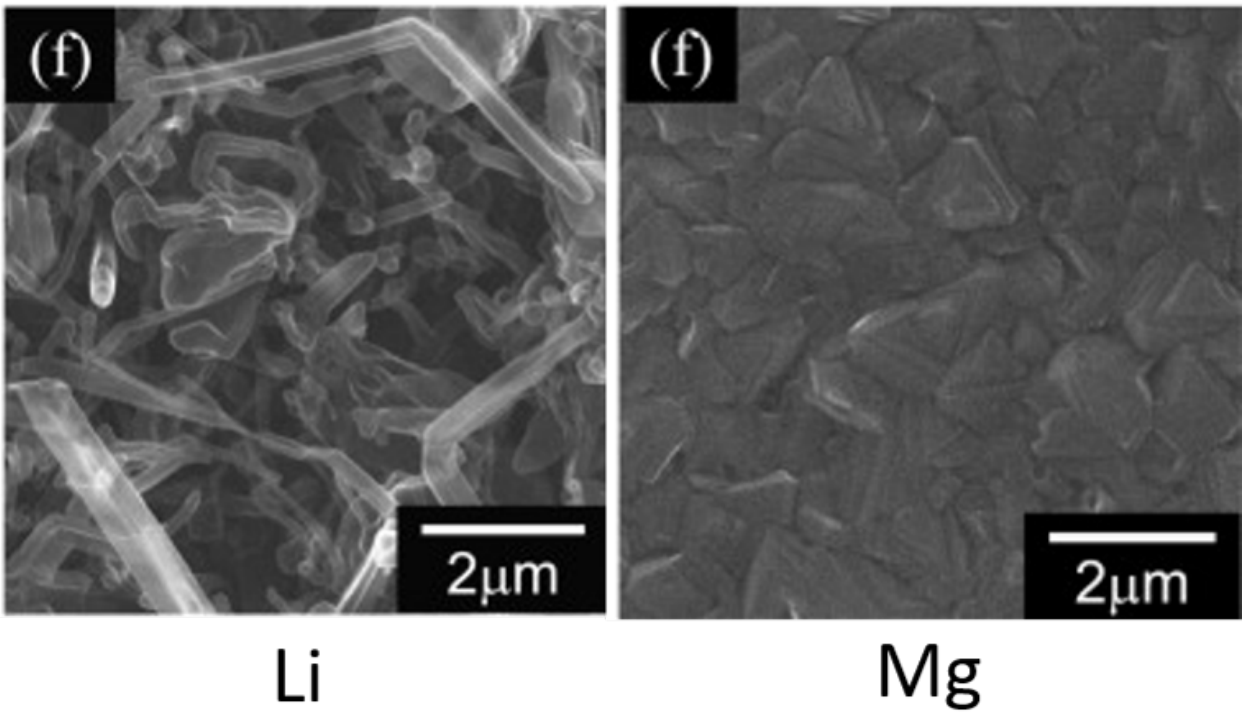

Figure 2.4: SEM images of the anode surface in a cycled (left) lithium and (right) magnesium battery. The rod-like shapes on the lithium surface are dendritic growth, the magnesium surface shows smooth, uniform plating. Adapted from [78]

been shown to have a low propensity for developing dendrites [76]. While dendrites under certain electrolyte/cycling conditions have been shown [77], Mg metal is considered dendrite-free under most operating conditions. This removes a key obstacle encountered in Li metal batteries, and is a significant advantage of Mg metal anode systems.

Magnesium has seen significant research in literature, establishing a number of electrolytes and cathodes to choose from [79, 80]. Despite this, magnesium had not yet been explored in the semi-solid flow battery literature- and therefore represented a path to expand the current library of material choices in SSFBs.

2.3 Cathode

With a magnesium anode, Mg^{2+} is the primary working ion. To produce a full cell with reversible capacity, a cathodic half cell needs to be selected.

The three primary charge transfer mechanisms in rechargeable batteries are intercalation,

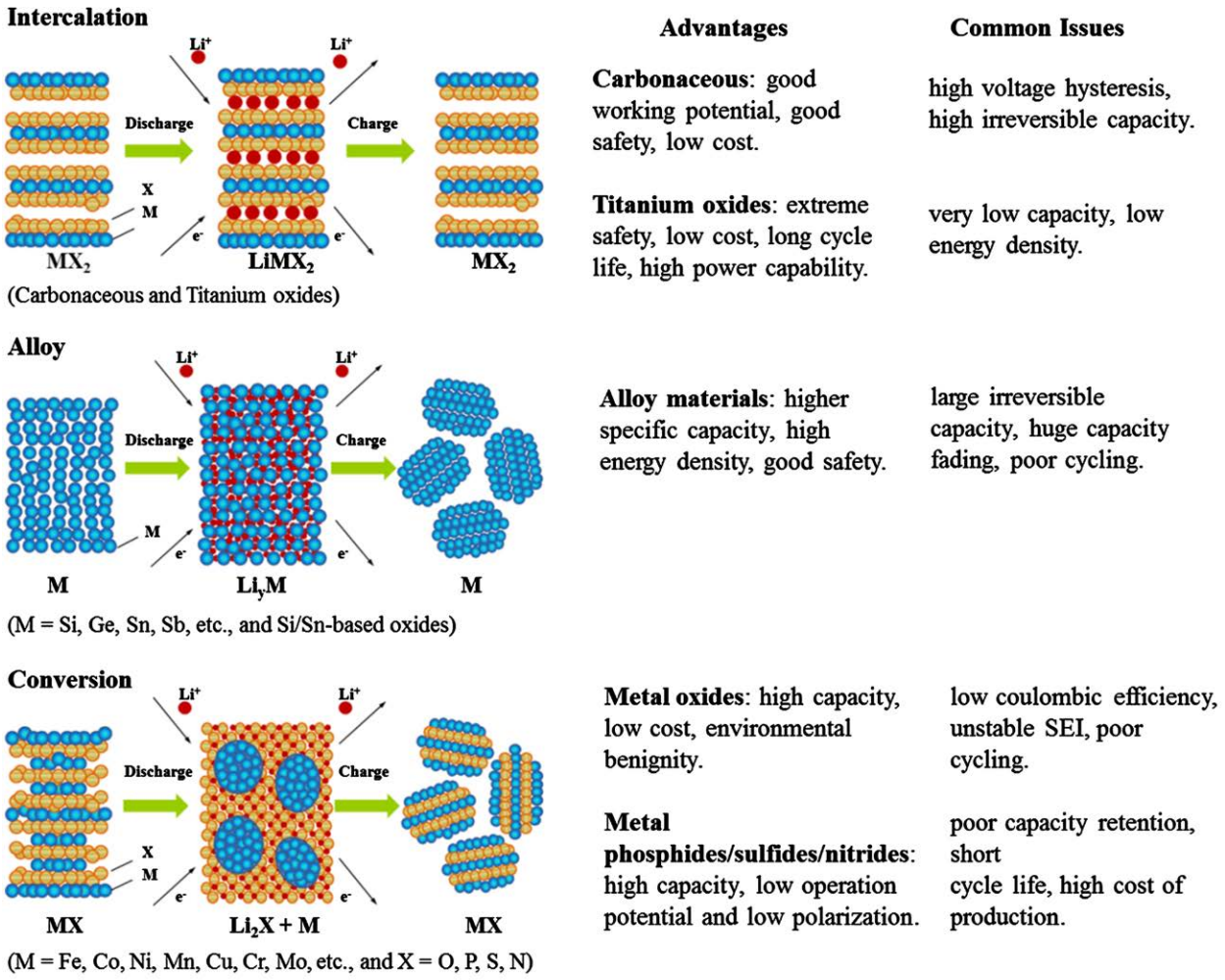

Figure 2.5: The three primary charge transfer mechanisms found in rechargeable batteries. Adapted from [81]

alloying, and conversion. Each mechanism is depicted in Figure 2.5. Alloying and conversion chemistries typically offer high capacity, with the downside of poor reversibility and stability. Intercalation is the most widely studied of the three mechanisms, and is common in commercial batteries due to its stability and high cycle life. For this work, the selection of cathodic chemistries was limited to intercalation compounds, as stability and longevity provide a reliable base through which to study the effect of a slurry electrode.

Intercalation, as illustrated in Fig 2.5, is the process during which an ion is inserted between two layers of a layered material without significantly changing the host structure. During the discharge of a cell, this insertion event causes a redox reaction, which requires an electron to be drawn from an external circuit. During charging, the ion is deintercalated from the host structure, and this redox reaction produces an electron that is injected into the external circuit, producing current. The stability of the layered host structure against deformation during insertion/removal, and the rate at which an ion can insert and remove from these layers are generally the two key criteria for a high capacity intercalation compound.

Compared with other ion systems, Mg^{2+} has slow intercalation kinetics, and many traditional layered materials previously used in Li batteries show negligible capacity in Mg systems [82]. The atomic radius of magnesium (0.72Å) is smaller than lithium (0.76Å), yet the capacity in similar cathode materials consistently favors Li [83].

The origin of slow kinetics in Mg^{2+} systems is the higher electrostatic force present when the high valence state of the Mg^{2+} ion is in close proximity to the layered structure. This electrostatic force acts to repel the ion, preventing its insertion into the layered structure [84]. Fig 2.6 illustrates the enhanced electrostatic force present with Mg ions with the lightly shaded spikes surrounding the atom. Previous work on MoS_2 showed that by increasing the interlayer spacing from 0.615nm to 1.45nm (and thereby decreasing the electrostatic interaction between ion and the nearby layers), a 100-fold increase in Mg mobility was measured [84]. A limited number of cathodes that intercalate the Mg^{2+} ion is currently the most substantial bottleneck in magnesium battery development.

Cathode criteria

The requirements for a cathode in this magnesium-based system, similar to all grid scale battery systems, centered around cost and capacity.

Low cost: To meet the ambitious cost targets of grid scale storage, all materials within the cell are chosen to have low cost. As raw material cost is often the cost-limiting factor in long-duration storage, having low material cost is of high importance.

High capacity: While cost is the ultimate metric of success in grid scale storage, achieving high capacity per weight or per volume can bring down the system cost per kilowatt-hour, as less raw material is required to achieve the same capacity. The search for a cathode was limited to existing intercalation materials, to leverage their high energy density and demonstrated capacity in literature. Specifically, cathode materials that intercalate Mg were under consideration.

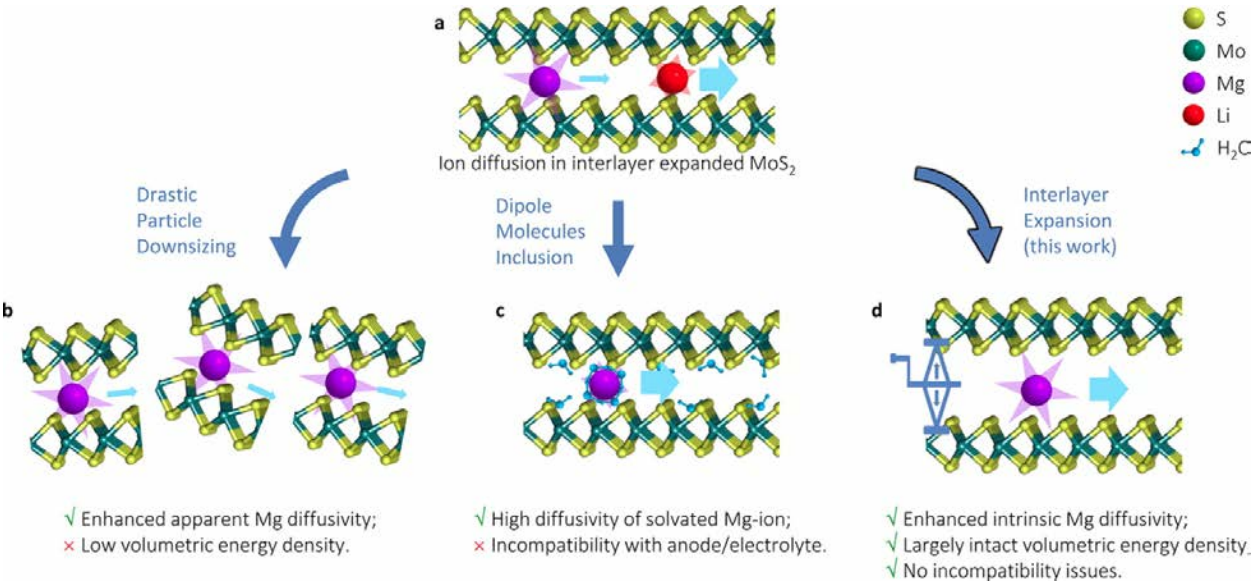

Figure 2.6: Illustration of (a) Mg vs Li transport in layered MoS_2 (b-d) possible pathways to enhance Mg diffusion. Adapted from [84]

Low capacity fade: Grid scale applications have high cycle life requirements, and therefore require materials with low capacity fade per cycle. Capacity fade, as observed in coin cell batteries, can be used to benchmark the rate of degradation in a more optimized battery system. The capacity fade in a novel slurry design will likely be more severe than observed in coin cells, as is explained in later sections. Choosing a material with low capacity fade in existing coin cell literature offers a reference point, from which any observed capacity fading in a slurry electrode can be compared.

Off-the-shelf availability: An ideal cathode material is low cost and already commercially available. By requiring off the shelf availability we restrict our options to mature materials that are presently available in higher volumes. By purchasing a material off-the-shelf, the time and resources normally required for synthesis could be channeled into other aspects of this project.

2.4 Electrolyte

Electrochemical stability window (ESW): Also known as the voltage stability window, the ESW is defined as the voltage range over which an electrolyte does not oxidize or reduce, and does not oxidize/reduce the current collectors that are in direct contact with the electrolyte. Most Mg cathode materials operate between 0-2V vs Mg [85], in which case an electrolyte-current collector pair with an ESW of 2V would be sufficient to avoid decompo-

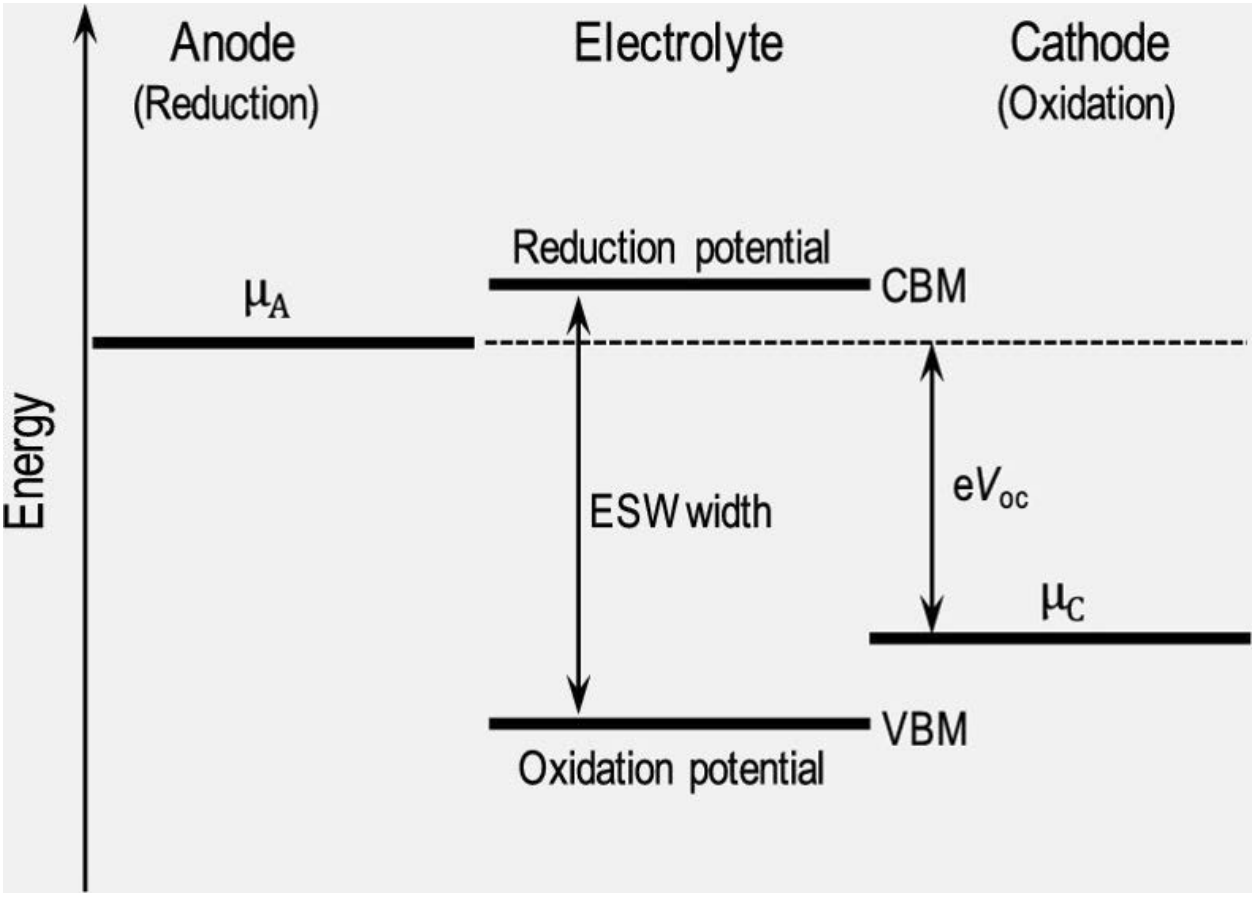

Figure 2.7: Illustration of electrochemical stability window (ESW) in a anode/electrolyte/cathode system. Having the u_A and u_C within the ESW ensures no decomposition from electrolyte-current collector oxidation/reduction during cycling. Adapted from [86]

sition of the electrolyte and current collectors during cycling. Generally lower cost metals (copper, aluminum, stainless steel) have a lower stability window than higher cost metals (gold, platinum), so a balance between cost and stability may be required.

In many other battery material systems, such as lithium ion, SEI (solid electrolyte interface) formation is directly linked to ESW. In these systems, the electrolyte is deliberately reduced, with the reduction products forming a thin film, ion-conducting barrier on the anode surface that acts as protection during cycling, and is critical to the high capacity and lifetimes observed in Li-ion systems. The SEI formation process is highly complex, and substantial efforts to understand and optimize SEI formation continue, both in research labs and in mass-production facilities [87]. A key feature of current Mg chemistries is their homogeneous, reliable plating and stripping on the anode, during which an SEI is not formed

[88]. By removing the need for SEI formation, the complexity of Mg chemistries is greatly reduced.

High ionic conductivity: High ionic conductivity is desirable for high rate performance. In slurry battery systems, electronic conductivity is expected to be rate-limiting, and there are no demonstrations of high rate performance, decreasing the priority on ionic conductivity [13].

Toxicity: In a storage application, large volumes of the electrolyte will be present in any full scale design. In some flow battery chemistries (particularly bromine-based systems), the use of highly toxic chemicals has been criticized for its potential impact to the surrounding environment (human/wildlife/water/soil) [89]. For this work, materials with highly toxic chemicals were avoided.

Ease of synthesis: While synthesis is expected for electrolytes in a novel battery field, some electrolyte synthesis procedures were deemed so complex and time-intensive that they would be a major bottleneck in battery development. These materials were excluded.

Dual salt electrolytes to enable cathode materials

As ions other than lithium are of increasing interest to the battery community, the search for cathode materials that intercalate novel ions (Mg, Na, K, Al, Zn) represents a challenge. While lithium is able to readily intercalate into many layered cathode materials, ions with a higher valence state (such as Mg^{2+}) are not able to intercalate into many of the same compounds. Significant research into novel cathode materials that intercalate Mg ions is underway, as this is currently the primary bottleneck in advancing Mg batteries.

To increase the pace of battery research, utilizing existing cathode materials is ideal as many existing cathode options have already been identified to have low cost and high capacity. Dual salt electrolytes have been examined for the purpose of integrating existing cathodes with novel ions. In this work, we will use the term 'dual salt electrolyte' to refer to electrolytes with two working ions present in solution. This is commonly achieved by synthesizing an electrolyte with one ion, and then dissolving a salt containing the second ion into the electrolyte. For example, a Mg electrolyte is synthesized, and then a lithium salt is added- leaving Mg^{2+} and Li^{+} ions in the electrolyte.

Dual salt electrolytes enable a broader range of cathode materials to be used with a given anode, in one of two ways:

1) The primary ion reacts exclusively at the anode, while the secondary ion intercalates/deintercalates into the cathode. In this case, there are two separate reactions at the anode and cathode, with a different working ion in each half cell.

2) The secondary ion causes a phase transformation at the cathode, and after the phase transformation, the transformed cathode material can now intercalate the primary ion in subsequent cycles.

Dual salt electrolytes are often demonstrated in battery cells where the anode is a metal foil. In these systems, the primary ion plates/strips on the anode, but the secondary ion does not [90]. This is commonly verified via EDX on the surface of the anode, looking for

the chemical presence of the secondary ion after a full plating cycle has been run [91]. The secondary ion reacts with the cathode material, shuttling in/out of solution during cycling.

For the purpose of this work, we will be utilizing a dual salt electrolyte in which the secondary ion causes a phase transformation in the cathode material. This mechanism will be explained further in the next section.

Cathode-electrolyte pair selection

Choosing a cathode material: MoS_2

Based on the cathode constraints listed in Section 2.3, molybdenum disulfide, or MoS_2, was identified as a promising cathode material. A list of material properties is presented in Table 2.2, but in summary, MoS_2 is inexpensive, has high theoretical capacity, is commercially available, and has been successfully demonstrated with a variety of working ions [92, 93, 94, 95, 96].

Theoretical capacity	669 mAh/g [97]
Cost	\$5-10/kg [97]
Crystal structures	1T, 2H, 3R [79]
Density	5.06 g/cm^3
OCV (vs Mg)	1.8V [95]

Table 2.2: MoS_2 material properties

MoS_2 is most commonly available in its semiconducting 2H phase (2H-MoS_2), as depicted in Fig 2.8b. However, it has been shown that Mg ions do not readily intercalate into the 2H-MoS_2 [98]. In Figure 2.10a, we see a Mg-MoS_2 coin cell battery, in which 2H-MoS_2 is used, and negligible capacity is observed.

The role of Li-ions

From the literature on Li-MoS_2 batteries, it is known that Li intercalation into MoS_2 during the first discharge causes a phase transformation, transforming 2H-MoS_2 to 1T-MoS_2 [100]. Figure 2.9 shows in-situ XRD data, where Li intercalation causes a phase transformation in the MoS_2, and the corresponding 2H $\rightarrow$ 1T transition can be directly observed through the decline of the (002) peak and rise of the (001) peak.

The 1T, or metallic MoS_2 phase, has a greater interlayer spacing- and Mg ions have shown to intercalate into 1T-MoS_2 in battery systems [98]. To accomplish this phase transformation, Li^+ is added to the Mg-based electrolytes, and a first discharge cycle is run. Similar to the Li-only system, a distinct voltage profile exists in the first cycle, corresponding to the phase transformation. In Figure 2.10b, we see the first cycle of a Mg/MoS_2 battery with a Mg+LiCl electrolyte, and see the characteristic first cycle, with a voltage plateau at $\tilde{0}$.2V vs Mg. This

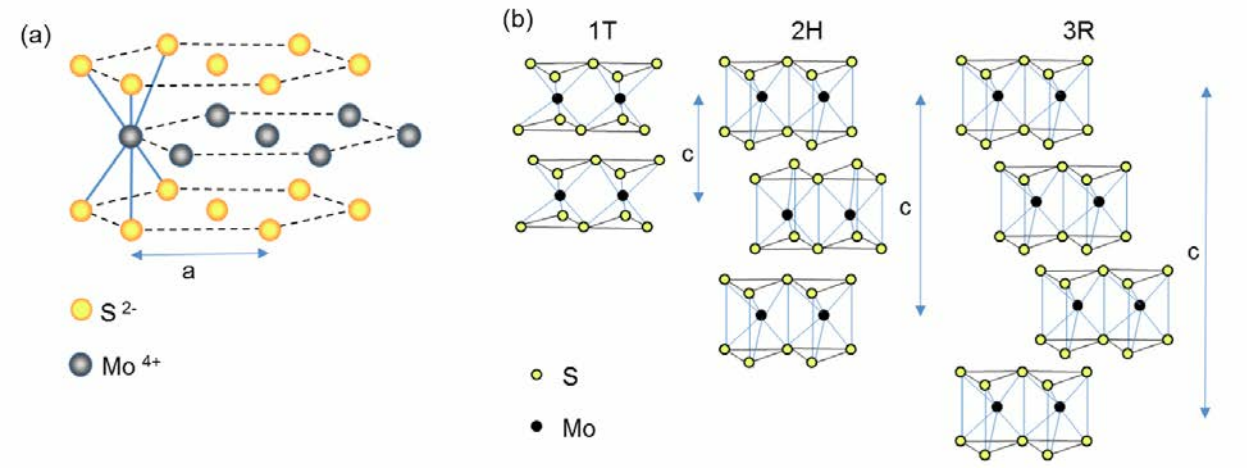

Figure 2.8: (a) General arrangement of Mo, S atoms in MoS_2 molecule (b) crystal structures of MoS_2. Adapted from [99]

plateau is also observed in the CV plot, in Figure 2.10c. Figure 2.10d shows the same Mg-LiCl electrolyte, but cycled down to 0.4V, and the lack of capacity in subsequent cycles is apparent.

The use of Li as a secondary ion enables high capacity operation in MoS_2, and only requires 1 formation cycle to enable the incorporation of an inexpensive, off-the-shelf cathode in a magnesium battery. Therefore, MoS_2 was selected for the cathode, and LiCl solubility became an additional constraint to the electrolyte selection process.

Choosing an electrolyte: all-phenyl complex (APC)

The electrolyte needed for this system required high ionic conductivity, a wide electrochemical stability window, a robust and widely repeated synthesis protocol, and LiCl solubility. The all phenyl complex, or APC, was selected for its performance and versatility.

The APC electrolyte was developed in 2008 in Doron Aurbach's group, after nearly a decade of work focused on increasing the ESW from 0-2V to 0-3V vs Pt [101]. It has been shown since that the phenyl rings present in APC impart stability on the electrolyte, and prevent oxidation at higher voltages, which made it the first Mg electrolyte to show high voltage (3V) stability. APC has almost universally been the electrolyte of choice for dual salt magnesium batteries, as LiCl has high solubility (≈1M) in THF [102]. The synthesis protocol is straightforward, dissolving and mixing commercially available aluminum chloride and THF with phenylmagnesium chloride in THF [101]. Ionic conductivity of 3-4 mS/cm, among the highest of Mg electrolytes, has been measured over a variety of temperatures [101]. The APC electrolyte has been studied with a wide variety of cathode materials, and has demonstrated strong compatibility with Mg foils and Celgard separators through these

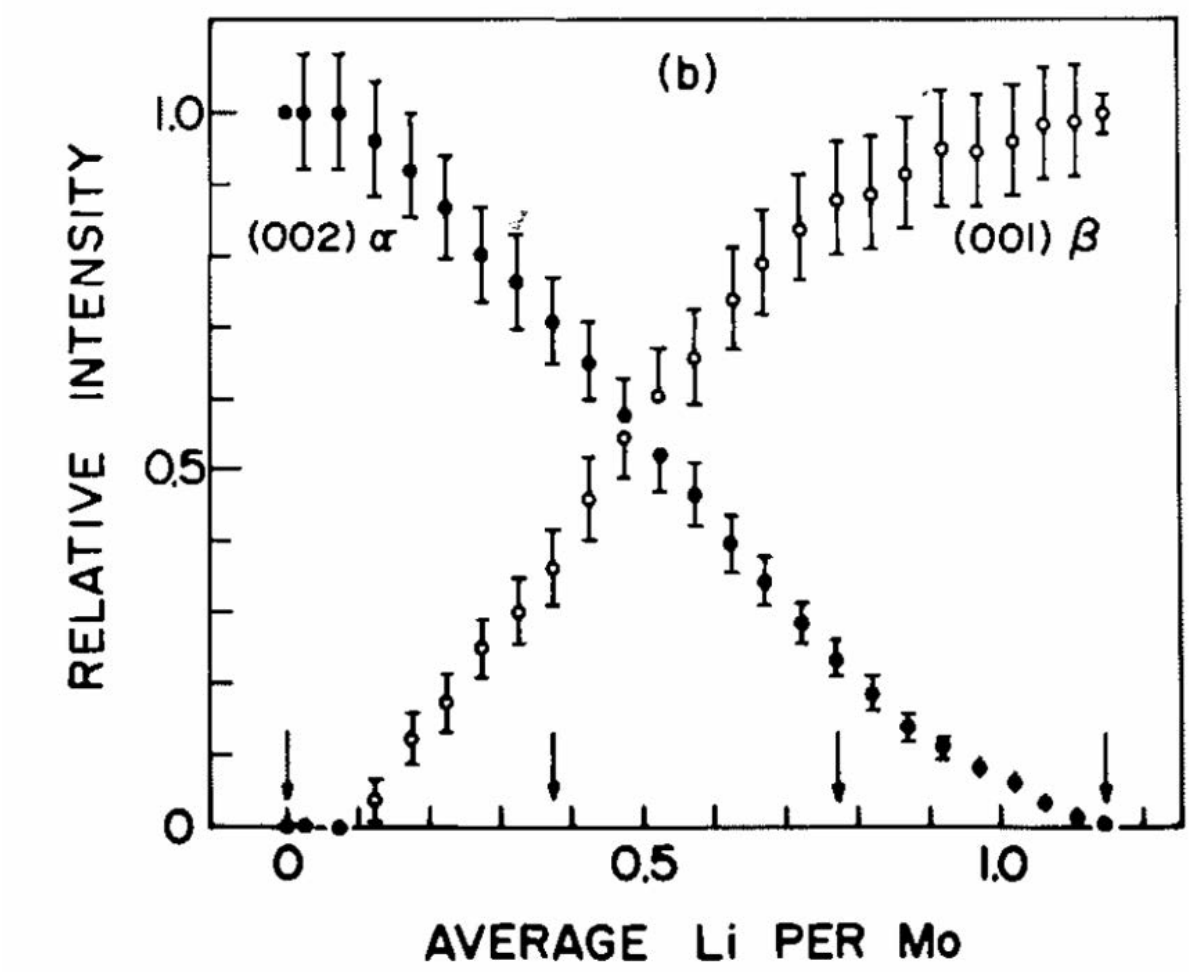

Figure 2.9: In-situ XRD during Li intercalation, showing transition from (002) peak [2H-MoS_2] to (001) peak [1T-MoS_2]. Adapted from [100]

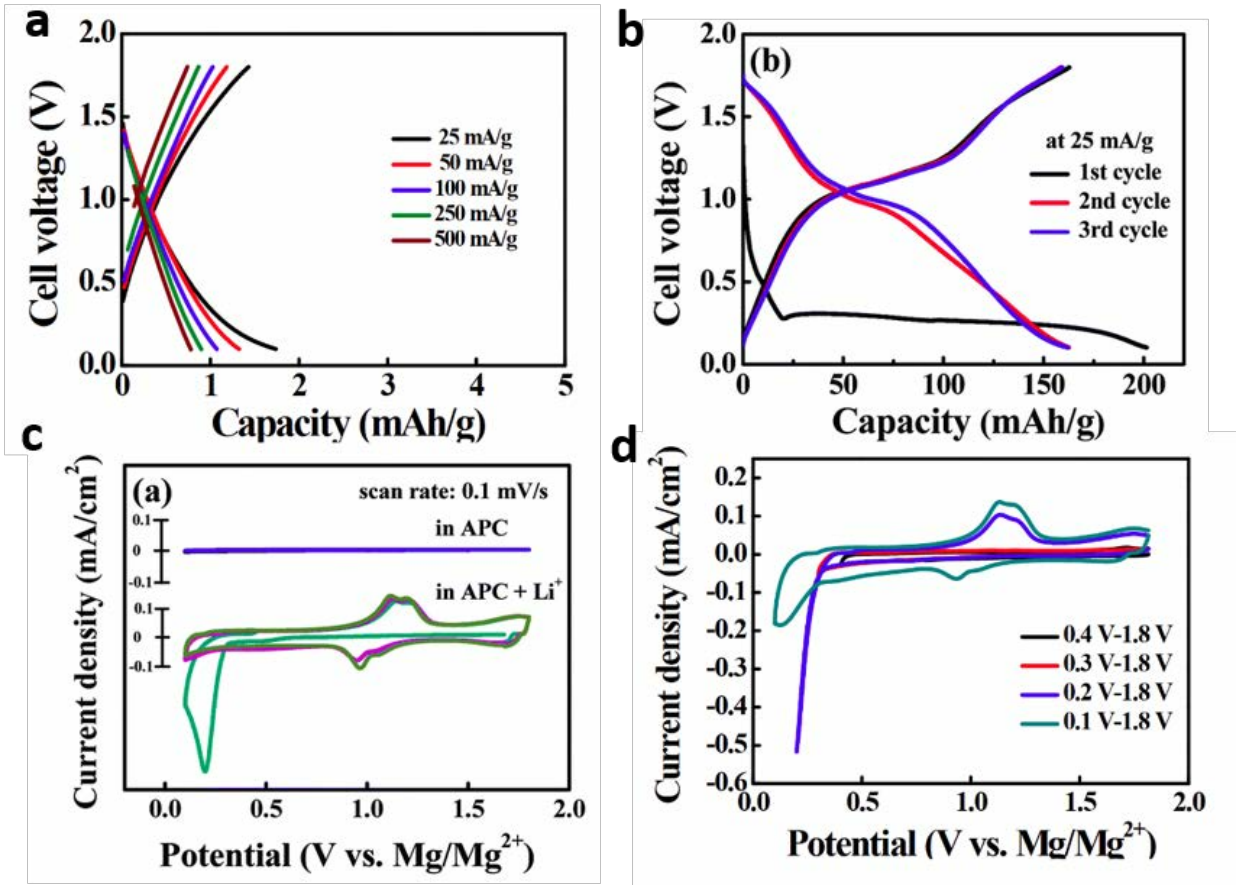

Figure 2.10: (a) Mg battery with 2H-MoS_2 cathode and Mg-only electrolyte (b) First 3 cycles of a Mg/2H-MoS_2 battery, with LiCl (c) CV scan of Mg/MoS_2 battery, with and without Li^+ in electrolyte (d) Mg/MoS_2 battery with LiCl, cycled down to different voltages. Adapted from [98]

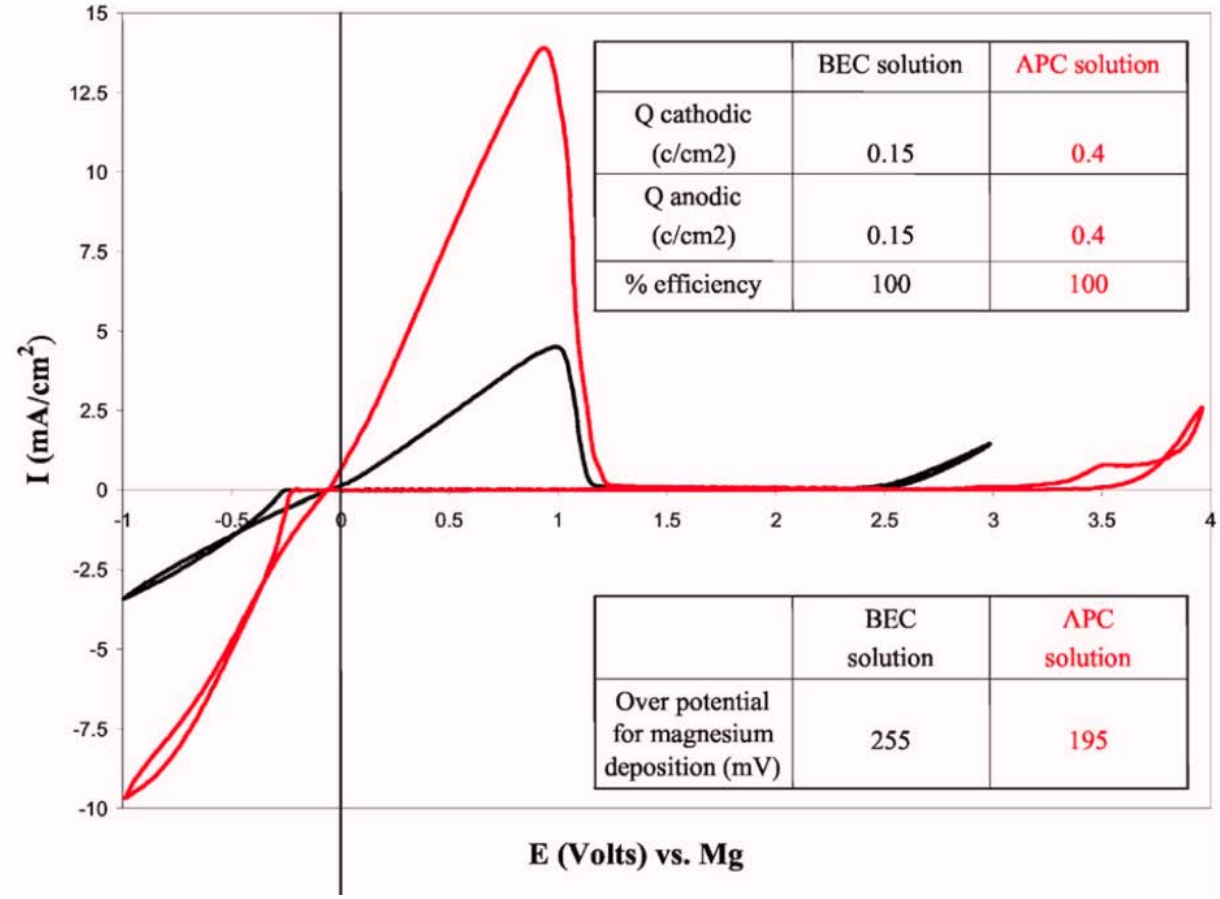

Figure 2.11: Cyclic voltammetry of APC electrolyte (red), showing low overpotential and high coulombic efficiency. Adapted from [101]

studies [91, 103, 104]. The coulombic efficiency, or reversibility, or Mg plating/stripping in APC has consistently been measured around 100%, indicating that side reactions or degradation products are negligible in the APC electrolyte (see Fig 2.11).

For each of these reasons, APC is the most common Mg electrolyte in current Mg battery research, and was selected as the electrolyte for the Mg slurry in this work.

2.5 Cathodic slurry

Like standard thin film electrodes, semi-solid electrodes need an active material, conductive material, and electrolyte. The active and conductive material are dispersed within the electrolyte to form a suspended particle network, which is then used as an electrode in

a battery cell. For this work, the material selection is outlined above (anode=Mg, electrolyte=APC+LiCl, cathode=MoS_2). To form a slurry electrode, the primary design considerations are the mass loading of the active and conductive materials and the electrode thickness.

Mass loading

Active material

The active material provides sites for redox reactions, and the theoretical capacity of the slurry electrode is set by the mass/volume of active material in the slurry. The mass loading in a semi solid/slurry system is commonly reported in volume percentage (vol%), as the spatial extent of each material in a given volume is critical to the amount of particle-to-particle contact.

The capacity and energy density of the battery can be increased with an increase in active material volume percentage, as increasing the vol% of active material provides more sites for redox reactions. Increasing the volume percentage also increases the viscosity of the slurry, by increasing the amount of solid material suspended within the electrolyte. A higher viscosity is expected to increase the energy required for pumping, which detracts from the round trip efficiency as is a form of loss in semi-solid batteries [13].

To deliver capacity, an active particle needs to be dispersed into a conductive particle network. This connection into the conductive particle network is referred to as an active particle being "electrically wired" into the network. An active particle which is electrically wired into the network can be accessed by electrons traveling through the conductive particle network, and can host redox reactions. Madec et al. studied the effect of varying the active material loading, from 15-25 vol%, and observed that at higher vol%, not all active particles were electrically wired into the network, leading to lower utilization and lower capacity (see Fig 2.12) [48]. Their work showed that a balance between active and conductive particles needs to be achieved to maximize capacity, and that the conductive particle vol% may need to be reoptimized as the active material vol% varies. For this work, we chose 10, 25 vol% as the active particle loadings to study, as they cover the range of values explored throughout the Li slurry literature.

Conductive material

The conductive additive is included in a semi-solid electrode to create conductive pathways for extracting/injecting electrons. Dispersed carbon particles form a suspended network, which electrically connects the current collector and active particles. As noted previously, the percolation threshold is the minimum amount of carbon additive required for non-negligible conductivity. The percolation threshold represents the lower bound on the amount of carbon additive required in our system. Increasing the volume percentage of conductive additive above the percolation threshold can be expected to further increase conductivity, reducing

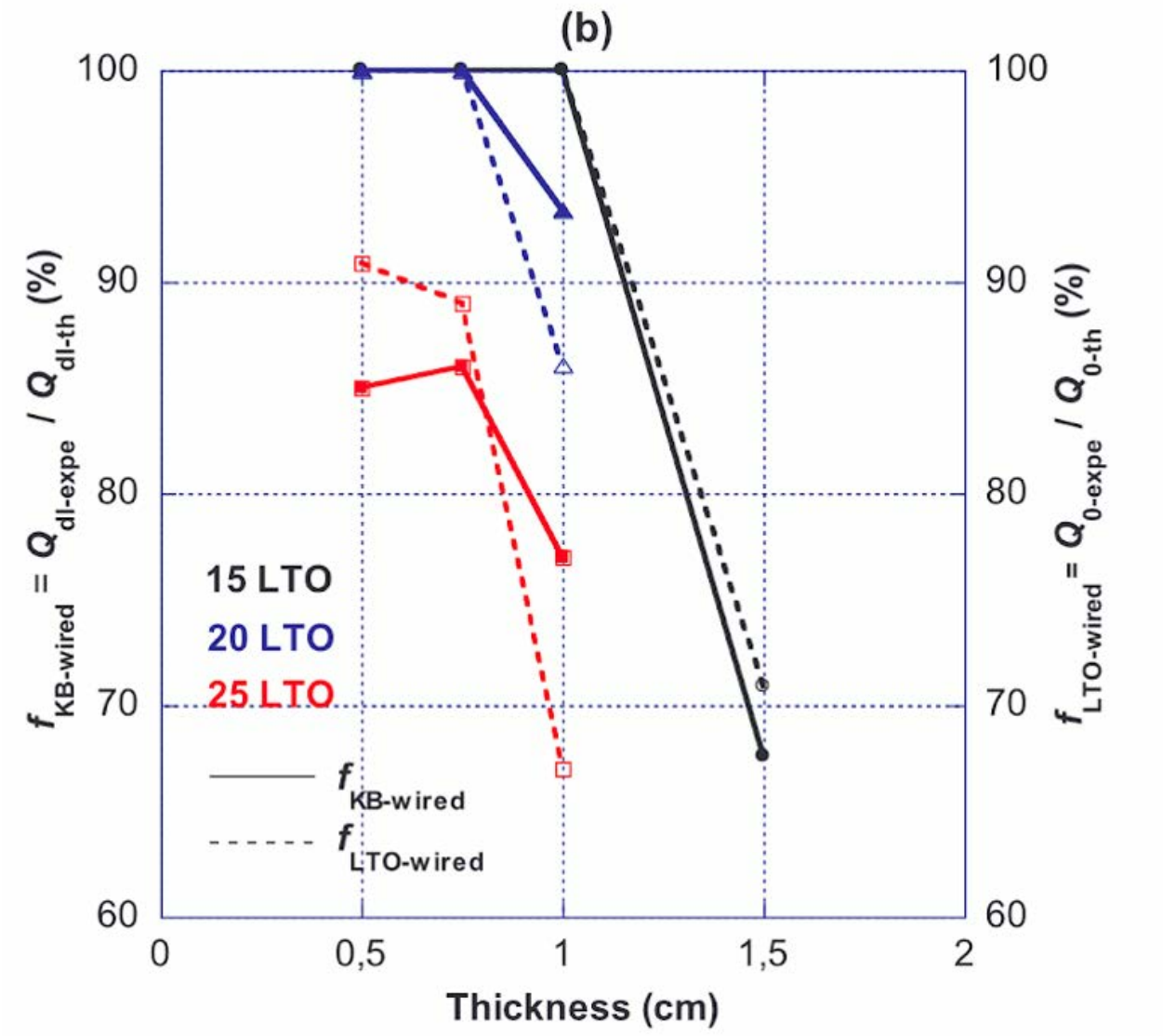

Figure 2.12: Percentage of the LTO and KB particles electrically wired into the network, as a function of electrode thickness. Adapted from [48]

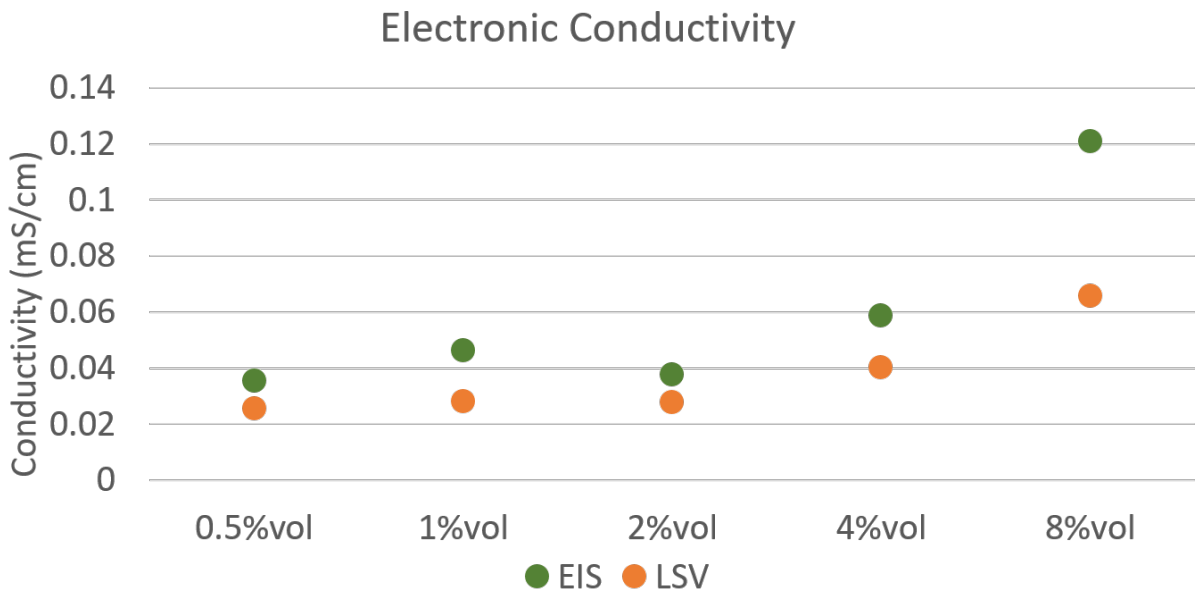

Figure 2.13: Electronic conductivity of MoS_2/KB slurries with varying KB vol%

IR losses and improving rate capacity. Increasing the vol% of conductive additives can also substantially increase the viscosity of the slurry, increasing pumping losses and reducing round trip efficiency of the cell [13]. Literature on Li semi-solid systems typically report 1-3%vol KB [13, 47, 48].

To establish bounds for the KB vol% in our MoS_2/KB slurry, a series of slurries were prepared with varying KB vol% (detailed in Chap 3 Experimental section) and the electronic conductivity was measured (see Fig. 2.13). A sharp increase in conductivity observed at 8%vol, and was chosen as the starting point for further studies. Later experiments that included 16%vol KB produced a gel-like slurry after mixing, which was in contrast to the liquid-like 8%vol KB sample. A phase transition between 8-16%vol was expected to exist, and 8,16 vol% were chosen as the low-high values for conductive additive loading for the initial slurry studies.

Electrode thickness

The thickness of the slurry electrode (set by the channel geometry) has shown to be a critical variable in the performance of a slurry flow battery, as it determines the active layer thickness in a battery. The working path length in a battery is the shortest distance from a given active particle to the current collector, as this is the length a conductive path must span to transport electrons to/from active sites (see Fig 2.14). Therefore, a chain/network of conductive particles must exist from each active particle to the current collector in order

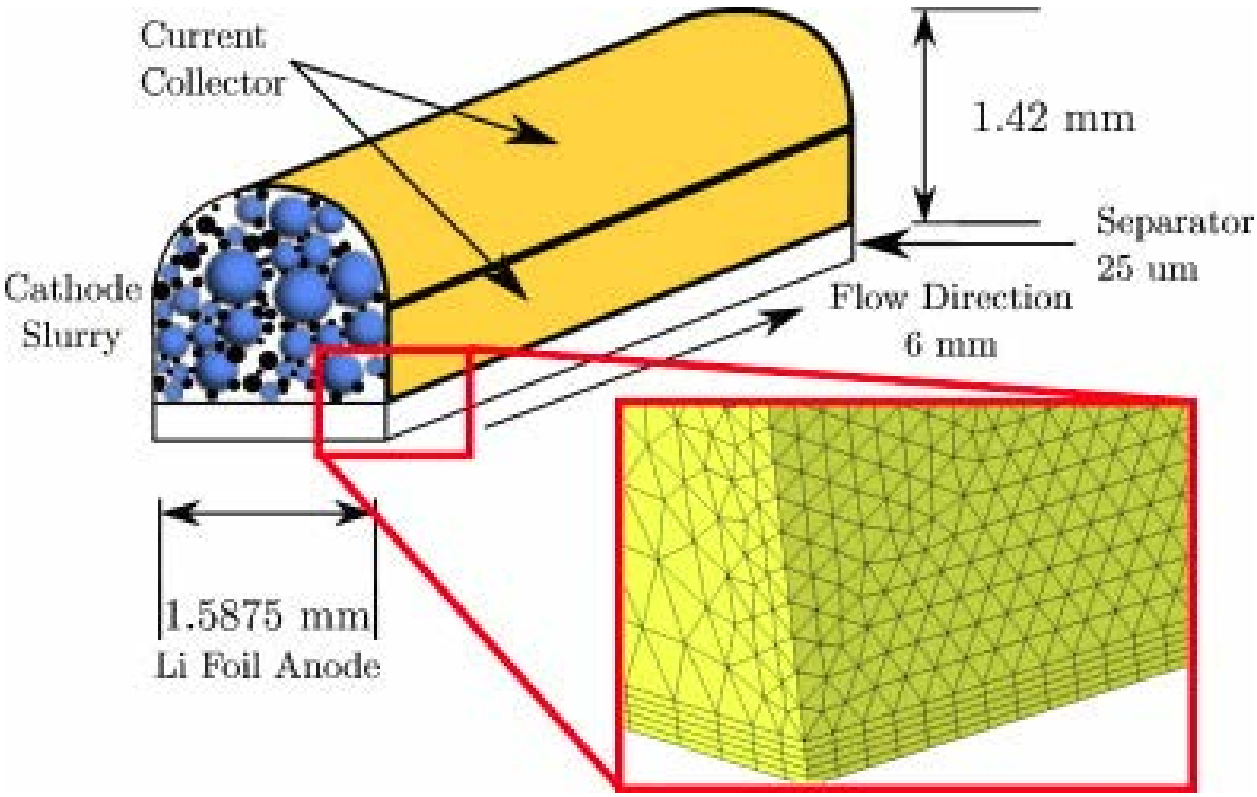

Figure 2.14: Cross-section illustration of flow channel, to illustrate how channel depth (1.42mm in image) affects slurry thickness in slurry flow battery. Adapted from [55]

to enable capacity from that active particle. As the path length that the conductive material must span increases, the probability of the conductive material being connected continuously over the full distance decreases. Incomplete conductive pathways therefore leave out active particles from the network, and reduce the capacity.

Figure 2.15 shows an LTO/KB slurry being cycled at various C-rates, but in Fig 2.15a the channel depth (active layer thickness) is 0.5mm, while in Fig 2.15b a channel depth of 1.0mm is used. At moderate and high discharge rates, a severe drop in capacity is observed at the larger 1.0mm channel diameter. The thinner 0.5mm diameter channel shows notably higher capacity in all cases, with the capacity at C/2 rate being 6x higher for 0.5mm compared with 1.0mm. This result was attributed to a carbon black network that incompletely connected active particles throughout the larger volume of the 1.0mm diameter channel, and highlights the difficulty of maintaining a continuous, suspended conductive network [48]. A 0.5mm active layer thickness was chosen for this work (further details in Section 2.8).

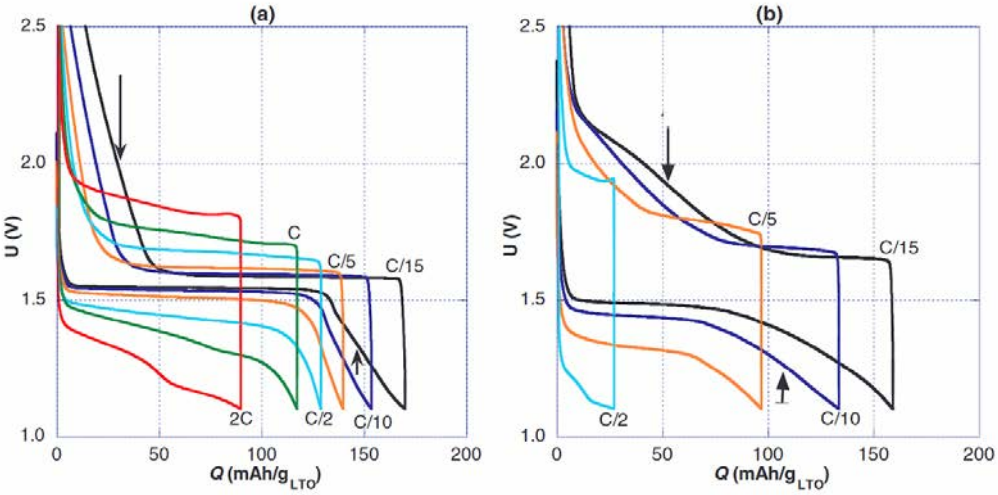

Figure 2. Typical galvanostatic charge/discharge curves of a 3 wt% KB/15 wt% LTO/82 wt% 1M LiTFSI-PC anolyte suspension (15LTO) obtained in static mode (no flow) as function of the charge/discharge rates for (a) 0.5 mm thick and (b) 1 mm thick.

Figure 2.15: Charge/discharge curves of an LTO semi-solid suspension at (a) 0.5mm and (b) 1.0mm slurry thickness. Adapted from [48]

2.6 Current collector

In a slurry battery system, the current collector has the following criteria:

High electronic conductivity: The current collector's primary responsibility is to conduct electrons from the external circuit to the electrodes. Carbon or metal are commonly used for current collectors for their high conductivity.

Stable in electrolyte: Current collectors can degrade or corrode at high voltages in some electrolytes. It is critical that the current collector is stable within the ESW of the electrolyte, to avoid degradation products and side reactions from affecting the electrochemical performance of the cell during cycling.

Low cost: Current collector stability is essential, however the materials with the highest stability (i.e. the largest barrier to reduction/oxidation) are typically noble metals like gold or platinum. These materials are prohibitively costly for high-volume, low cost applications. Striking a balance between cost and stability is a core challenge for current collector selection.

To quantify the electrochemical stability window (ESW) of an electrolyte/current collector combination, a LSV or CV sweep is conducted in a 3 electrode setup. The working and reference electrodes in the 3 electrode setup are typically a metal foil of the working ion in the battery (in this case, Mg foil was used for the working and reference electrodes). Possible current collector materials are used for the counter electrode, and a voltage is imposed between the counter and working electrodes. Voltage is swept from low to high, until a sharp increase in current is observed. The current produced is attributed to the oxidation/reduction of ei-

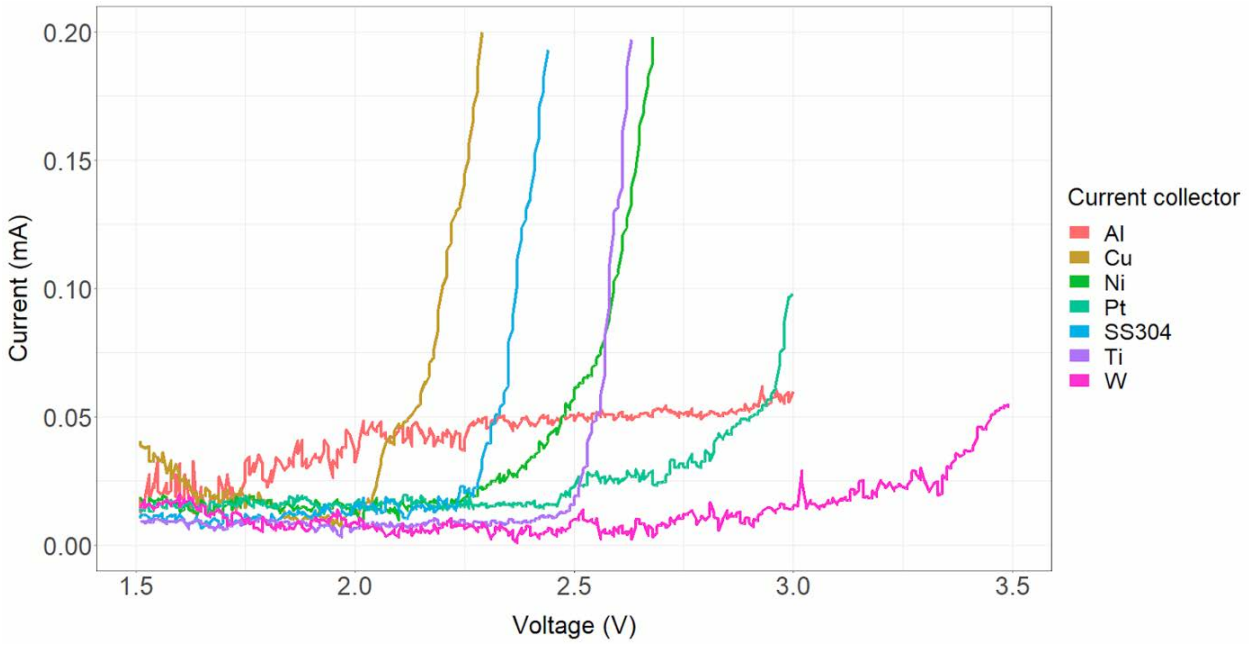

Figure 2.16: Electrochemical stability of current collectors in APC electrolyte, by CV measurement

ther the electrolyte or current collector, as there is no active material present within the cell. The voltage at which an inflection point in current is observed is considered the breakdown voltage, and marks the upper bound of the ESW for that electrolyte/counter electrode pair.

It is common to run a 3-electrode setup with platinum as the counter electrode first, as platinum is highly resistant to reduction and oxidation, and is considered inert. The breakdown voltage measured vs Pt represents the breakdown voltage of the electrolyte itself, and the ESW of the electrolyte/Pt becomes the standard to measure other current collectors against. If $\mathrm{ESW}_{\text{electrolyte/current collector}} < \mathrm{ESW}_{\text{electrolyte/Pt}}$, then the observed breakdown voltage is attributed to the current collector material.

In Fig. 2.16 below, several current collector materials, representing common battery current collectors in Mg and Li literature [105, 106], are evaluated via CV measurements. The breakdown voltage for each current collector is tabulated in Table 2.3. The ESW of APC/Pt in this study was 2.9V, and the open circuit voltage of Mg/MoS_2 is 1.8V. The selected current collector therefore needs to have an ESW in APC of just 1.8V, as that will be the highest voltage used during cycling. As the inflection point methodology for breakdown voltage has some subjectivity, a target of 2.0V ESW was selected to provide a margin for error. From Table 2.3, stainless steel 304 (SS304) was selected, as it offers the highest voltage stability (2.25V) of the low cost materials (Al, Cu, SS304).

Current collector	ESW (V)
Al	2.0
Cu	2.1
Ni	2.25
SS304	2.25
Ti	2.5
Pt	2.9
W	3.3

Table 2.3: Electrochemical stability window of current collectors in APC electrolyte

2.7 Separator

The purpose of a separator (also known as a membrane) in a battery is to conduct ions between the half cell reactions, but prevent electron transfer. In a slurry flow battery, the electronic conductors are the conductive and active material. The active material (MoS_2) is micron-scale in diameter, and the Ketjenblack EC-600JD powder is approximately 40nm in diameter [107]. In other flow battery technologies, where active compounds are dissolved and are $\leq$1nm in size, ion-selective membranes are required because sub-nanometer membranes are not yet available. In this work, size-selection membranes can prevent material crossover, provided that their pore size is smaller than the smallest charge carrier- for this design, 40nm.

Intercalation compounds in coin/cylindrical cells commonly use size-selection membranes, with Celgard membranes being the most widely used. Celgard manufactures a variety of membranes, which are polymer films (typically polypropylene and/or polyethylene) which are 12-38μm thick with controlled pore sizes ranging between 26-64nm [108]. Celgard membranes have been shown extensively with Mg-MoS_2 coin cells, providing evidence of strong material compatibility [95, 109, 110]. For this cell design, Celgard 2325 (see Fig 2.17) was selected for having sufficiently small pore size (28nm) and for its trilayer design (polypropylene-polyethylene-polypropylene) to prevent material crossover [108].

2.8 Cell hardware

To fabricate slurry cells, existing hardware could not be used, and therefore new hardware had to be designed. Electrodes need to be fabricated with well-defined dimensions, to control surface area, thickness, and mass. They also need to withstand compression of the cell layers; pressure is applied during fabrication to ensure strong layer-to-layer contact between the anode, separator, and cathode, and springs are common in cell designs to maintain pressure during cycling. In coin/cylindrical cells, freestanding thin film electrodes and/or metal foils are cut to well-defined geometric specifications, and can withstand compression

Product	2340	2325	C500	C480	2320	C300	C250	C200	C212	M825	M824
Thickness; µm	38	25	25	21.5	20	20	18	17	16	16	12
JIS Gurley; seconds	780	620	515	320	530	560	500	450	435	460	425
Porosity	45%	39%	35%	50%	39%	36%	35%	35%	35%	39%	38%
PP Pore Size; µm	0.035	0.028	0.041	0.038	0.027	0.032	0.032	0.032	0.032	0.026	0.026
TD Shrinkage @ 90° C / 1 hour	0.0%	0.0%	0.0%	0.0%	0.0%	0.0%	0.0%	0.0%	0.0%	0.0%	0.0%
MD Shrinkage @ 90° C / 1 hour	<7.0%	<5.0%	<5.0%	<5.0%	<5.0%	<4.0%	<5.0%	<5.0%	<2.5%	<1.0%	<1.5%
Puncture Strength; grams	>550	>380	>320	>400	>360	>300	>300	>245	>220	>300	>225
TD Tensile Strength; kgf/cm^2	165	150	170	140	165	185	175	190	180	150	155
MD Tensile Strength; kgf/cm^2	1630	1700	1680	2195	2050	1800	1800	1900	2085	2100	2200

Figure 2.17: Product specifications for trilayer commercial Celgard separators. Adapted from [108]

during cell assembly and sealing. Slurry electrodes are flowable and not inherently restricted to a well-defined geometry, and can only withstand compression if placed in a solid container.

This section describes the cell hardware design used throughout this work. Two cell designs were created: a flow cell, and a non-flowing, or static cell. The static cell has a fixed volume of slurry, and does not have the ability to flow in the cathodic slurry, but would be a prototyping testbed that allows for the slurry parameters to be rapidly studied without the effects of flow. Figure 2.18 shows the existing slurry cell hardware designs available in literature, however few specifications were provided, and so designs had to be specified from scratch.

Static cell hardware design

The design criteria for the static cell were:

Defined electrochemical area/volume: The flowable slurry would need to be confined to a defined volume, to control the amount of slurry in each cell, and to prevent flowing/leaking of the slurry when the cell is compressed/moved during assembly and operation. The thickness of the container holding the slurry would define the cathode thickness, which is a critical variable in previous slurry battery works.

Airtight: Magnesium foils and the APC electrolyte are both sensitive to oxygen and moisture contamination, and would be prepared in a nitrogen glovebox, but cell testing would happen largely outside of the glovebox. The cell design needed to prevent air ingress during cycling, to prevent oxygen and moisture-related degradation of active materials.

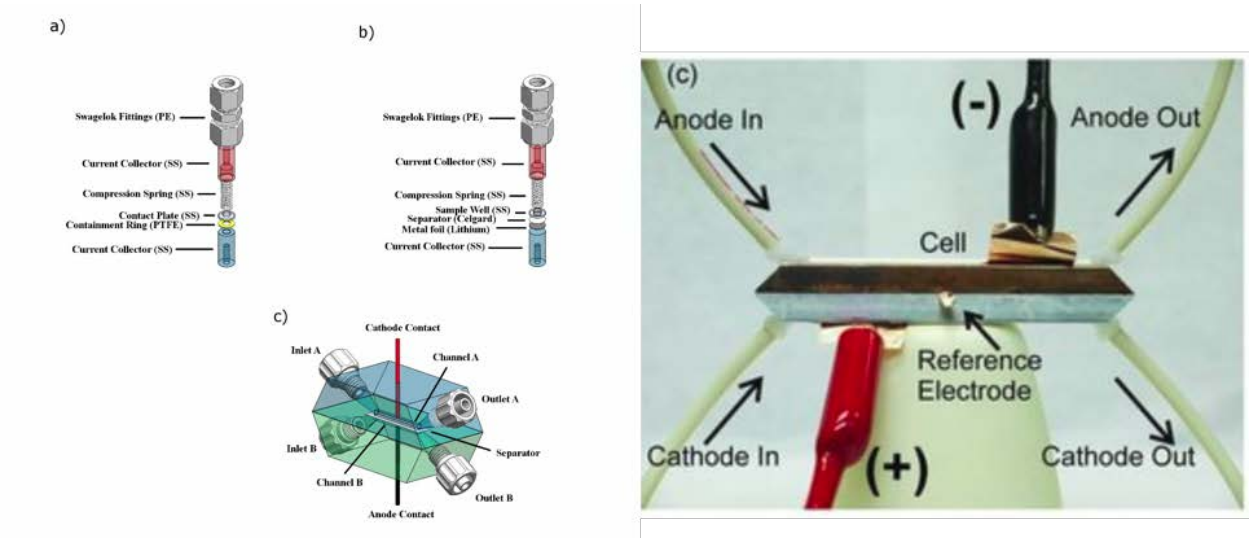

Figure 2.18: Semi-solid battery hardware in literature, from [47] (left: a) conduction b) static c) flow cells) and [13] (right: flow cell)

Reusable hardware for full cell, conductivity cell: A full cell setup, with Mg foil anode, separator, and cathode slurry, is the default configuration for the static cell hardware. A conductivity cell, which has insulating sidewalls and conducting end plates for LSV/EIS measurements, allows for conductivity measurements to be taken on the slurry, without any other films/materials present. The hardware selected for a full cell had to be adaptable to create a conductivity cell as well.

Solvent resistant (THF): The housing for the cell materials cannot degrade in the presence of the THF found in the electrolyte. THF is a highly volatile solvent which actively dissolves many common labware plastics [111].

Rapid assembly: Assembling large batches of cells quickly allows for rapidly exploring the parameter space for design of experiments. The flow cell hardware is more complicated, and having a rapid option for studying the non-flowing slurry was critical to success in this work.

Inexpensive, commercial hardware: To allow for other research groups to easily purchase and reproduce this cell hardware, components were purchased and used as-is or machined from inexpensive, commercially available hardware.

Swagelok hardware was chosen for the static cell, as it is already used in battery literature for 2 and 3 electrode setups in literature, is airtight, and easy to assemble. A two terminal Swagelok union (item #: PFA-820-6) was selected, and the housing material PFA (perfluoroalkoxy alkane) is known to be resistant to THF [111]. By inserting SS304 rods into either terminal of the union, electrical contact is made to both the anode and cathode sides of the cell.

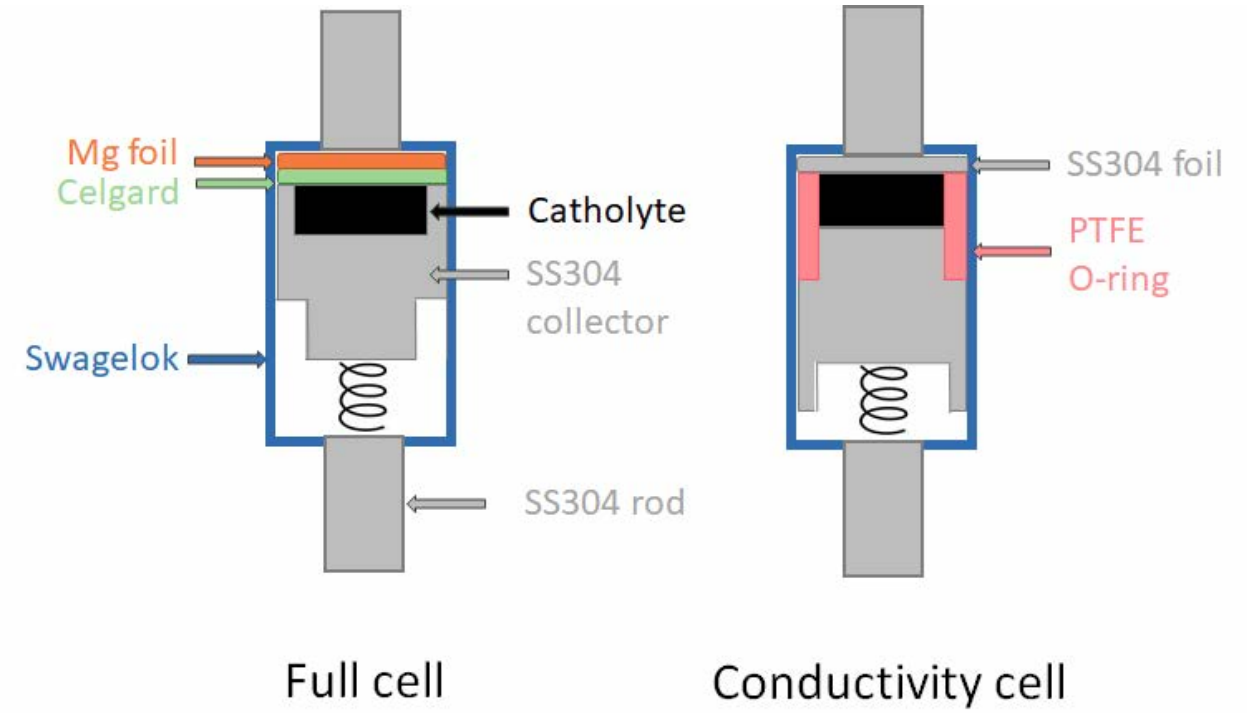

Figure 2.19: Schematic of static cell hardware variations used in this work

Swagelok hardware is popular within the battery community, as it is an easily sealable, airtight enclosure with a well-defined cavity in the center. Custom machined parts can be sized to fit within this cavity, for different electrochemical cell types. In the design for this work, a Mg foil and Celgard separator were inserted on one end of the Swagelok union, and held in place by a stainless steel rod (see Fig. 2.19). A custom metal part, designed in a cup shape to contain the cathodic slurry, was designed to fit within the cavity (see additional details below). Finally, a metal spring placed between the metal cup and SS304 rod provides compression when the cell is sealed, to ensure good contact is made between all of the parts within the Swagelok housing.

Machining a custom slurry container allowed off the shelf Swagelok hardware to be adapted for static slurry cells. To contain the slurry, an open-ended well of 0.5mm depth was machined into a cylindrical metal rod (Figure 2.20a). This design allows the slurry to be contacted by a separator on the open face of the metal container, while providing a base and sidewalls to contain the slurry so it cannot flow. This cup shape also allows the container to be put under compression as the pressure is applied to the walls of the metal cup and not the slurry. It allows strict definition of the depth and volume of the slurry, so that an exact amount of slurry is loaded into each cell, and the thickness of the slurry is set by the depth of the open-ended well.

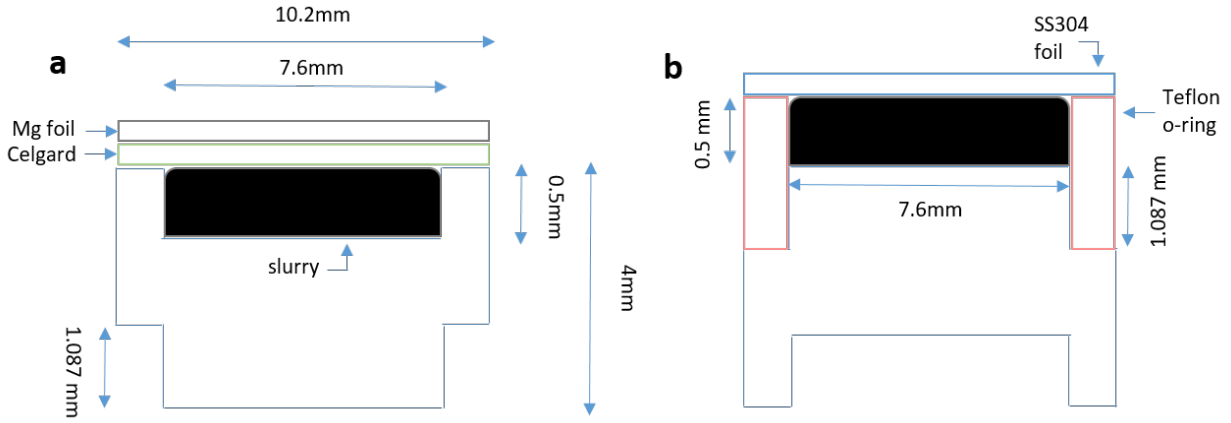

Figure 2.20: Schematic of metal slurry cup design, in the (a) full cell configuration (b) conductivity cell configuration

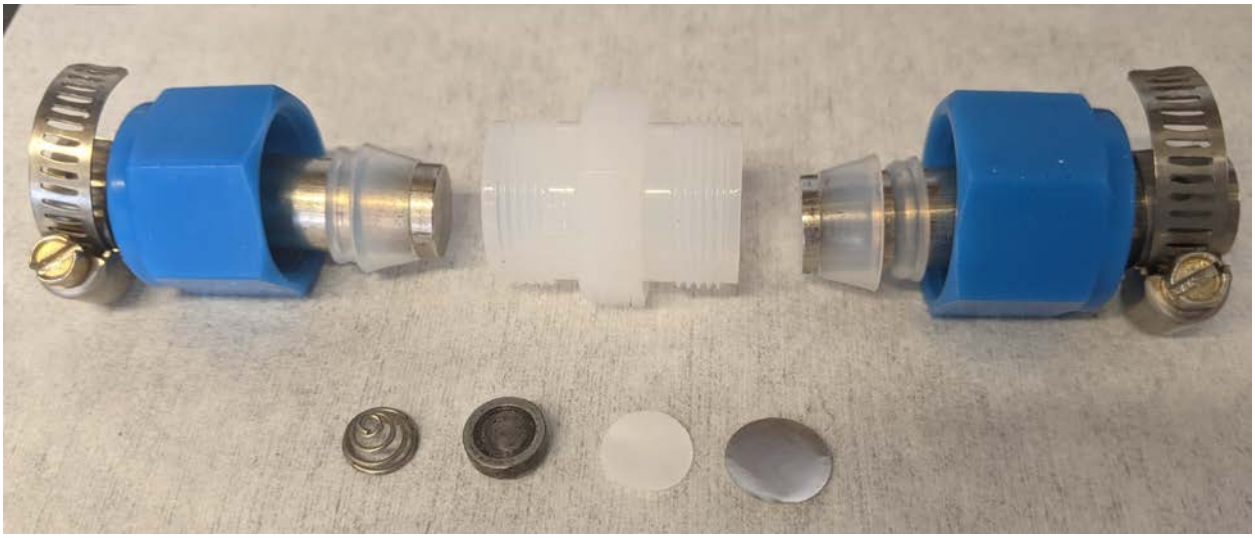

Figure 2.21: Picture of static cell hardware

To adapt this cell design for conductivity measurements, the same slurry container was inverted to establish a parallel plate configuration (see Fig 2.20b). Conductive surfaces on either end of an enclosed area, with insulating walls, allows for the conductivity of a battery material to be measured by applying a voltage across the conductive end plates and measuring current across the material enclosed within the volume. The existing open-ended cup side of the slurry holder has conductive sidewalls, and therefore is not suitable for conductivity measurements. The other end of the slurry cup was designed with a raised middle section with cut-out side walls. This geometry allows an insulating Teflon o-ring to be firmly attached around the middle section. As shown in Figure 2.20b, the o-ring thickness is chosen to be greater than the depth of the sidewall cutout, which results in the Teflon o-ring creating a cup-shaped well with a depth of 0.5mm , with Teflon (insulating) sidewalls and metal surfaces on either face. The slurry is loaded into this Teflon-walled well, and conductivity measurements can be conducted. A photograph of each piece of the static cell hardware is shown in Figure 2.21.

Flow battery hardware design

The flow cell hardware in this work had similar design constraints to the static cell, with the added constraint of having an inlet/outlet through which sorry could be pumped into/out of the cell. This cell hardware is meant to capture the effects of flow on the slurry during cycling, and to more closely mimic how the cell would be operated in a practical application. A syringe pump was used at the inlet, to provide precise volumes of slurry into the flow cell. Further details about the syringe pump setup can be found in the Experimental section of Chapter 3.

The flow cell, shown in Figure 2.22, shows an inlet and outlet, to which either a syringe or peristaltic pump can be connected, and a syringe filled with slurry is loaded into. The channel is machined out of a SS304 block, which is contacted perpendicularly to a current collecting metal rod. As with the static cell, metal and separator foils are cut/punched to the appropriate geometry, and the cell is fabricated by stacking the layers of the cell and holding them under pressure via threaded screws. The housing is machined out of a PTFE block, to provide solvent resistance from THF.

2.9 Summary

This chapter outlines the design decisions made to select the materials and hardware for this project. A magnesium anode was selected, for its lack of dendrites, low cost, and high abundance. A MoS_2 cathode was selected, for its low cost, high capacity, and commercial availability. The all-phenyl complex (APC) electrolyte provides high ionic conductivity and a wide electrochemical stability window. To enable MoS_2 to be used with a Mg anode, Li^+ were added to the APC electrolyte via the dissolution of LiCl salt. Li^+ intercalation transforms the phase of MoS_2 from 2H $\rightarrow$ 1T, and 1T-MoS_2 allows for both Li^+ and Mg^{2+}

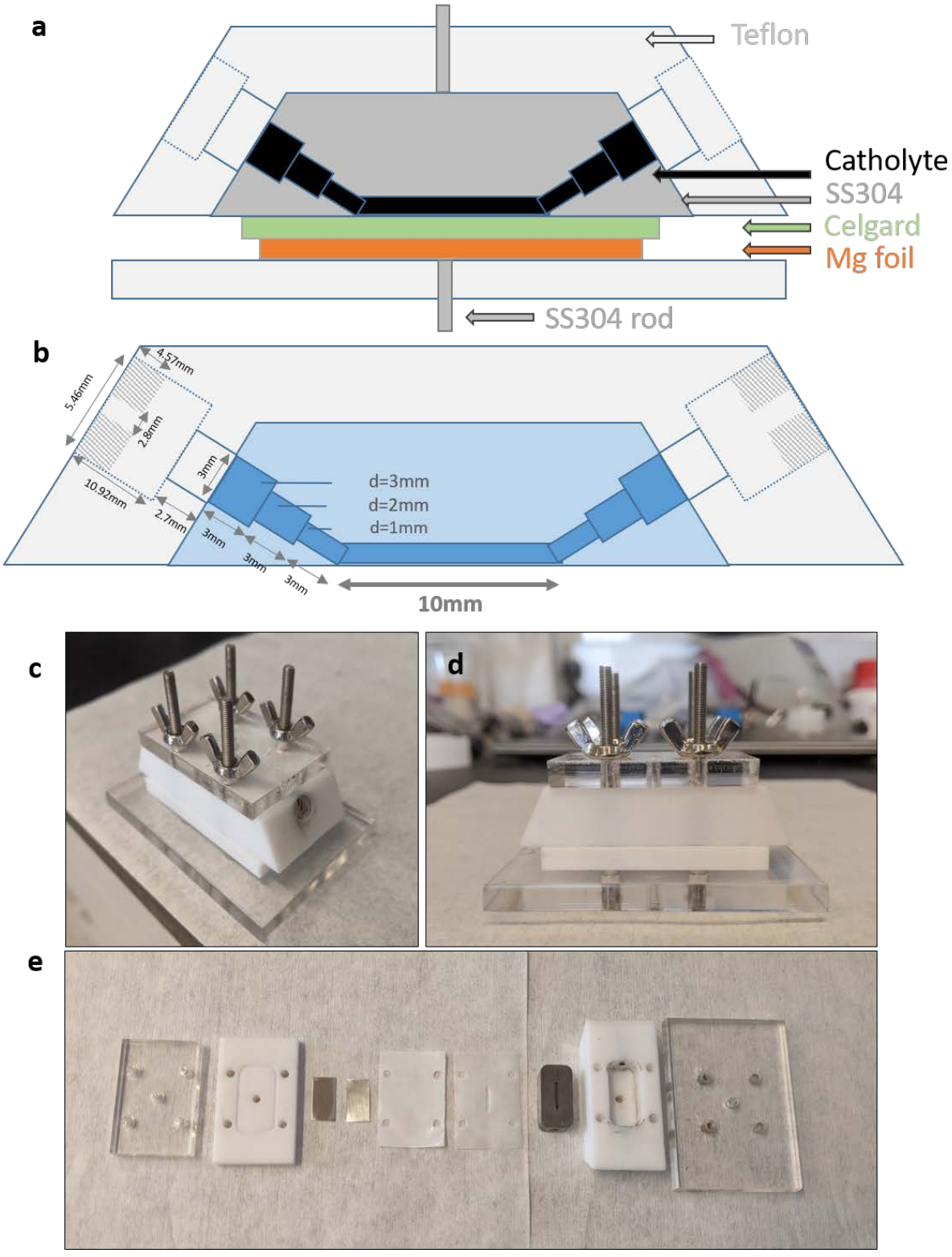

Figure 2.22: (a) Flow cell hardware configuration (b) Schematic showing dimensions of Teflon housing and slurry channel SS304 block (c) Front view of the flow cell (d) side view c) component view. In order, from left to right: acylic endplate, Teflon baseplate, SS316 plate, Mg foil, Celgard, PTFE film, flow channel block, top Teflon housing, acrylic endplate

intercalation. Celgard 2325 separators were used as size-exclusion separators, due to their small pore size. Stainless steel 304 showed sufficient stability and low cost, and was selected as the current collector material. Custom cell hardware was designed and machined, to allow a flowable slurry to be contained and integrated into flowing and non-flowing cell hardware.

The next chapter presents the first experimental data from a magnesium-based slurry flow battery. It will present electrochemical, electrical, and rheological data collected on the initial formulations of a MoS_2/KB cathodic slurry. Experimental methods of how the slurries are prepared and the custom cell hardware is assembled is included. Characterization data from multiple slurry compositions will be presented and discussed, with cycling data used as the final metric to select the optimal slurry composition.

Chapter 3

Rheological and Electrochemical Characterization of Magnesium Slurries

In order to develop an understanding of a slurry's characteristics, a suite of measurements was applied to an initial set of slurries to understand their rheological, electrical, and electrochemical properties. The purpose of the measurements described in this chapter was to characterize these four slurry compositions for their potential use in a slurry battery. We have broken down the basic criteria for a slurry in an SSFB, as outlined by prior works: 1) a shear thinning particle network, 2) ionic and electronic conductivity, and 3) hosting redox reactions. The measurements in this chapter aim to evaluate each of these criteria, with the final section providing data on the full cell performance of each of the four studied slurries.

As outlined in Chapter 2, several volume loadings were selected for our initial studies. For the concentration of Ketjenblack (KB), 8%vol and 16%vol are used, and for molybdenum disulfide (MoS_2), 10%vol and 25%vol were used. Crossing these factors produced four slurries: 10%vol MoS_2 - 8%vol KB (10MoS_2-8KB), 10%vol MoS_2 - 16%vol KB (10MoS_2-16KB), 25%vol MoS_2 - 8%vol KB (25MoS_2-8KB), and 25%vol MoS_2 - 16%vol KB (25MoS_2-16KB). These four slurries were used throughout this chapter, with an APC concentration of 0.8M and a LiCl concentration of 0.5M in the APC electrolyte.

3.1 Experimental methods

Materials

Aluminum chloride ($AlCl_3$, 99.999%), phenylmagnesium chloride (PMC, 2M in THF), anhydrous tetrahydrofuran (THF), 3Å molecular sieves (4-8 mesh), Whatman filters, and lithium chloride (LiCl, 99.98%) were purchased from Sigma Aldrich. Magnesium foil (100 µm) and Celgard 2325 were purchased from MTI. Molybdenum disulfide (MoS_2, 6 µm) was purchased from US Nanomaterials. Ketjenblack EC-600JD (KB) was donated by Akzonobel.

MoS_2, KB, and LiCl powders were dried at 150C under vacuum for 18hrs before each use. All other materials were used as received. All materials were opened and stored in a N_2 glovebox (MBraun, <1ppm O_2, 1ppm H_2O).

Electrolyte synthesis

All processes were carried out at room temperature in a N_2 glovebox. All materials were stored in glass vials with Teflon lined-caps in the glovebox. Powders were handled with a stainless steel scoop, and solutions were handled with a 10mL glass barrel syringe with Teflon-coated plunger.

To dry the THF, 3Å molecular sieves were activated under vacuum in an oven for 18hrs in an uncapped 500mL glass Nalgene bottle. Sieves were transferred into the glovebox immediately after removal from the vacuum oven, and cooled to room temperature before use. THF was poured over sieves in a glass bottle (1:1 vol ratio of THF:sieves), and left for 24hrs. Dried THF was then filtered through Whatman filter paper into a glass vial. To prepare the electrolyte, 800mg $AlCl_3$ was added to 9mL of dried THF under 1500rpm stirring with 1/2" Teflon-coated stir bar. The addition of $AlCl_3$ produces white smoke if added quickly, $AlCl_3$ was slowly added over a 15min period to minimize smoke formation. The $AlCl_3$/THF mixture was then added to 6mL of PMC, over a period of 2 mins. The solution was left overnight to stir at 1500rpm. After stirring, LiCl was added with a polypropylene scoop to the APC while under stirring at 1500rpm. The APC+LiCl was left for 6hrs (0.5M LiCl) or overnight (1M LiCl), until fully dissolved. Unless otherwise noted, a 0.8M APC+0.5M LiCl concentration was used for the electrolyte.

Slurry preparation

KB + MoS_2 were handled with a polypropylene scoop, and measured into a 20mL glass vial. APC+LiCl was then added via glass syringe. The tap density of each powder was measured multiple times and averaged, and used for slurry vol% calculations. The tap densities of the slurry powders: MoS_2=0.735g/mL, KB=0.088g/mL. For an example of the slurry vol% calculations: 5mL of 10MoS_2-16KB slurry = 0.0705g KB, 0.3675g MoS_2, 3.7mL APC-LiCl. To disperse the slurry, a probe tip sonicator (Branson 2400) with 6mm tip was used at 20% power for 150sec, paused for 60sec, then sonicated at 20% power for an additional 150sec. The vial was moved continuosuly by hand during sonication to allow the probe tip to contact the entire volume of slurry. The slurry was then homogenized (AN Laboratory AD300S-P) at 75% power for 1 min. The batch size was 5mL of slurry. Fresh slurry was prepared for each batch of batteries, and used immediately after preparation.

Full cell assembly

All cell assembly steps were carried out in an N_2 glovebox. Magnesium foil was twice polished with 800 grit SiC sandpaper in a cross hatch pattern, then twice polished in the same manner with 3000 grit SiC sandpaper. Mg anodes were punched out of polished Mg foil with a 12mm steel hole punch (McMaster, 3418A12) using a metal hammer on an OXO plastic cutting board. Each punched foil was rinsed with THF and dried with a Tekwipe. Celgard

2325 was laser cut into 12.5mm circles for the separator. The Mg foil and Celgard separator were placed into one end of the 1/2" Swagelok PFA union housing (Swagelok, PFA-820-6) and a 1/2" diameter x 2" long SS304 rod (McMaster, 89535K15) and PFA ferrules/end cap were tightened down to make contact with the anode foil and seal the union on one side. The custom slurry cup was placed in a custom 3D-printed plastic holder (see Chapter 2 for diagrams). The flat end of a PTFE-coated spatula (Sigma, Z513334) was used to scoop the slurry out of its vial and into the slurry cup. The flat edge of the spatula was used to blade coat across the top of holder to remove excess slurry. The Swagelok union was inverted and screwed into the threaded end of the custom plastic holder. A stainless steel rod (diameter: 9mm, length: 75mm) was used to push the slurry cup out of the holder and insert it into the cathode side of the Swagelok union, so that the open face of the slurry cup containing the slurry contacted the Celgard 2325 foil. The insertion rod was removed, and a 0.36" x 0.125" compression conical spring (McMaster, 1692K11) was added to the backside of the slurry holder. The Swagelok union was sealed by tightening down an end cap with PFA ferrules on a SS304 rod. Hose clamps (McMaster, 5388K17) were attached to each SS304 end rod to allow easy connection via alligator clips. To clean the hardware after use, all Swagelok parts and slurry cups were wiped with THF-soaked cotton tip applicators, and then sonicated in THF. 3000 grit SiC sandpaper was used to further clean the slurry cups, which were sonicated afterwards with THF. Fig 3.1 graphically illustrates the assembly procedure for the static cell hardware.

Conductivity cell assembly

Conductivity cells were assembled similar to full cells, except a 12mm diameter SS304 disk replaced the Mg foil and Celgard 2325 separator, and the other end of the slurry cup was used. An o-ring (inner diameter: 7.6mm, outer diameter: 10.2mm) was laser cut out of 1/16" (1.56mm) thick PTFE sheet (McMaster, 8545K13) and was attached around the metal center of the slurry cup. Slurry was then added into the center well, per full cell instructions.

Cycling protocol

Cells were mounted vertically into a plastic holder, with the metal anode foil above the slurry cup (as oriented in Fig 3.1). All cells were oriented this way during testing. A Biologic BCS-805 with BT-Lab software was used for cycling. All cycling protocols began with a 15 min rest period at open circuit, followed by a discharge-then-charge pattern for subsequent cycles. A voltage range of 1.8-0.1V was used, with a 15min rest in between each cycle. Discharge rates are calculated per gram of MoS_2, based on the slurry cup volume of 22.7 µL. For example, 22.7 µL of 10MoS_2-16KB slurry has 1.67mg of MoS_2; a 25mA/g rate corresponds to 41.67 µA.

CV protocol

Voltage was scanned between 1.8V and 0.1V, at a scan speed of 0.1mV/sec.

LSV protocol

A Gamry Reference 600 was used to scan between 0-100mV in 1mV intervals while cur-

rent is measured. EChem Analyst software was used to fit the slope of the I-V curve between 10-90mV, providing a resistance value R_{slope}. sigma = (L/A) / R_{slope}, with a cell configuration factor (L/A) of 0.1069 was used to calculate electronic conductivity.

EIS protocol

A Gamry Reference 600 was used to run a 10mV amplitude (vs E_{oc}) potentiostatic EIS scan from 1MHz to 0.1Hz, starting with a 15min rest period. The circuit model fitting is discussed in Section 3.3.

Rheometer

Brookfield DV-III+ and DV3T cone-plate rheometers were used for viscosity measurements. Rheometers with different viscosity ranges and spindles were required due to the large range in viscosity of the four slurries. The following slurry/rheometer/spindle combinations were used: 10MoS_2-8KB/DV-III+/CP-40, 10MoS_2-16KB/DV3T/CP-40, 25MoS_2-8KB/DV-III+/CP-52, 25MoS_2-16KB/DV3T/CP-52. Slurries were measured in air, with air exposure limited to 30 sec while loading into the rheometer. The measurement protocol was to let the slurry rest in the rheometer chamber for 15mins once loaded, preshear at 100 1/sec for 1min, rest for 1min, then measure from high to low shear, from 50 1/sec to 5 1/sec at 5 1/sec intervals. Each shear rate was applied for 2mins, and data from the last 30sec was averaged and taken as the measurement value. Fitting to the Herschel-Bulkley model was done using Microsoft Excel's Solver add-in.

3.2 Evidence of shear thinning in Mg slurries

To have a slurry that can provide reversible capacity as a battery electrode, the active and conductive particles must be in contact to transport electrons for redox reactions. The rheology of the slurry can provide evidence that such a particle network exists. In suspension/slurry literature, shear thinning is often used to indicate if a particle network has formed [112, 113, 114, 115]. To observe shear thinning, a viscosity-shear rate plot is generated, by varying the shear on a suspension and measuring the viscosity at each shear rate. Shear thinning refers to a monotonic decrease in viscosity with increasing shear rate. The reduction in viscosity is attributed to breaking apart connections between particles and agglomerates, reducing agglomerate size, and resulting in a loosely bound particle network of small agglomerates [113, 54]. Fig 3.2 graphically illustrates the effect of shear on a network of agglomerated particles.

To look for shear thinning behavior, viscosity as a function of shear rate was measured for each slurry composition in a cone-spindle rheometer (further experimental details are found in Section 3.1). As shown in Fig. 3.3a, the magnitude of viscosity across the measured slurries shows a range from 100 to 30,000cP. The wide range in viscosity justifies the need to study and refine the volume loading in a slurry electrode, as the pumping losses and rheological behavior are highly dependent on the viscosity.

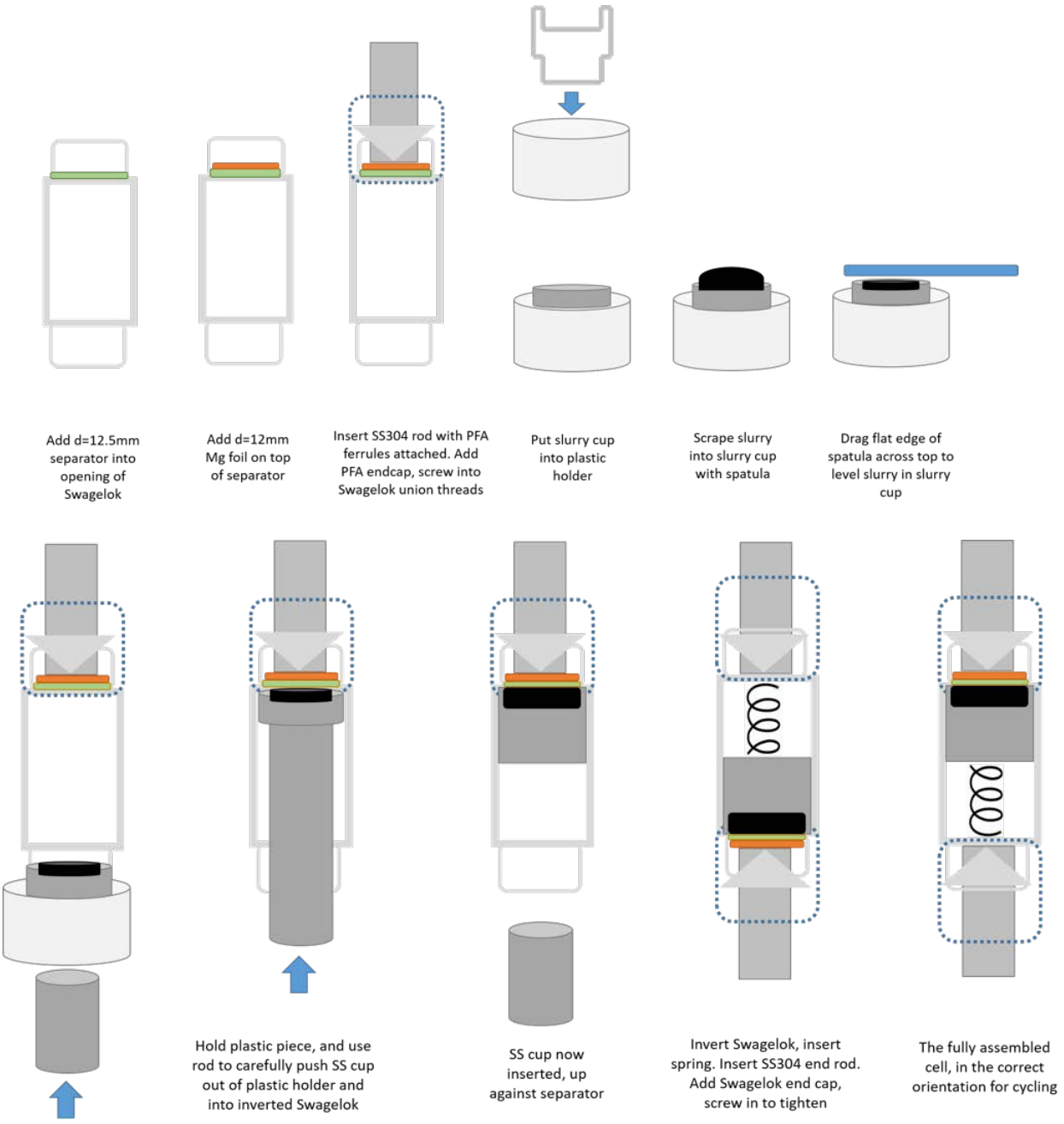

Figure 3.1: Fabrication steps for static cell hardware

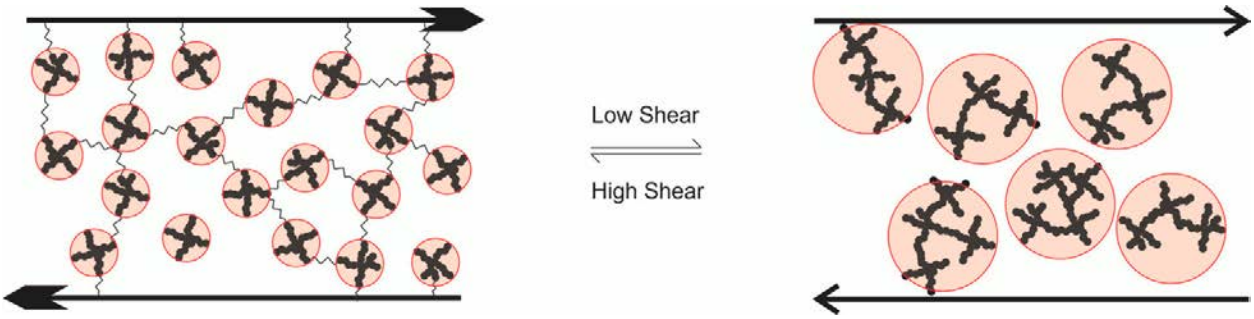

Figure 3.2: Illustration of agglomerate breakup due to high shear. Adapted from [113]

Slurry viscosity is strongly correlated to the number of particle-to-particle interactions within the slurry; increased volume loading within a slurry leads to increased contact between particles/chains of particles within the fluid, and the forces between particles increase the viscosity of the slurry. However, slurry viscosity did not increase monotonically as the mass loading increased in the four measured slurries for this work. For the four slurries presented we see the following total volume loadings: 10MoS_2-8KB = 18%vol, 10MoS_2-16KB = 26%vol, 25MoS_2-8KB = 33%vol, 25MoS_2-16KB= 41%vol. However, the viscosity increases in the following order by total vol%: $18 < 33 < 26 < 41$. The effect of KB on the viscosity is highlighted relative to the 10MoS_2-8KB slurry: adding 8%vol more KB (10MoS_2-16KB) results in a 14x increase in viscosity, while adding 15%vol more MoS_2 (25MoS_2-8KB) results in a 3x increase. The vol% of KB is therefore critically linked to viscosity, and efforts to reduce viscosity to reduce pumping losses should primarily focus on KB vol% reduction.

Fig 3.3a exhibits the presence of shear thinning is each of the 4 slurries, showing a decrease in viscosity with increasing shear. Fig 3.3b shows the normalized viscosity of each slurry, to more clearly display this trend. This plot highlights the similar slopes for each volume loading curve and suggests a similar degree of shear thinning for each slurry. Fig 3.3c plots the shear stress vs shear rate. The solid line shows the Herschel-Buckley model fit for each slurry, and the fitted flow indices confirm pseudoplastic behavior for all slurries (n<1, see Table 3.1 for values). These data taken together show the presence of a non-Newtonian fluid with particle connectivity.

Slurry	Yield Stress (τ_0)	Consistency (k)	Flow Index (n)
10MoS_2-8KB	0.11	15.84	0.25
10MoS_2-16KB	0.00	249.18	0.25
25MoS_2-8KB	0.00	66.41	0.21
25MoS_2-16KB	0.00	1198.07	0.32

Table 3.1: Parameters for Hershel-Bulkley Model Fitting in Fig 3.3c

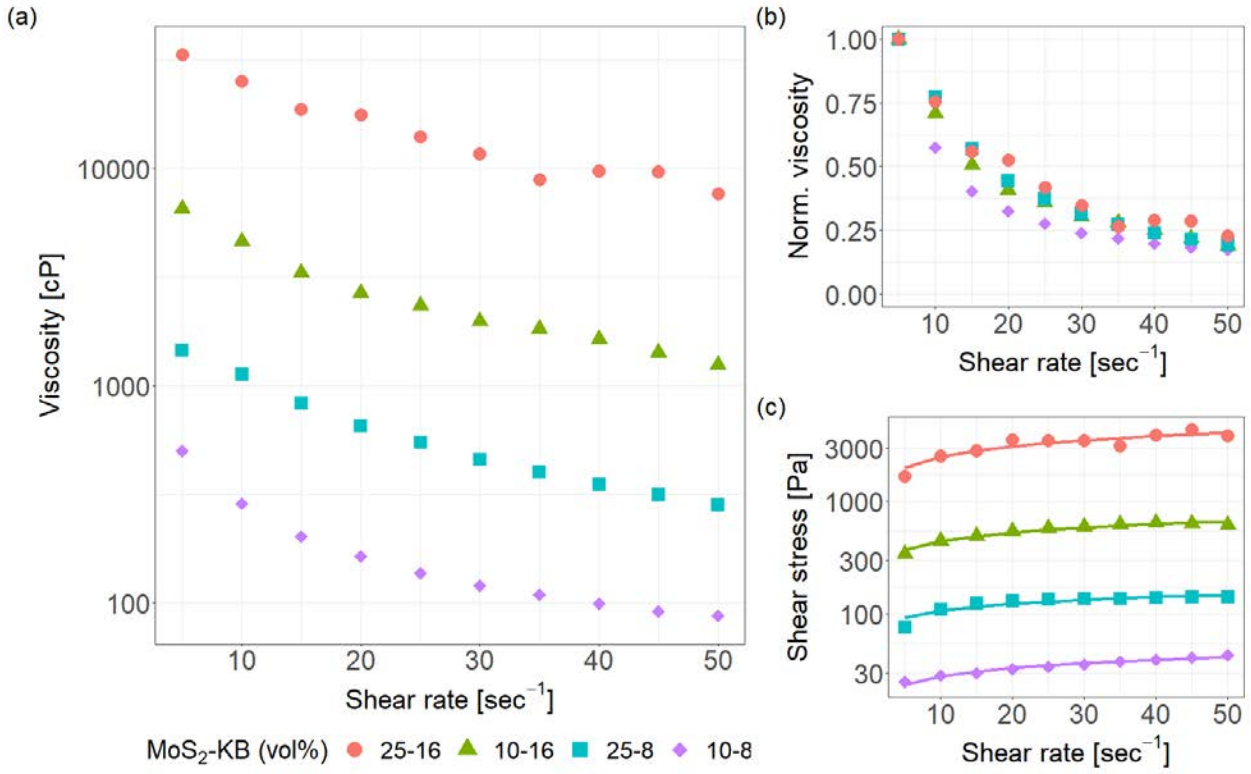

Figure 3.3: (a) Viscosity-shear (b) Normalized viscosity-shear rate (c) Shear stress-shear rate plot for four studied slurries

3.3 Electronic and ionic conductivity in MoS_2/KB particle network

A slurry electrode in a semi-solid flow battery needs to conduct both ions and electrons, similar to a traditional battery electrode. Particle-to-particle contact is of interest to transport electrons to/from active particles within the slurry. Conductivity measurements are a direct way to evaluate the transport properties of a given slurry composition, and were used to quantify ionic and electronic transport in each of the explored slurry compositions.

Electronic conductivity

Two methods were used to evaluate conductivity, linear sweep voltammetry (LSV) and electrochemical impedance spectroscopy (EIS), both using the conductivity cell hardware (see Section 3.1 for further experimental details). LSV applies a voltage across two ion-blocking, electron-conducting electrodes, measures a current, and uses Ohms law (V=IR)

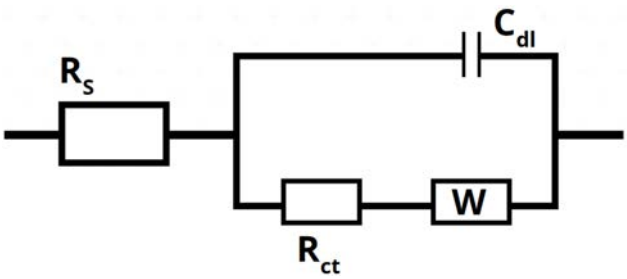

Figure 3.4: Circuit schematic of Randle cell

to calculate resistance. In our hardware, the SS304 rods can conduct electrons but not ions. Because of the ion-blocking electrodes, the current measured is solely attributed to the conduction of electrons. EIS measures impedance across two conductors, and then the raw data is fit to a circuit model to extract relevant parameters about resistance, capacitance, and inductance. The chosen circuit model often allows for separation between the ionic and electronic conductivity.

For this work, the EIS model of choice was the Randle cell. The Randle cell contains the following elements, depicted in Fig 3.4: solution resistance (R_s), double layer capacitance (C_{dl}), charge transfer resistance (R_{ct}), and ion diffusion modeled as a Warburg impedance (W). A similar version of this circuit model is used in several other semi-solid battery works [116, 67, 113]. In a Randle cell, the solution resistance and charge transfer resistance are separate elements, to allow the decoupling of various transport processes. A Warburg impedance element is included for modeling the diffusion of ions, and the double layer capacitance accounts for the effect of ions near the electrode double layer.

The data points in Fig 3.5a show the raw data from the EIS scans of each slurry, plotted as Nyquist plots. The semi-circle behavior seen in the data has two x-axis intercepts, each one corresponding to a different mechanism of charge transport. The low impedance x-axis intercept (the high frequency EIS measurements) represents the ionic resistance, and the high impedance intercept represents the electronic resistance. The intercepts are assigned to those charge transfer mechanisms because 1) the conductivity of the electrolyte is 3-4 mS/cm, matching closely to the values extracted from the low impedance intercept 2) the LSV results, representing the electronic conductivity, match reasonably well to values extracted from the high impedance intercept.

The solid lines in Fig 3.4a show the Randle cell fit to each of the slurry data. Randle cell model fits approximated the 10MoS_2-16KB and 25MoS_2-16KB data well, but significantly worse fits were obtained for the 10MoS_2-8KB and 25MoS_2-8KB slurries. Because of this poor fit, the electronic conductivity was instead taken from the LSV data. The LSV data collected on each slurry was analyzed by fitting the slope of the I-V curve under small bias (0-100mV), and calculating conductivity using the found resistance value. This data is plotted in black in Fig 3.6.

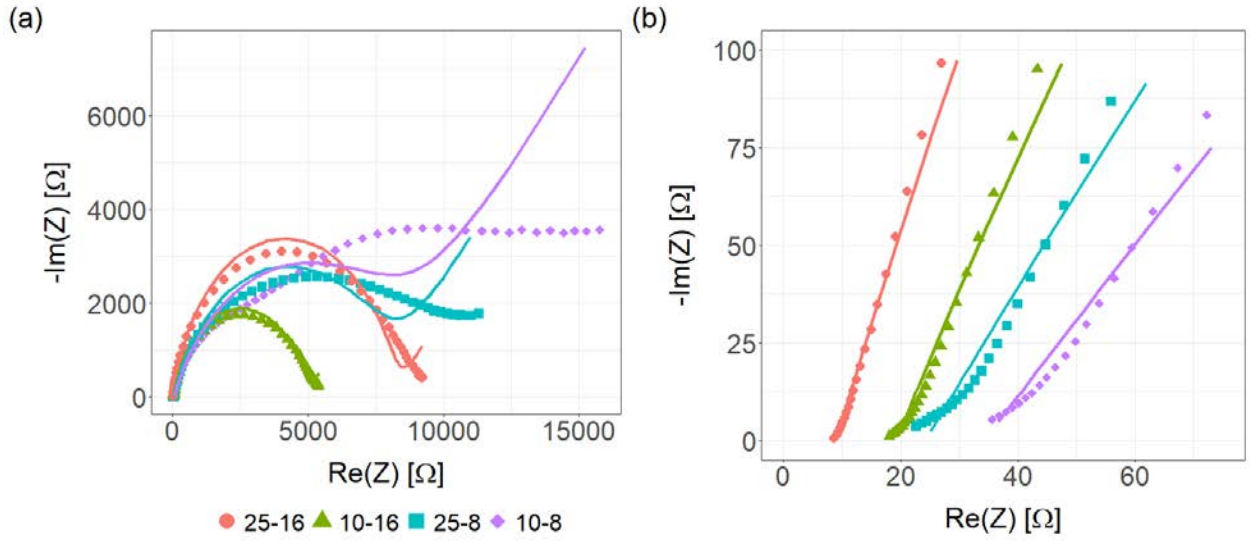

Figure 3.5: (a) Nyquist plots from raw EIS data, for all slurries (b) High frequency x-intercept showing ionic resistances

All four slurries were found to have non-negligible electronic conductivity, suggesting that each slurry had sufficient KB-chain connectivity to span the electrode thickness. The general trend seen is for higher electronic conductivity at higher volume loadings. This could be attributed to better particle-particle contact due to higher volume loading, particularly due to increased KB to create additional conductive paths and reinforce existing paths. The 10MoS2-16KB slurry is a notable outlier, which has higher conductivity than would be expected from the general trend.

Ionic conductivity

Ionic conductivity is primarily imparted onto the slurry via the electrolyte. As the electrolyte comprises the majority (between 59-82%vol) of the volume in our slurries, and the particles are fully immersed in the electrolyte, high ionic conductivity is expected for each slurry blend. As shown in Fig 3.5b, the low frequency intercept for EIS measurements is accurately modeled with the Randle cell, and therefore EIS data was used to extract ionic conductivity.

Fig 3.6 shows the ionic and electronic conductivity of the four studied slurries. Across all slurries, the ionic conductivity is 3 orders of magnitude higher. This discrepancy is similar to other literature reports on SSFBs, and why electron conduction is expected to be rate limiting in SSFBs [13]. It is not yet clear why ionic conductivity increases with higher volume loading of KB and MoS_2 particles. All slurries under study showed significant electronic and ionic conductivity, and did show a trend towards higher conductivity at higher volume loading.

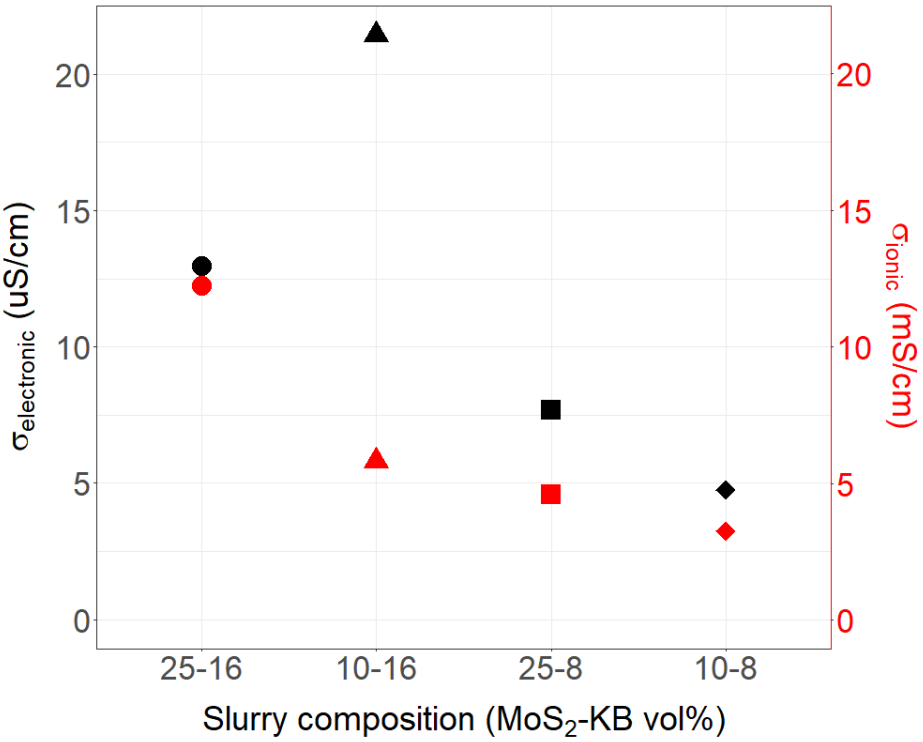

Figure 3.6: Ionic and electronic conductivity for each slurry composition

3.4 Redox activity in static Mg slurry batteries

While the rheology and conductivity measurements suggest the existence of a conductive particle network, the connectedness of the active MoS_2 particle into this particle network has not yet been verified. To quantify this behavior, cyclic voltammetry (CV) measurements were carried out. By sweeping voltage and measuring current, CV measurements capture the rate at which redox reactions are occurring across a range of voltage. Knowing that MoS_2 is the only redox active compound in the electrode, we can therefore quantify the utilization of MoS_2 in the slurry via CV measurements. Peaks in the current occurring at specific voltages can also help identify which redox reactions are occurring, and provide further insight about the mechanisms at work during cycling.

The full CV data is presented in Fig 3.7, including all 6 cycles of data for each slurry. The current shown on the y-axis has been normalized to the mass of MoS_2 in each slurry, to allow a direct comparison across different MoS_2 volume loadings. It is apparent that more electrochemical activity is happening in the two 16%vol KB slurries, as each 16%vol CV plot has several notable peaks where the 8%vol slurries have none. The plots in Figures 3.8 and 3.9 show certain aspects of the data in Fig 3.7, to highlight specific features.

Fig 3.8 shows the first two cycles of the CV scan, for each slurry composition. In order for

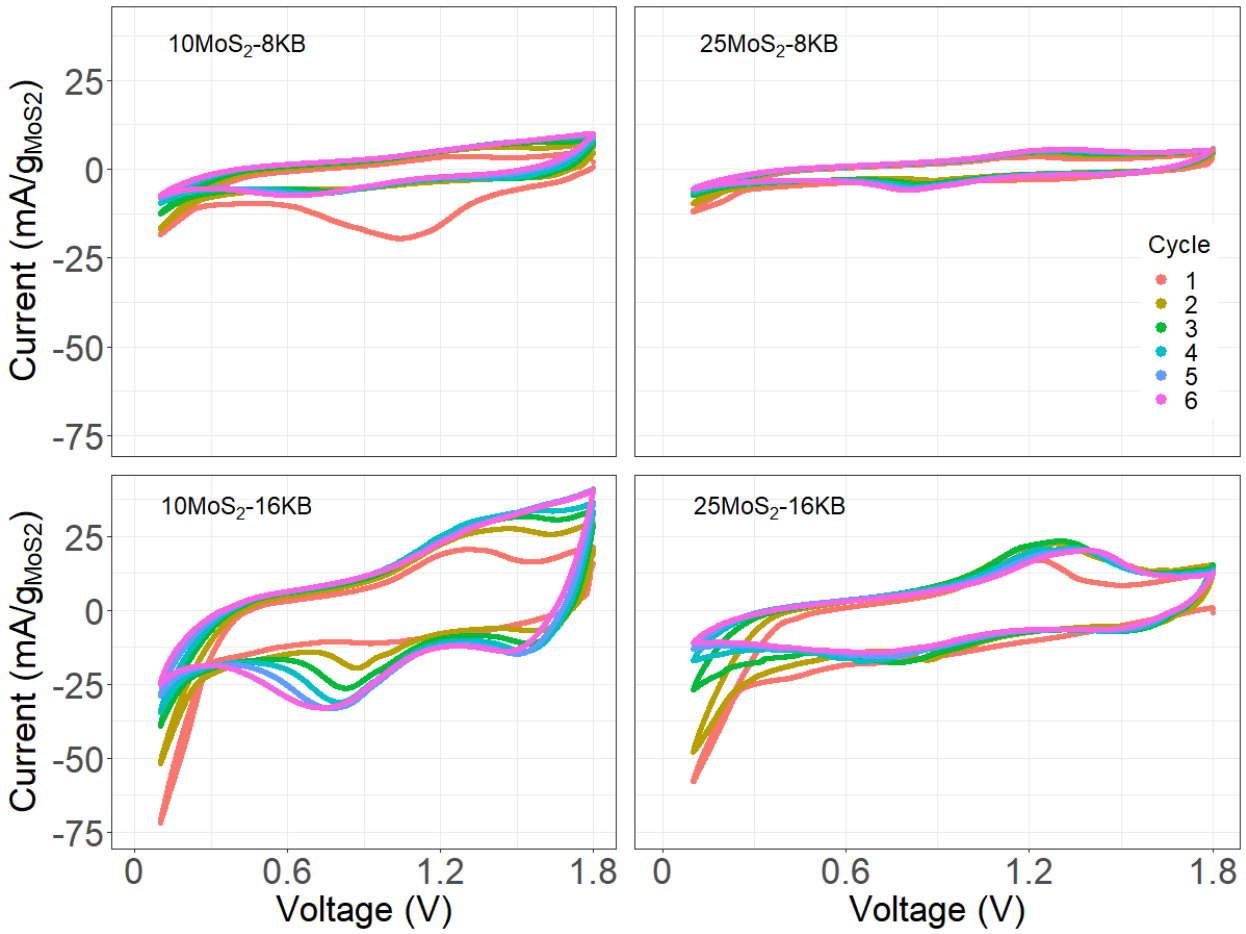

Figure 3.7: Cyclic voltammetry (CV) scans for each slurry, for 6 cycles

the MoS_2 particles to intercalate Mg^{2+} ions, the Li^+ ions need to intercalate into the MoS_2 particle in the first discharge cycle, and drive a phase transformation to convert from 2H-MoS_2 $\rightarrow$ 1T-MoS_2. From literature, it is known that Li^+ intercalates into MoS_2 around 0.2V vs Mg [98]. Each cell was cycled between 1.8-0.1V, to fully capture the Li^+ intercalation.

In the 16%vol KB slurries, there is a pronounced peak at 0.2V in the first discharge cycle (see Fig 3.8a), indicating that Li^+ intercalation is occurring in those slurries. This Li^+ intercalation peak is $\approx$3-5x smaller in the 8%vol KB slurries, suggesting that Li^+ intercalation is happening to a lesser extent in the 8%vol KB slurries. Upon sweeping from 0.1V to 1.8V in the first cycle (corresponding to the charging direction), a prominent peak exists at $\approx$1.2V in the 16%vol KB slurries, and in the second cycle a discharge peak at $\approx$0.9V is visible as well. These peaks are consistent with CV reports of APC-LiCl/MoS_2/KB in the literature [98]. This data indicates that both charging and discharging redox reactions are happening in the 16%vol KB slurries, and the absence of peaks suggests that redox reactions are happening at

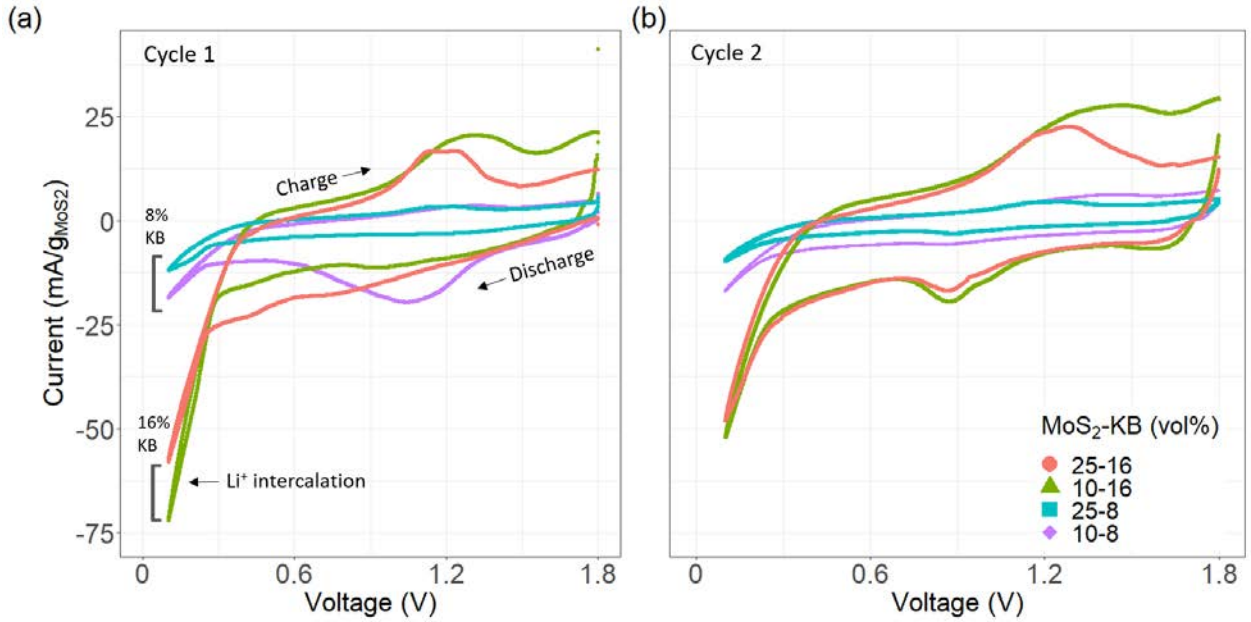

Figure 3.8: (a) 1st cycle (b) 2nd cycle of CV scans for each slurry

far fewer rates in the 8%vol KB slurries. Further work to elucidate if the charging/discharging reactions are driven by Li^+ or Mg^{2+} ions is presented in Chapter 4.

In prior work on Mg-MoS_2-LiCl systems, the Li^+ intercalation peak at 0.2V disappeared after 1 discharge cycle, suggesting that the 2H-MoS_2 $\rightarrow$ 1T-MoS_2 transformation was completed within the first cycle. In the slurry systems used in this work, the same effect is not observed; the Li^+ intercalation peak is present across 6 cycles (the full length of the measurement), but diminishes in magnitude each cycle. Fig 3.9 shows the value of the current at 0.1V for each slurry for each CV cycle. This plot suggests that the MoS_2 is not fully transformed to the 1T phase after the initial discharge cycle. This behavior should be noted for long term cycling studies, as a period of several cycles may be required before full MoS_2 conversion is achieved.

3.5 Reversible capacity in static cells for low and high concentration slurries

Ultimately, reversible capacity is the metric that determines the suitability of a slurry electrode in a full cell system. Full cells were fabricated using the same slurries discussed in this chapter. A 25 mA/g current was used to discharge and charge the cells for an initialization cycle, allowing Li^+ intercalation into the MoS_2, followed by 5 subsequent cycles. The voltage-capacity data in Fig 3.10a shows the 2nd cycle, occurring after the initialization

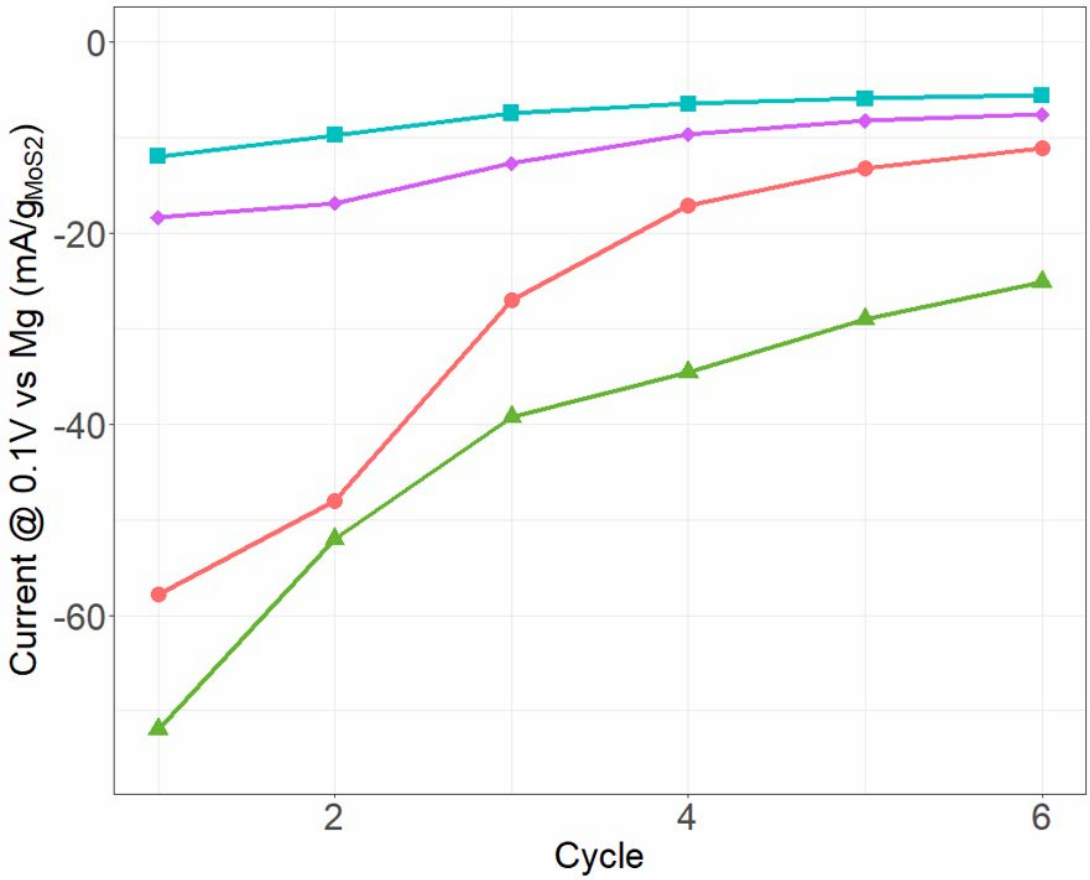

Figure 3.9: Current after full discharge (0.1V vs Mg) from CV measurements, representing the magnitude of the Li^+ intercalation peak

cycle was completed. The 16%vol KB slurries both showed non-negligible capacity, with capacities of 60 mAh/g and 165 mAh/g for the 25MoS_2-16KB and 10MoS_2-16KB slurries, respectively. The 8%vol KB slurries showed capacities of 12 mAh/g and 6 mAh/g for the 25MoS_2-8%KB and 10MoS_2-8%KB slurries, respectively. Fig 3.10b shows the initialization cycle (cycle 1) and the subsequent 5 cycles. Despite a capacity drop after the initialization cycle (attributed to some Li^+ trapped in the transformed MoS_2), the capacity of the 16%vol KB slurries remains high during cycling, while the 8%vol KB slurries is negligible after the initialization cycle.

The lack of capacity shown in the 10MoS_2-8KB and 25MoS_2-8KB slurries is consistent with their lack of redox activity present in their CV plots. It is expected that low amounts of Li^+ intercalation in the first cycle would inhibit capacity, as few MoS_2 sites have been transformed to the 1T phase and therefore intercalation for Mg ions is prevented in later cycles. Therefore, the 16%vol KB slurries with high Li^+ activity would be expected to show

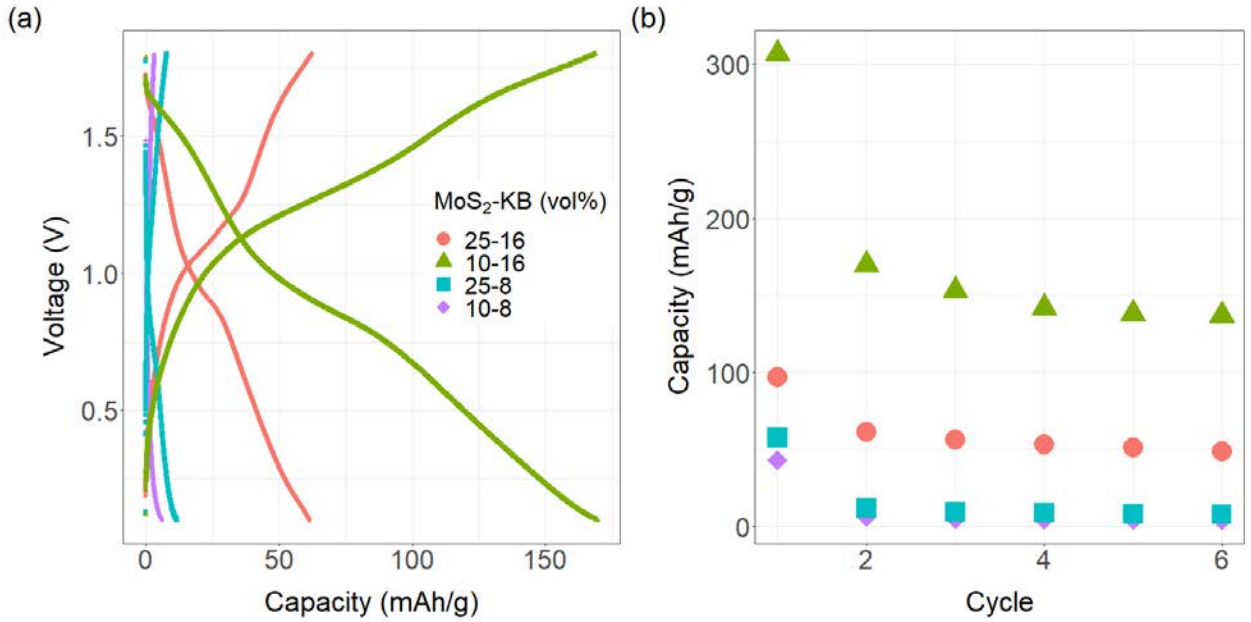

Figure 3.10: (a) 2nd voltage-capacity data (b) discharge capacity for first 6 cycles, for each slurry composition

higher capacity than the 8%vol KB slurries with low Li^+ activity, and this trend is present in Fig 3.10a and 3.10b. The capacity data follows the trend presented in the electronic conductivity data, with the both capacity and electronic conductivity data following the order of $10MoS_2$-16KB >> $25MoS_2$-16KB > $25MoS_2$-8KB > $10MoS_2$-8KB. The higher ionic conductivity and higher viscosity of the $25MoS_2$-16KB slurry did not lead to superior performance over the $10MoS_2$-16KB slurry. Our data is consistent with theories in the literature than electronic conductivity is rate-limiting in semi-solid electrode systems, and that Li^+ intercalation in the first cycle is a strong predicator of later cycling performance. Due to its high capacity, the $10MoS_2$-16KB slurry composition was chosen for all subsequent studies.

3.6 Conclusion

In this chapter, MoS_2/KB slurries with varying volume loadings have been characterized for their rheological, electrical, and electrochemical performance. Shear thinning rheology was shown in all slurries, indicating the presence of a particle network suspended within the electrolyte. Viscosities varying from 100-30,000cP were measured, showing the critical effect of volume loading on the slurry rheology. Ionic and electronic conductivity was present in all slurries, with both positively correlating to the overall volume loading of the slurry. A notable exception at $10MoS_2$-16KB was observed, for which high electronic conductiv-

ity was observed. Cyclic voltammetry measurements illuminated that 16%vol KB slurries showed strong Li^+ intercalation peaks, which were far smaller in 8%vol KB systems. This result is consistent with cycling data, for which 8%vol KB slurries showed negligible capacity compared to the 16%vol KB slurries. The highest observed capacity was found in the 10MoS_2-16KB slurry system at 165 mAh/g, demonstrating the high potential of the Mg/MoS_2 system to deliver capacity in a semi-solid system.

In the next chapter, the contributions of both Mg^{2+} and Li^+ ions will be explored and quantified. This chapter is focused on the two-ion nature of the electrolyte and its impact on the performance of this slurry flow battery. The use of a dual-ion electrolyte is justified via cells fabricated with Mg^{2+}, Li^+, or Mg^{2+}+Li^+ ions in the electrolyte. To quantify the contributions of both ions at the cathode, ICP-OES measurements are carried out at various stages of cycling. The Li^+ concentration is optimized, resulting in high capacity cells.

Chapter 4

Ionic Mechanisms in Magnesium Slurry Static Batteries

In the previous chapter, initial cycling results showed that MoS_2/KB slurries can exhibit high, reversible capacity. However, the origin of this capacity is not clear. The mechanism for capacity (conversion, intercalation, alloying, etc) has not been confirmed in the literature, with intercalation believed to be the working mechanism. It has also not been studied which ion, Mg^{2+} or Li^+, is active at the cathode, and to what extent either ion is contributing to reversible capacity after the initialization cycle. The results presented in this chapter provide evidence of both ions being active at the cathode and quantifies the extent to which both Mg^{2+} and Li^+ contribute to capacity.

4.1 Experimental methods

Materials

Hydrochloric acid (HCl), nitric acid (HNO_3), 1ppm yttrium standard solution in HNO_3 (Sigma, 75592), 100ppm ICP multi-element calibration solution in HNO_3 (Sigma, 1094920100, solution VIII containing Mg, Li), and 1000ppm Mo solution in HCl (Sigma, 68780) were purchased from Sigma Aldrich and used as received.

Cycling parameters

All cell data in this chapter used the 10MoS_2-16KB slurry composition, and were cycled at a 25mA/g rate. A 0.8M APC electrolyte was used with 0.5M LiCl concentration unless otherwise noted.

Ex-situ sample preparation

For XRD and ICP ex-situ studies, the slurry from cycled cells was extracted and washed. Cells were first disassembled in a N_2 glovebox. The flat end of a PTFE-coated spatula was used to scrape out slurry from the slurry cup, then the cycled slurry was added into an 8mL

glass vial. A glass syringe was used to add 2mL THF to the vial, which was then sealed in the N_2 environment. The vial was removed from the glovebox and agitated on a vortexer for 30sec at 2000rpm. Custom centrifuge baskets were fabricated via 3D printing to hold 8mL vials. The vial was centrifuged for 1min at 5000rpm. The vial was brought into the glovebox, and the supernatant was poured off. The THF addition, agitation, centrifugation, and decanting steps were repeated two more times.

X-ray diffraction

Sample preparation: Cycled powders were first prepared following the ex-situ sample preparation process. After washing the powders, 0.5mL THF was added to the vial. The vial was removed from the glovebox and agitated for 30sec at 2000 rpm via vortexer. After returning to the glovebox, a 1mL glass syringe with 9 gauge needle was used to draw up the agitated solution. Plastic XRD specimen holder trays with ≈0.5mm deep circular wells were fully coated with 2" wide Kapton tape. The agitated mixture was cast into the Kapton tape covered circular well, and left uncovered at room temperature overnight to dry. After the solvent had fully evaporated, an additional piece of Kapton tape was used to cover the powders in the well, forming an airtight seal around the edges. An airtight Nalgene container was used to transport the samples from the glovebox to the XRD machine.

Measurement: The crystallographic characteristics were measured using a D8 Discover GADDS powder X-ray diffractometer with a Cu K-α source from 10-60° at 0.02° steps.

ICP-OES

Sample preparation: Cycled powders were first prepared following the ex-situ sample preparation process. All subsequent work was done in a fume hood in ambient air. Aqua regia was created by mixing 32mL hydrochloric acid and 8mL nitric acid in a 100mL glass beaker. The solution was left to sit for 15mins before use. Using a 1mL polypropylene syringe, 1mL of aqua regia was added to the 8mL glass vial containing washed and dried powders. Vials were placed in an aluminum block holder for 2hrs on a metal-topped hotplate at 95C. The vial was then removed from the hotplate and allowed to cool to room temperature for 15mins. Vials were centrifuged at 5000rpm for 2mins, and the contents were filtered through a 0.1 µm PTFE syringe filter. The filter was used to remove any remaining solids (Ketjenblack is not fully digested by aqua regia) to prevent clogging of the ICP machine. To create the blank, calibration, and digested powder ICP solutions, the final volume was fixed at 20mL. For blank samples, 1mL of aqua regia was combined with 2mL 1ppm yttrium solution and 17mL deionized water. Calibration samples containing 0.01, 0.1, 0.25, 0.5, 1, 2, 5ppm Mg and Li and 0.1, 1, 2.5, 5, 10, 25, and 50ppm Mo were generated by diluting the 100ppm multi-element solution solution and 1000ppm Mo stock solution with deionized water. The calibration samples also contained 1mL aqua regia and 2mL 1ppm yttrium solution. For samples with digested particles, the 1mL of aqua regia with digested powders was combined with 2mL of 1ppm yttrium solution and 17mL deionized water. Finished samples were transferred into a 50mL polypropylene centrifuge tube and sealed until use.

Measurement: ICP-OES measurements were carried out on a Perkin Elmer ICP Op-

tima 7000 DV Spectrometer. The wavelengths (nm) were used for element detection: Mg (285.213), Li (610.362), Mo (202.031), Y (371.029).

4.2 Mg^{2+} and Li^+ ion dependence in MoS_2-KB slurry electrolyte

Initial cycling data using the hybrid electrolyte showed promising capacity, but the role of each ion (Mg^{2+}, Li^+) remained unclear. To establish if either ion alone could sustain reversible capacity, cells were fabricated using one of 3 electrolytes: Mg-only (0.8M APC, Mg^{2+} ions), Li-only (0.5M LiCl in THF, Li^+ ions), or Mg+Li (0.8M APC + 0.5M LiCl, Mg^{2+} + Li^+ ions).

For these three electrolyte compositions, only the hybrid Mg+Li electrolyte showed high, reversible capacity (Fig 4.1). The Li-only electrolyte produced high discharge capacity during the initialization cycle (cycle 1), but this capacity rapidly faded and was not able to sustain past the third cycle. This discharge capacity likely originates from Li^+ intercalation into the MoS_2 in the cathode. The inset for Fig 4.1 shows the charging capacity for the three electrolyte compositions. The Li-only electrolyte is unable to produce significant charging capacity during any cycle; with no Mg^{2+} in the electrolyte, there is no Mg plating onto the anode to provide electrons to the cathodic reaction during charging. The Mg-only electrolyte showed low capacity throughout all cycles. This result is expected, as Mg^{2+} cannot intercalate into the 2H-MoS_2 used in the cathodic slurry without the phase transformation initiated by Li^+ ions. The Mg+Li electrolyte shows high discharge and charge capacity which is reversible over all 10 cycles. This behavior is consistent with the proposed mechanism, where Li^+ intercalation causes a phase transformation in the MoS_2, increasing interlayer spacing and improving the intercalation kinetics, allowing both ions to react at the cathode. This data justified the need for a hybrid-ion electrolyte, as neither ion alone was able to show high, reversible capacity, and showcased the critical role of Li in this Mg/MoS_2 system.

4.3 Quantitative analysis of Mg^{2+} and Li^+ participation at the cathode

The data in Fig 4.1 is consistent with previous reports, which suggest that Li is a critical part of Mg/MoS_2 intercalation material system [98]. It is not yet understood if each ion is active at the cathode. The cyclic voltammetry results presented earlier in this work suggest Li^+ intercalation is occurring at the cathode, for at least the initial few cycles. However evidence of intercalation as the capacity mechanism is lacking. It is also unknown if Mg^{2+} is active at the cathode at all, or if only Li^+ ions are participating in the cathodic half cell.

To provide evidence of the reaction mechanism and quantify the contribution of Mg^{2+} and Li^+ ions, inductively coupled plasma (ICP) measurements were carried out. Cells were

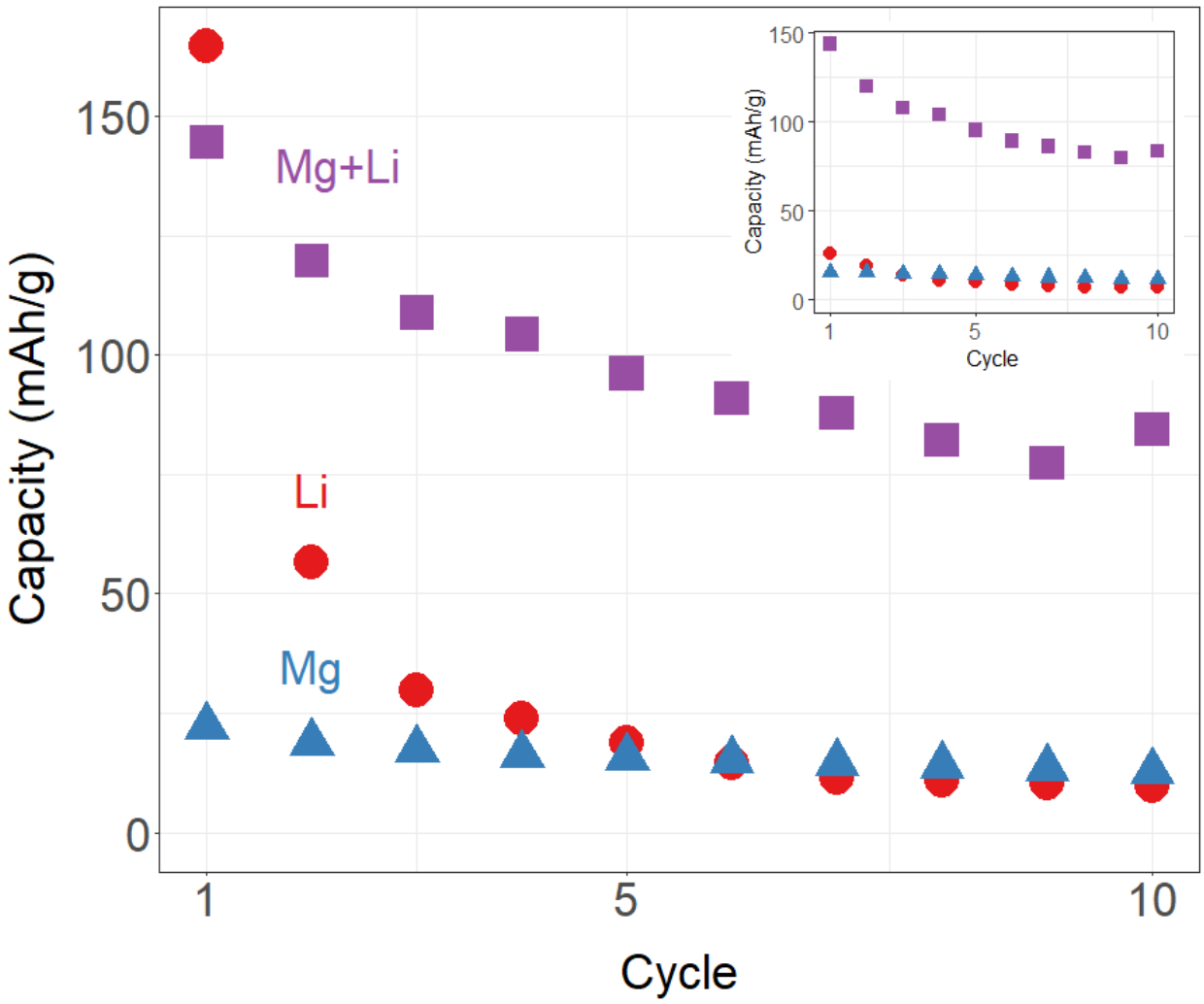

Figure 4.1: (main) Discharge capacity data (inset) charge capacity data from cells made with either LiCl/THF (Li), APC (Mg), or APC+LiCl (Mg+Li) electrolytes.

cycled to charged and discharged states for varying numbers of cycles. The cells were then disassembled, the cathodic slurry (MoS_2/KB) was removed and dissolved in a strong acid (also known as digestion), and the resulting solution contained dissolved MoS_2 and all of the ions found within the MoS_2. ICP measurements quantified the concentration of Mg, Li, and Mo in this solution. By tracking the concentration of these elements as a function of charge/discharge cycle, the contribution of Mg and Li during cycling can be understood.

ICP measurements require all solid particles to be dissolved into a solution for analysis. This necessitates ICP as a bulk measurement technique, which is not surface limited and captures the entire sample volume without rastering. Other chemical analysis methods are restricted by depth limitations (XPS: <10nm, EDX: ≈1um) and require beam rastering to measure large areas. The resolution of ICP (≈1ppb for most compounds) is far greater than is needed for this experiment.

Fig 4.2 shows the ICP data, which is normalized to the molybdenum (Mo) concentration in solution to establish a ratio of ions (Mg, Li) to active particles (MoS_2). The full cycles (0.0, 1.0, 2.0) along the x-axis correspond to cells in the charged (deintercalated) state, while half cycles (0.5, 1.5, 2.5) correspond to cells in the discharged (intercalated) state.

To prepare battery electrodes for ICP, the electrode from a disassembled cell has to be washed to remove any residual electrolyte that may be present on the particles. This excess electrolyte contains Mg^{2+} and Li^+ ions, and will skew the ICP data by including ions that are on the particle surface but are not intercalated. It is important to verify that the washing procedure can sufficiently remove any surface/residual material, so that the only measured Mg and Li in the sample come from intercalated ions. The first data point in Fig 4.2 at cycle 0.0 shows the Li and Mg concentration in a control cell that was assembled but not cycled, and then washed per the stated procedure. In this cell there was no applied voltage to drive intercalation, thus there should be no Mg or Li present in the particles after washing. While Mo was detected in this control sample, proving that the particle digestion was successful and that MoS_2 was present, negligible amounts of Li and Mg were detected. This data verifies that the washing procedure successfully removed excess electrolyte from the powders. It also indicates that any Mg or Li detected by ICP can be attributed to cycling of the slurry.

Looking at Fig 4.2, the overall movement of Mg^{2+} and Li^+ ions can be charted. At each half cycle (cycle=0.5, 1.5, 2.5), the cell is discharged to 0.1V, and ions are intercalated into the MoS_2. This is reflected in the increased amount of Mg and Li seen in the half cycle states. At each full cycle (cycle=1.0, 2.0), the cell has been charged to 1.8V, and ion deintercalation occurs. This is observed in Fig 4.2, where the Mg and Li concentrations decrease relative to the previous discharge state. This behavior is reversible, and repeats several times during this experiment.

In the charged states, some Mg and Li is still present. This is likely due to trapped charge, as the result of either the 2H-MoS_2 → 1T-MoS_2 phase transformation or ion intercalation during the first discharge cycle. The quantity of trapped Mg and Li ions is relatively constant between the first and second cycle, consistent with the theory that charge is trapped irreversibly during the initialization cycle but subsequent cycles are highly reversible.

The change in Mg and Li concentration during cycling was used to understand which

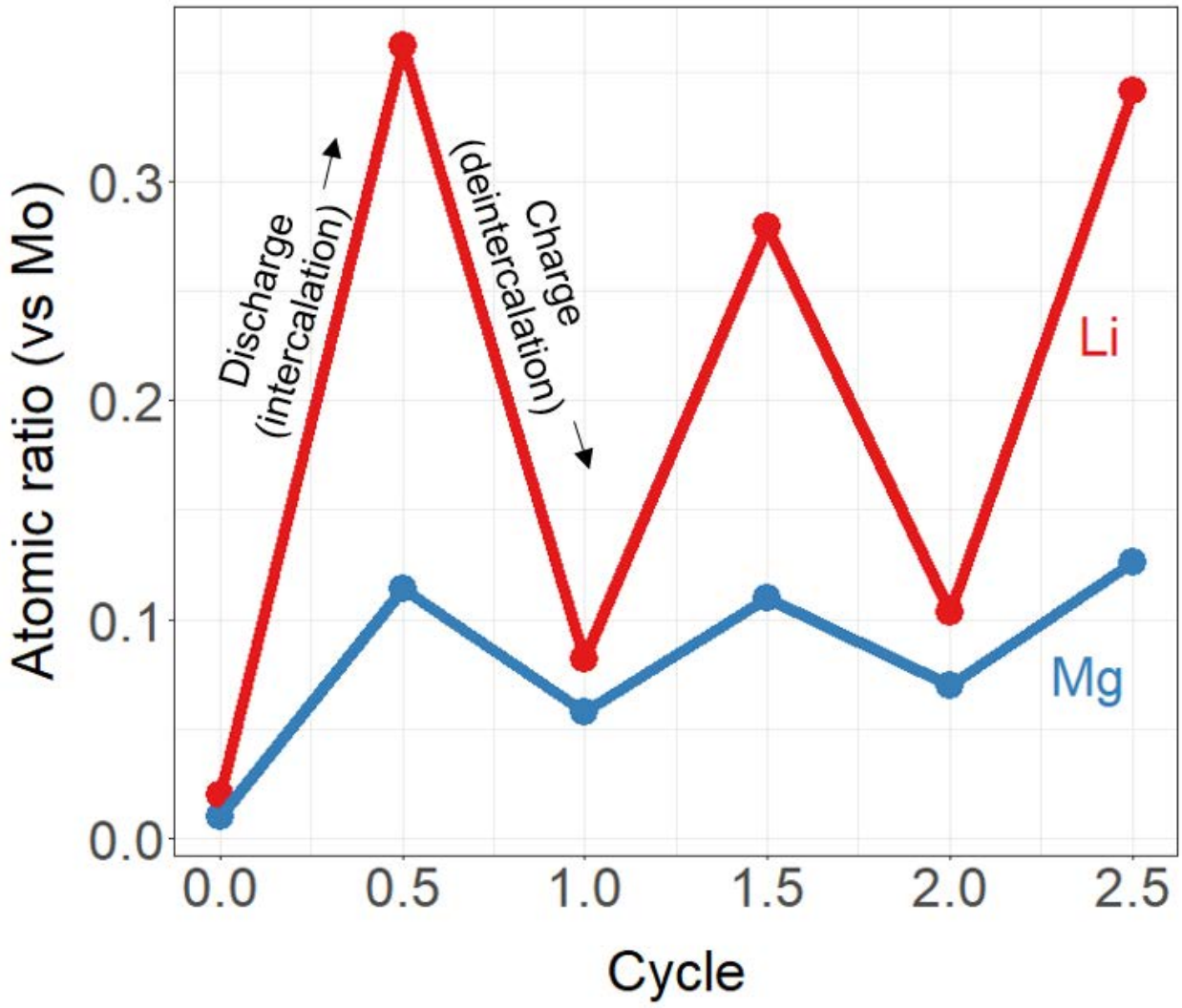

Figure 4.2: ICP data, normalized to Mo concentration, showing the Li and Mg concentration as a function of cycle life. Half cycles show a discharged cell where full intercalation is expected, full cycles show a charged cell where complete deintercalation is expected.

ions are participating in the cathodic reaction. The Li concentration seen in Fig 4.2 varies during cycling, increasing during charging and decreasing during discharging, indicating Li is participating in a reaction at the cathode. This result was expected based on the peak around 0.2V in the cyclic voltammetry data, and confirms that Li is active at the cathode. The concentration of Mg also increases during discharging and decreases during charging, indicating that Mg is also active at the cathode. Previously, Mg activity in a 1T-MoS_2 cathode had not been verified by experimental data. Equations 4.1-4.3 detail the proposed system of reactions within the Mg-Li/MoS_2 battery.

Anode reaction:

$$Mg \Leftrightarrow Mg^2 + + e^- \tag{4.1}$$

Cathode reactions:

$$6MoS_2 + 4Mg^{2+} + 8e^- \Leftrightarrow Mg_4Mo_6S_{12} \tag{4.2}$$

$$MoS_2 + Li^+ + e^- \Leftrightarrow LiMoS_2 \tag{4.3}$$

The relative amounts of each ion were calculated in order to compare the contributions of Mg and Li ions at the cathode. Across all discharge cycles in this experiment, Li is found at 2:1 ratio to Mg, after subtracting out the trapped charge measured in the charged states. This data confirms that Li is the primary contributor to capacity on the cathode side. From this data, Li is estimated to contribute approximately 2/3 of the capacity at the cathode.

4.4 Structural evolution of MoS_2 during cycling

To corroborate the 2H-MoS_2 $\rightarrow$ 1T-MoS_2 phase transformation suggested by cyclic voltammetry and provide evidence of intercalation as the reaction mechanism at the cathode, ex-situ XRD was carried out. Cycled powders were washed, sealed in Kapton-coated trays, and their x-ray diffraction patterns were measured. Fig 4.3a shows the XRD data at various stages of cycling. The top and bottom data sets are 2H-MoS_2 and 1T-MoS_2 reference data from the JCPDS database and are included for comparison.

As shown in Fig 4.3a, the peaks measured in the raw slurry powders (10MoS_2-16KB blend) are consistent with 2H-MoS_2, with the (002), (100), (101), (103), (006), (105), and (008) peaks present. After the first discharge cycle, all higher angle peaks diminish, leaving only the (002) peak in subsequent cycles. The loss of higher angle peaks suggests that the 2H-MoS_2 phase has transformed, but the new phase of MoS_2 cannot be identified from from this data alone. Differentiating between 2H-MoS_2 and 1T-MoS_2 is difficult as the (002) peak for both spectra are both around 14.4°. However, taken with the prominent peak at 0.2V in the CV data, and the ability for Li to intercalate shown in past literature, we believe the new phase of the cycled MoS_2 powder is 1T-MoS_2. Peak shifting or broadening was not detected in these samples, and further evidence of intercalation was therefore not able to be found in the diffraction data (see Fig 4.3b).

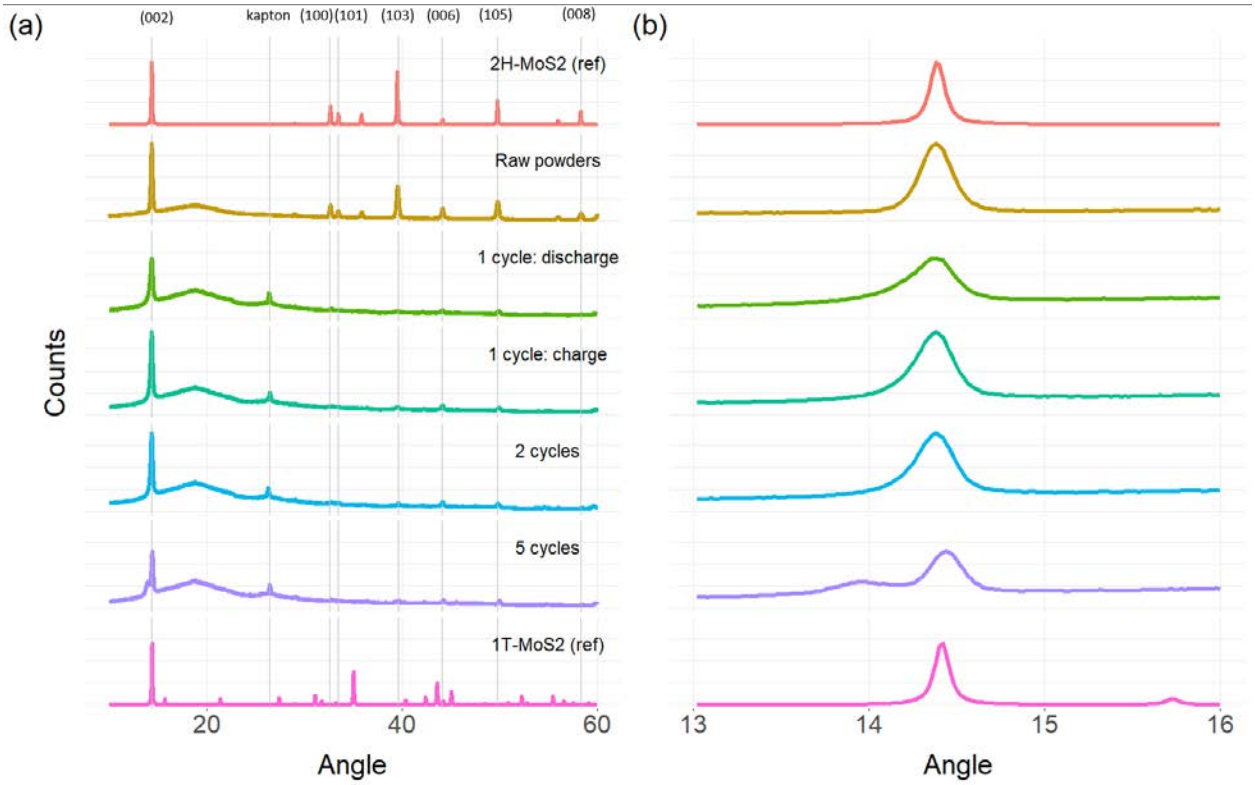

Figure 4.3: (a) XRD spectra from cells cycled to different voltages. Cells with (ref) are reference data from JCPDS database (b) (002) peak for each sample

4.5 Optimizing Li^+ concentration in APC electrolyte

With the critical role of Li^+ ions in the Mg/MoS_2 material system established, the optimal concentration of Li+ was investigated by varying the amount of LiCl added. The addition of LiCl to the APC electrolyte is expected to increase capacity, as more Li^+ ions are available for intercalation. The solubility limit of LiCl in APC is ≈1M, which bounded the maximum Li^+ in the electrolyte. Fig 4.4 shows the discharge capacity for 4 cells at each LiCl concentration, after an initialization cycle was completed. As was seen in Fig 4.1, the capacity of cells with 0M LiCl is negligibly small. A monotonic increase in capacity is observed with increasing Li^+ concentration, resulting in an average capacity of 175mAh/g at 1M LiCl concentration. All subsequent cells were fabricated using 1M LiCl with the 0.8M APC electrolyte

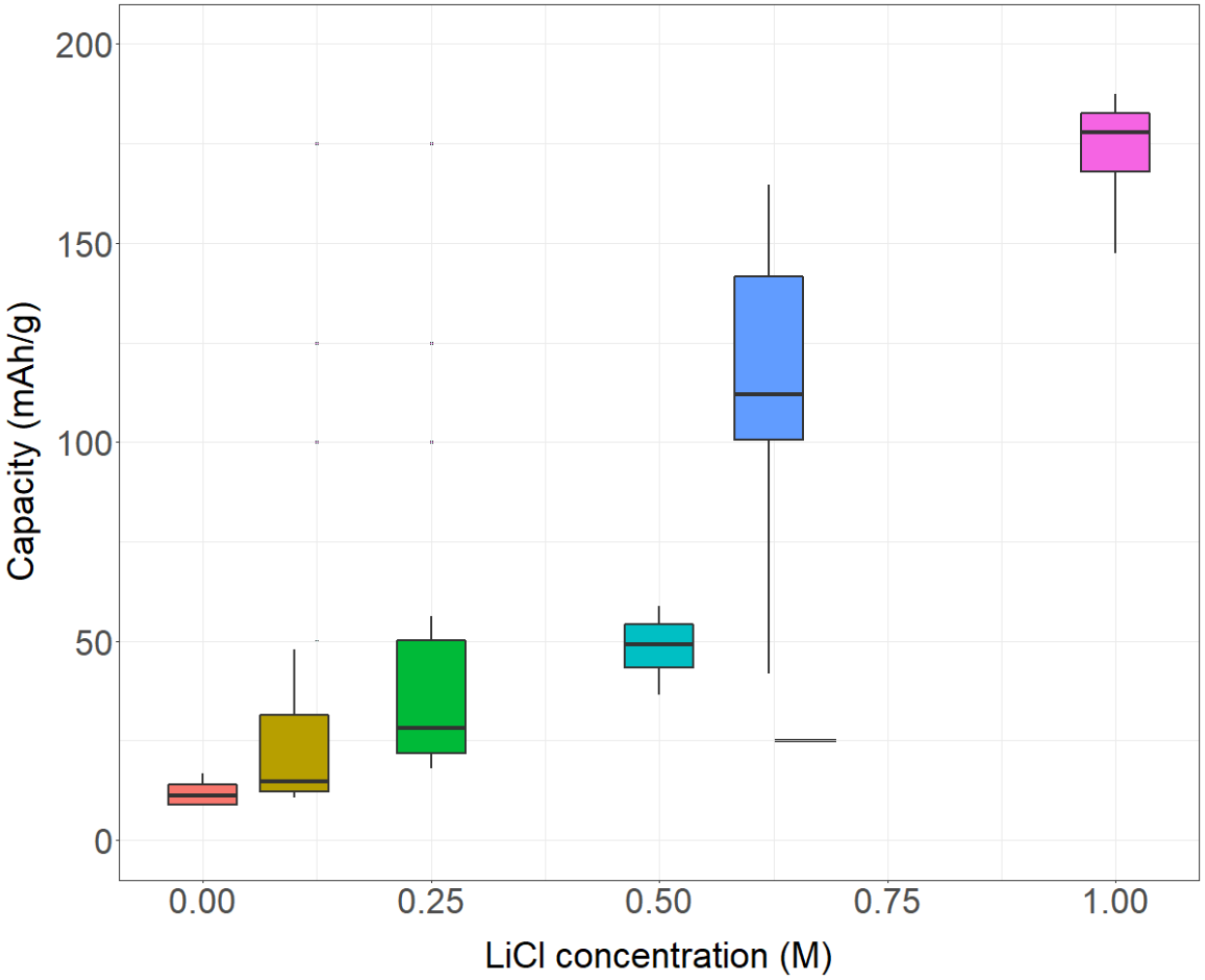

Figure 4.4: Discharge capacity with varying LiCl concentration, for 2nd cycle (after initialization cycle). Each boxplot represents 4 cells at that condition. The horizontal black bar within the boxplot represents the mean of sample data.

4.6 Conclusion

In this chapter, the mechanisms that contribute to capacity at the cathode and the relative contributions of each ion were studied. Cells fabricated with either Mg ions, Li ions, or Mg + Li ions solidified the need for both Mg^{2+} and Li^{+} ions in this MoS_2 slurry system, as electrolytes with either of these ions were unable to provide high, reversible capacity in a full cell. Cells with both ions were able to sustain high capacity (≈100mAh/g) for 10 cycles. ICP-OES measurements on ex-situ samples were used to quantify the ions present in discharged and charged cells. Both Mg and Li were found to vary during charge and discharge, which confirmed that both ions are active at the cathode. Overall, Li existed at a 2:1 ratio to Mg in the ICP samples, and Li is therefore expected to contribute 2/3 of the capacity at the cathode. XRD on cycled powders was unable to provide clear evidence of intercalation or 2H-MoS_2 → 1T-MoS_2 conversion in this system. After varying the LiCl concentration in the electrolyte, the optimal concentration was determined to be 1M, leading to a capacity of 175 mAh/g.

Chapter 5

Rate and Cycling Performance in Static and Flow Slurry Batteries

In previous chapters, the design and optimization of a MoS_2-KB-APC-LiCl slurry composition has been explored, and the contributions of both Mg^{2+} and Li^+ ions to cell capacity have been quantified. In this chapter, the rate and cycling performance of the optimized slurry (10MoS_2-16KB, 0.8M APC + 1M LiCl) are characterized. Flow cell hardware is introduced in this chapter, to explore how flow affects the long term cycling capacity of our slurry. Measurements from both static and flow cell hardware are presented; this benchmark data helps identify areas for improvement in the Mg-MoS_2/KB slurry battery system.

5.1 Experimental methods

C-rate cycling protocol

For C-rate measurements, 10MoS_2-16KB cells with 0.8M APC + 1M LiCl electrolyte were assembled. Cells were allowed to equilibrate for 15min, then an initialization discharge-charge cycle was run. Following a 15min rest after initialization, the cell was discharged and charged in the order of 10, 25, 50, 100, 250 and 1000 mA/g, using a voltage range of 0.1-1.8V. Between each current density, cells were left to rest at open circuit for 15mins.

Flow cell assembly

1x3x6" thick Teflon PTFE block (#8743K24), 3/4x1x12" stainless steel 316 bar (#9083K47), 0.003" thick PTFE film (#8569K36), 0.01" thick SS316 sheet (#3774T59), 25mm long M3 screws (#91292A020), SS316 M3 wingnuts (#94543A320), Luer lock to 1/4"-28 pipe adapters (#51525K318) and 1/8" inner diameter (ID) Luer lock connectors (#51525K322) were purchased from McMaster Carr.

The flow channel block was machined from the SS316 bar (to the dimensions shown in Fig 5.1a). The top Teflon housing and bottom Teflon baseplate pieces were machined from the Teflon block (Fig 5.1b,d). Celgard 2325 and PTFE films were laser cut to the dimensions in

Fig 5.1e and 5.1f, respectively. 10mm thick acrylic endplates, cut to the same dimensions as the Teflon baseplate, were attached on the outside of the cell assembly to provide mechanical strength under compression. A 15x10mm metal plate was cut from the 0.01" SS316 sheet to prevent contact screws from puncturing the Mg foil. Magnesium foil was polished as previously described, and cut to 13x6mm.

All assembly steps were carried out in a N_2 glovebox. Four M3 screws were inserted facing upwards through an acrylic endplate and then the Teflon baseplate. The SS316 plate was placed in the center of the baseplate, and the Mg foil was placed on top of the SS316 plate. Kapton tape was applied to the edges of the SS316 plate and Mg foil to secure them to the Teflon baseplate. The M3 screws were pushed through the corner holes of the Celgard 2325 sheet, and the sheet was gently pulled down until it contacted the Mg foil. The same procedure was used to attach the PTFE film on top of the Celgard sheet. The flow channel block was inserted into the top Teflon housing, such that the flow channel was flush with the wide base of the top Teflon housing. The housing and flow block were pushed down onto the M3 screws until the flow channel was in contact with the PTFE-Celgard-Mg-SS316 sheet stack. An acrylic endplate was added above the top Teflon housing, and then wingnuts were tightened on each M3 screw to compress the stack together. Threaded Luer lock to 1/4"-28 connectors were screwed into the inlet and outlet threads of the top Teflon housing. An M3 screw was screwed into the center hole in the top and bottom Teflon housings, until contact with the flow channel block or SS316 sheet was made, respectively. Two 3" length 1/8" ID PFA tubing segments were cut, and male Luer lock connectors were inserted into the ends of both pieces of tubing. These pieces were attached to the Luer lock connectors to the flow cell. Photographs of the assembled cell and its components are shown in Figure 2.22.

10MoS_2-16KB slurry was prepared as previously described, and added into a 10mL Hamilton glass syringe barrel using a PTFE-coated spatula. The syringe plunger was carefully reinserted into the syringe, and used to push out all air bubbles from the syringe. The syringe was then connected to the inlet tubing of the flow cell via the Luer lock tip, and then mounted into a syringe pump (NE-1000, New Era Pump Systems). The syringe pump was connected via RS232 connection to a laptop. WinPumpTerm software controlled the syringe pump. The flow cell remained in the glovebox throughout all testing, and was connected to the laptop via an external feedthrough in the glovebox.

Flow cell operation

For cycling in a flow cell, an aliquot of slurry is pumped into the flow channel. The channel, colored in black in Fig 5.1a, is the d=1mm half-circle exposed area at the base of the channel block (see Fig 5.1c) and the 1mm diameter segment immediately adjacent to the exposed area. The channel has a volume of 12.5uL. For flow cell experiments, a volume of 15uL was pumped in per aliquot, at a rate of 200uL/min. A voltage range of 0.1-1.8V was used for all cycling. A Neware BTS battery analyzer was used to collect cycle data.

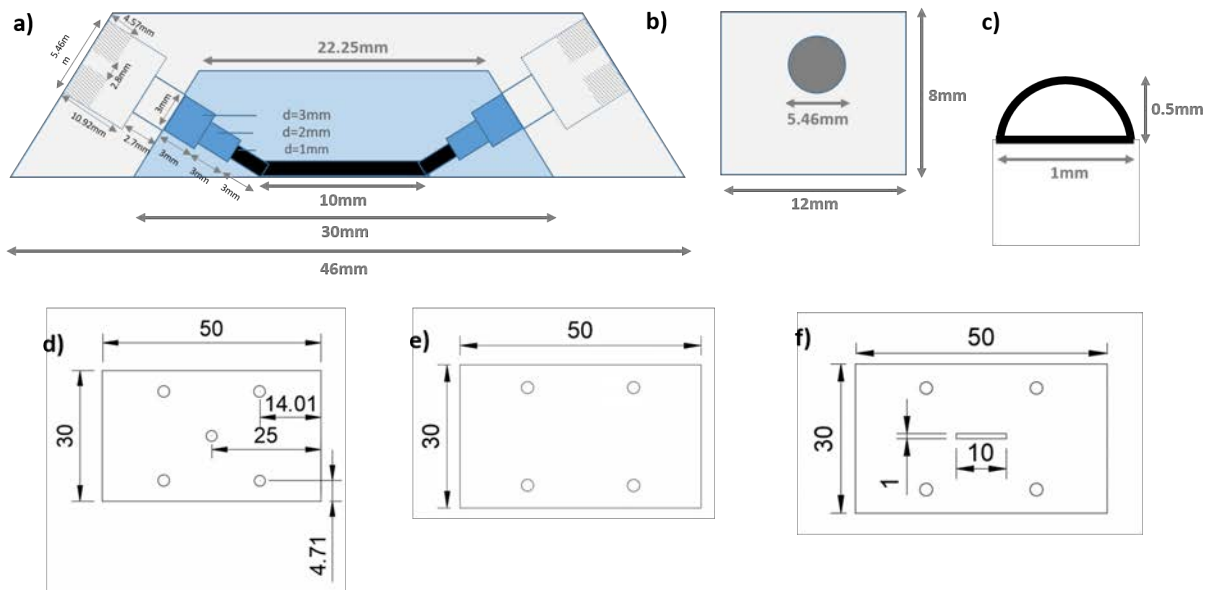

Figure 5.1: Flow cell schematics, in mm, of the a) side view of top Teflon housing (gray) and flow channel block (blue), with the flow channel of d=1mm (black) b) front view of top Teflon housing c) cross section of the flow channel d) top view of Teflon baseplate, with M3 screwholes shown e) top view of Celgard 2325 sheet f) top view of PTFE film

5.2 Rate Performance

To assess the rate capability of the optimal slurry composition (10MoS_2-16KB, 0.8M APC+1M LiCl), C-rate discharge tests were performed. While the static and flow hardware were designed to have the same working distance (0.5mm) for both channels and are expected to have similar performance, both hardware configurations were tested for their rate capabilities with the optimal slurry formulation, and the results are shown in Fig 5.2. Fig 5.2 shows the discharge capacity across a range of current densities from 10-1000mA/g (from C/25 to 7.5C, as determined by the length of each discharge cycle). Similar rate performance is found between the two cell hardware types. At the lowest current density, a discharge capacity of 225mAh/g is measured, in close agreement with previous results presented in this work. At 1.2C, a discharge capacity of 95mAh/g is found, resulting in 42% capacity retention from the C/25 case.

Achieving moderate performance at C/2.5 and 1.2C is a substantial milestone for this novel slurry material set, and provides a demonstration that slurry electrodes, thought to be limited by high electrical resistivity, can potentially be optimized for moderate and high power applications. In conventional battery cells, the volume fraction of conductive additive is increased for high power applications in an effort to lower resistive losses at high current densities. A similar strategy could be employed with slurry electrodes, with the slurry being

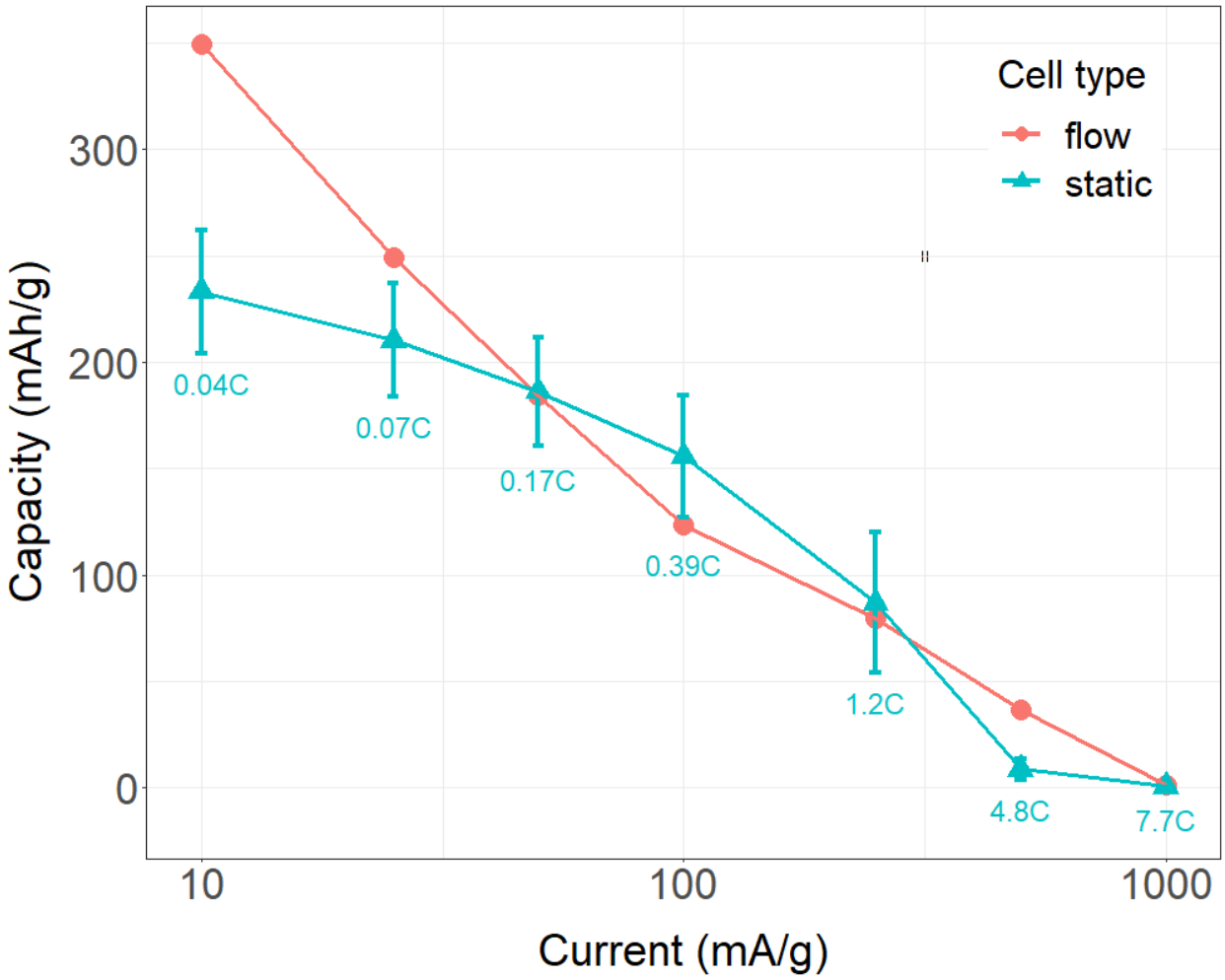

Figure 5.2: Rate performance data for static and flow hardware. A 10MoS_2-16KB slurry with 1M LiCl was used in both cell types. Error bars for static cell data represent n=4 samples

tailored for application specific performance such as high rate operation.

Fig 5.3 shows the discharge capacity of static cells, at 10 and 50mA/g initialization rates and 10-250mA/g cycling rates. Low discharge rates produce capacities of 150-200mAh/g across the 10 cycles, further confirming the reversibility of this anode-cathode pairing. This data is in agreement with the cycling data in Chapter 4, showing capacity loss is over the first 10 cycles, but appearing to level off after the initial 5 cycles. The decreasing capacity in the first several cycles is potentially caused by an on-going 2H→1T MoS_2 phase transformation occurring over the first ≈5 cycles, as was observed in CV data. Once the MoS_2 phase transformation is complete, those reactions are irreversible, and therefore would not affect

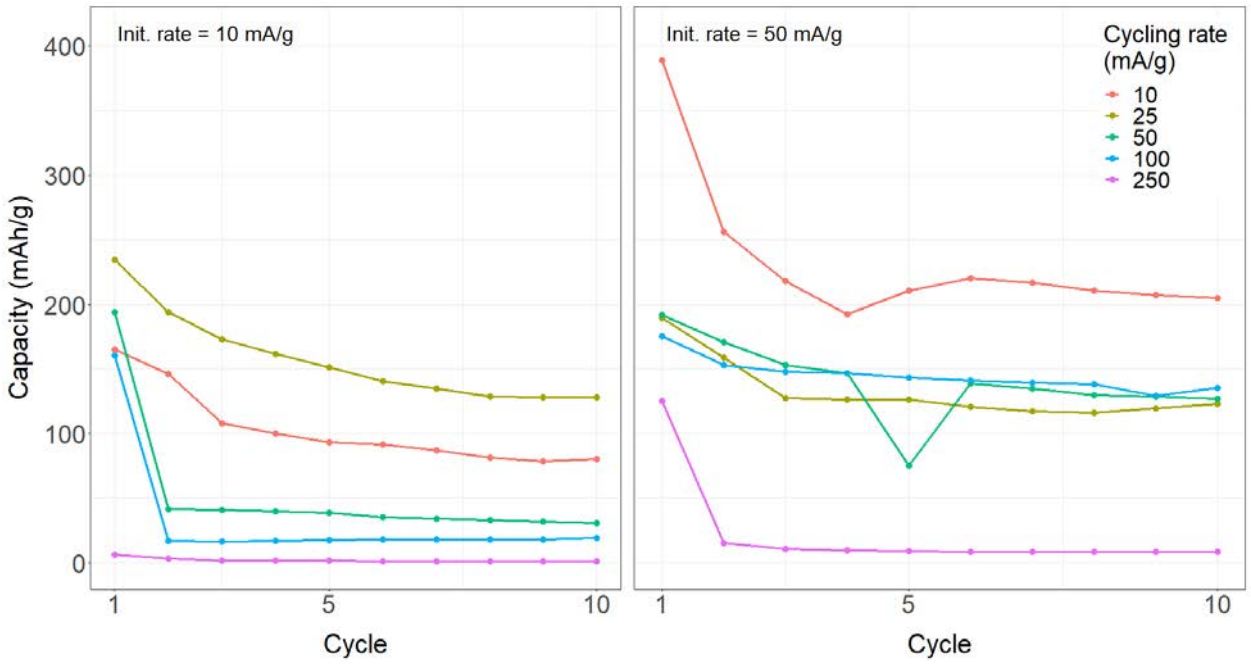

Figure 5.3: Discharge capacity of static cells through 10 cycles, at various current densities and initialization rates. The initialization cycle capacity is not shown.

capacity in future cycles. This may explain the slower rate of capacity decrease after cycle 5 is reached in Fig 5.3.

At both initialization rates, a general trend is observed; higher cycling rates lead to lower capacity. This is expected due to increasing ohmic losses at higher currents, which are particularly of concern in a slurry battery due to the challenge of forming a percolating conductive network as a suspension. It is presently unknown why higher capacities are found in the 50mA/g initialization rate samples than at 10mA/g and further measurements are required to confirm this effect.

5.3 Cycle Life

A cycling study was conducted to evaluate the slurry cycle life in both static and flow cell hardware. The static cells underwent an initialization cycle (not shown) at 50mA/g, and were cycled at 100mA/g for all subsequent cycles. The flow cell used an aliquot pumping scheme for repeated cycling. An aliquot of slurry was pumped into the flow cell channel via syringe pump. A 50mA/g discharge-charge initialization cycle was run to transform the slurry in the channel from 2H→1T-MoS_2, followed by a 100mA/g discharge-charge cycle. The 100mA/g cycle data was the data of interest in this experiment, and can be directly

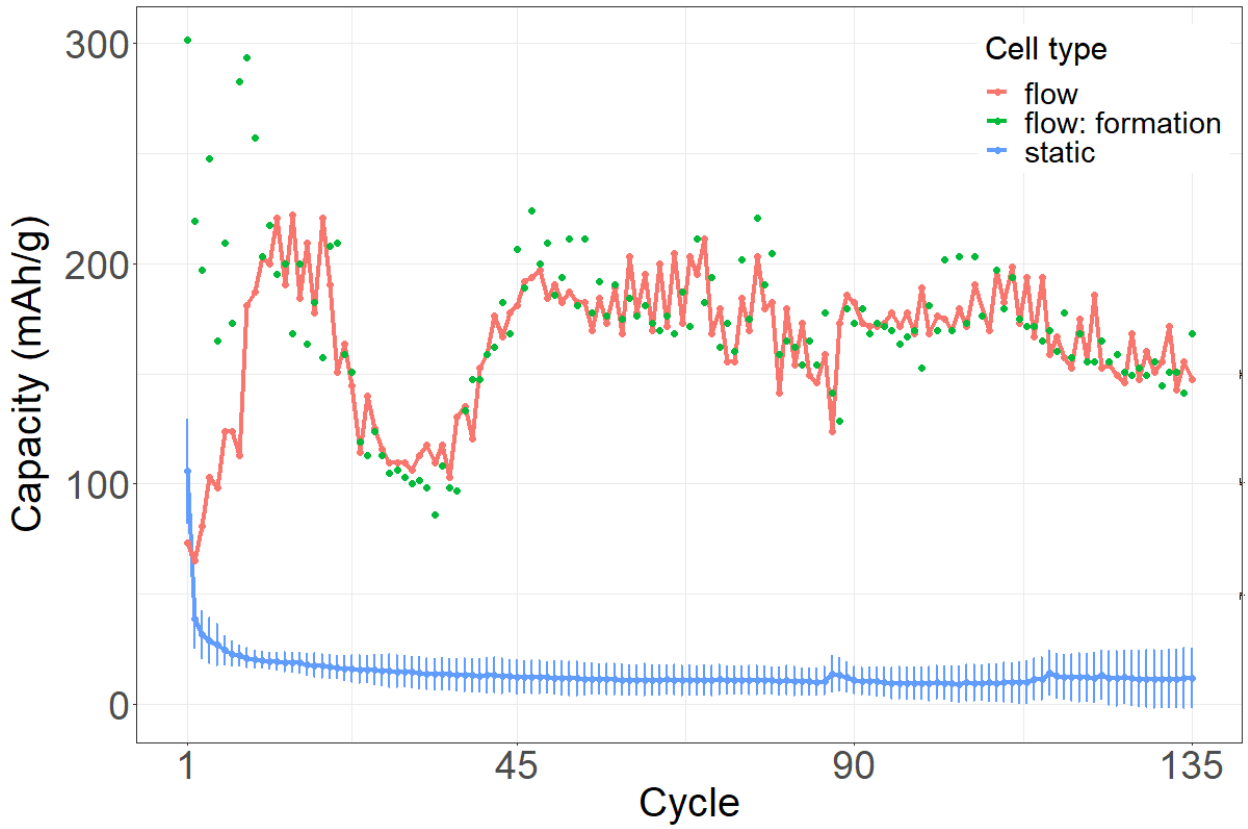

Figure 5.4: Cycle life data for static and flow cell hardware. A 10MoS_2-16KB slurry, 0.8M APC+1M LiCl slurry was used in all cells. Initialization cycles (not shown) were run at 50mA/g, while all other cycles were at 100mA/g.

compared with the static cells. A new aliquot of slurry was then pumped into the cell, and this two step cycling protocol was repeated.

Fig 5.4 shows the cycling data across 135 cycles, for a 10MoS_2-16KB, 0.8M APC + 1M LiCl slurry in static and flow cell hardware. The green data points represent the 50mA/g initialization cycles in the flow cell, the red data points represent the flow cell discharge capacity for 100mA/g cycles, and blue data points correspond to 100mA/g cycles in the static cell.

The static cell shows similar behavior to the data in Fig 5.3, where capacity drops after the first cycle after initialization, then declines more slowly in subsequent cycles. The absolute capacity observed in the later cycles is around 20-40mAh/g, and is consistent between the 3 samples that comprise the error bars.

The flow cell shows a significant increase in capacity in the first few cycles, for reasons that are not yet clear. After this period, the capacity stabilizes around 150-160mAh/g.

It is important to note that when calculating the volume of MoS_2 in the channel for the flow cell, only the sections of flow channel with a radius of 0.5mm were included (see Fig 5.1a). Larger radius sections within the flow channel block, while having metallic walls that could potentially allow for electron conduction to the active sites in the slurry, have a much lower probability of contributing to capacity due to the longer path length across the slurry. It is therefore possible that some slurry in the larger radius sections of the flow channel block contributed to capacity, and caused our absolute capacity values to be overestimated. Regardless of the exact magnitude of the capacity, the flow cell aliquot pumping scheme utilized here showed stable, reversible capacity across 135 cycles. The results in Fig 5.4 suggest that capacity fading is not significant after the initial few cycles, in both static and flow cell hardware configurations, and that the aliquot pumping scheme can deliver stable capacity in the slurry flow cell hardware.

5.4 Irregularities observed during long term cycling

During the long term cycling data gathered in static cells, spikes in the charging capacity data were observed on multiple occasions. A spike in capacity is defined here as a substantial increase in capacity relative to the previous cycles, typically only lasting one cycle before returning to the range of previously measured values. Fig 5.5a-c showcases spiking behavior in the 10MoS_2-16KB slurry, cycled in static cell hardware at 50mA/g, 100mA/g, and 250mA/g respectively.

Spiking behavior was observed repeatedly across different cycling conditions, but had several common characteristics:

- In most cases, the capacity significantly exceeds the theoretical capacity of MoS_2 (670mAh/g), suggesting the origin of capacity during a spike cannot be fully attributed to intercalation. The dashed line in Fig 5.5a-c is included for visual reference of the theoretical capacity of MoS_2.
- Capacity spikes were only observed during charging, not during the discharge of a cell.
- Spikes appear suddenly, and are typically not preceded by irregularities in preceding cycles. Some variation was observed in the coulombic efficiency data for the cycles preceding a spike (Fig 5.5d-f), but it is unclear if this is a related phenomenon.
- Spiking behavior was not seen in the flow cell. Fewer cells were tested on the flow cell hardware and there may have been insufficient samples to observe this behavior.
- Spiking was observed across both initialization rates and all cycling rates which reached high cycle counts.
- Spiking behavior was not seen in the first several cycles, and was typically seen >100 cycles into cycling data. This likely explains why low-rate cycling, which only reached 25-40 cycles, did not exhibit any irregularities.

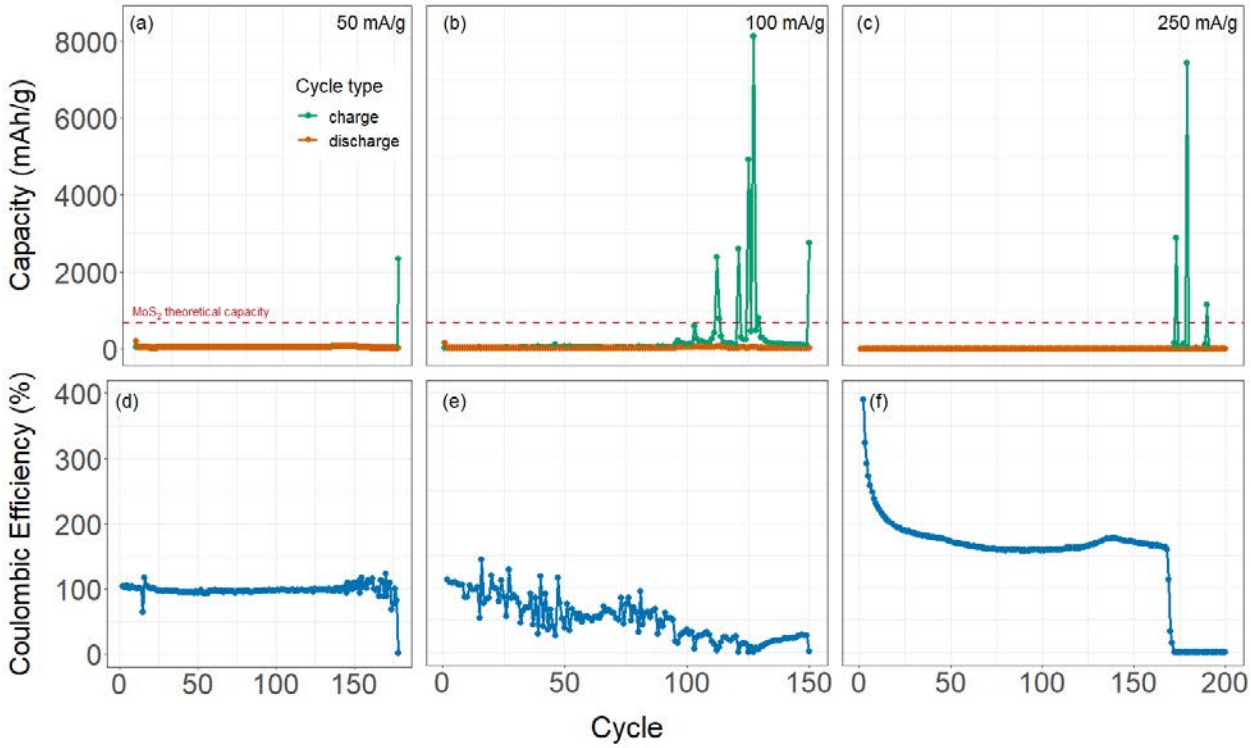

Figure 5.5: Charge-discharge data and coulombic efficiency data for cells showing charging capacity spikes. The cycling rates for each cell are a,d) 50mA/g b,e) 100mA/g c,f) 250mA/g

While some cells recovered from a spike in charging capacity and resumed normal cycling after the irregular charging phase completed, other cells did not recover. Fig 5.6ab shows two cells that highlight the two voltage profiles seen during a charging capacity spike. In the final cycle of Fig 5.6a, the cell voltage reached 1.7V before abruptly dropping to 1.25V, then further dropped to 1.1V where the voltage plateaued. The voltage in this cell remained around 1.1V until cycling was terminated (see Fig 5.5a for the complete cycling data for this cell). Fig 5.6b shows an alternative voltage profile from a different cell. Charging cycles in this cell commonly lasted 1-2 hours, but as can be observed in the data, some charging cycles ran for >20hrs before reaching the cutoff voltage of 1.8V. The charging rate for all cycles in this cell was 100 mA/g, but the voltage increase was substantially slower for these long lasting charging cycles. The capacity in these extended charging cycles far surpassed the theoretical capacity of MoS_2, creating uncertainty as to the origin of this capacity. These two different voltage profiles suggest that two different failure mechanisms may be occurring.

Further analysis is required to understand the modes of failure highlighted by this data. As the spiking behavior is only observed during charging, this should provide evidence as to the underlying issue. During charging, Mg^{2+} ions are deintercalated, travel through the

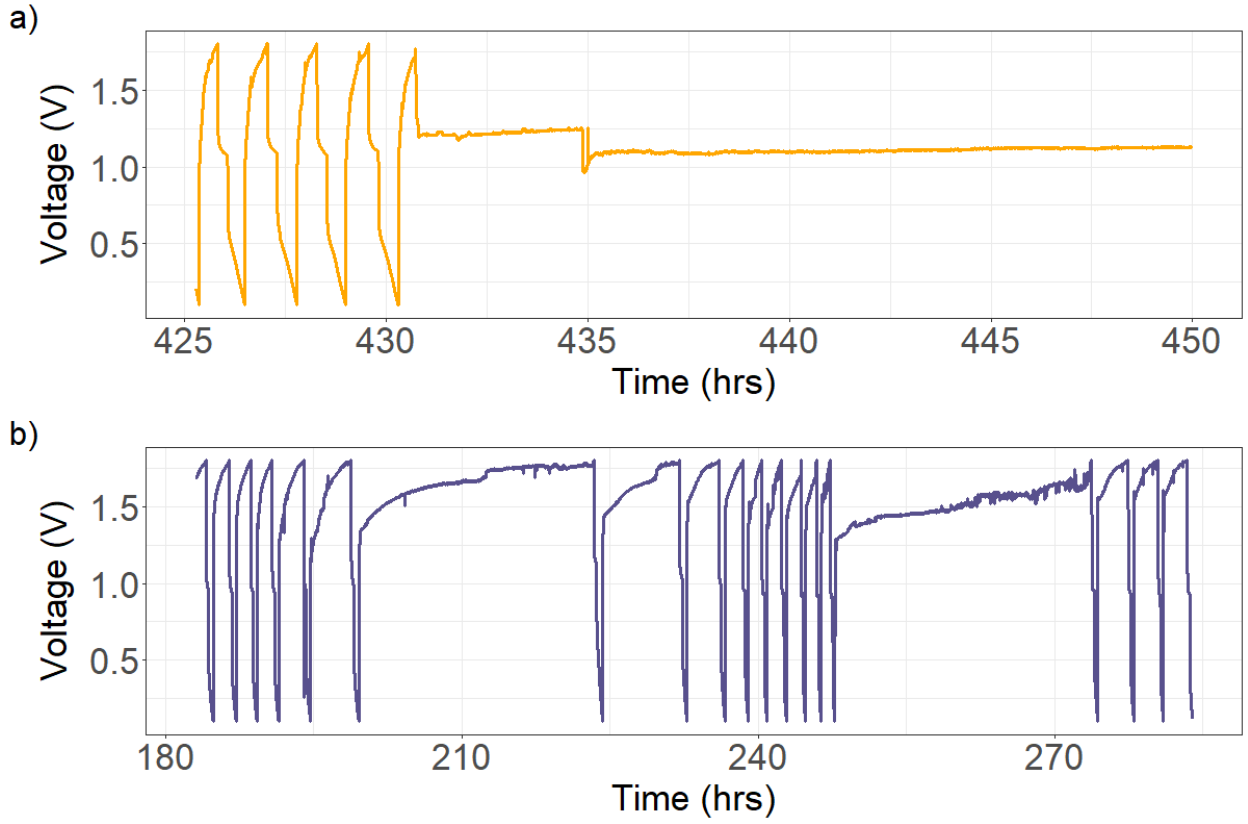

Figure 5.6: Voltage-time plots for two static cells exhibiting a) 1.1V voltage plateau, from which the cell did not recover b) prolonged charging cycles (around 200-220hrs and 250-270hrs) that exceeded the theoretical capacity of MoS_2

electrolyte and across the separator, and plate onto the anode. Li^+ ions deintercalate and remain in the electrolyte. Future studies seeking to identify this failure mechanism could look at the separator integrity optically (microscope, SEM) and electrically (EIS), to look for signs of degradation that may have led to a voltage drop across the separator. Analyzing the surface chemistry of the anode, examined via EDX or XPS, could provide evidence of side reactions that are occurring, which could also explain the change in cell voltage. To isolate the component responsible for the plateau voltage (shown in Fig 5.6a), cells stuck at 1.1V could be disassembled, and a new separator/anode inserted. Upon resuming cycling, successful charge/discharge cycles would indicate an issue with the anode or separator, and further investigations would have a more well-defined target.

5.5 Conclusion

The rate and cycling performance of the optimized MoS_2/KB slurry have been presented. C-rate measurements for both static and flow cell hardware achieve similar capacities, with a peak capacity of 225mAh/g at C/25 and a 42% capacity retention at 1.2C. Reducing overpotentials associated with ohmic losses is a challenge in slurry electrode systems, but represents an area in which the performance of slurry electrodes is poor. Cycling data over 10 cycles reiterated the capacity decrease in the first several cycles, possibly due to a continued 2H→1T MoS_2 phase transition, but showed a far more gradual decline in later cycles. Long term cycling data in the static and flow hardware illustrated a very gradual capacity fade over 135 cycles. Stable capacities were demonstrated via an intermittent aliquot pumping scheme in the flow cell hardware, presenting the first flow cell data for the Mg-MoS_2/KB slurry battery system.

The next chapter presents conclusions drawn from this body of work, as well as recommendations for future research on slurry flow battery materials.

Chapter 6

Conclusions

6.1 Summary

Low cost battery systems are widely desirable, but particularly critical in the context of grid scale storage. Flow batteries have been under investigation for decades as a grid scale battery technology, and while the cell architecture has been validated, the intrinsic material cost and solubility limits have severely limited the cost and commercialization of such systems. Slurry flow battery systems present a pathway to decrease material cost without solubility constraints, but substantial work in understanding the fabrication and composition of a slurry electrode is needed. In this work, the design and characterization of a Mg foil anode, MoS_2/KB cathodic slurry is explored. The studies and results are:

- Design of novel, low-cost Mg-MoS_2 slurry. The material selection criteria and choices for each cell component in this slurry flow battery are presented in this work. The characterization data from multiple slurry compositions to identify suitable concentrations for active and conductive materials and electrolyte additive are included.

- The fabrication procedure for a slurry electrode, as well as the design of cell hardware (static, flow), and handling procedures for this novel form factor cathode are presented. The experimental sections contain details on how the cathodic slurry is fabricated, details about each type of cell hardware, and how measurements like EIS and ICP are adapted to the unique slurry form factor of the cathode. These protocols can be adopted across other slurry flow battery systems, and are expected to provide a detailed foundation for future slurry electrode research.

- Rheological, electrical, and electrochemical characterization of MoS_2/KB slurries. The shear thinning behavior and electrical/ionic conductivity of suspended particle MoS_2/KB networks are measured. Cyclic voltammetry showed reversible electrochemical behavior and provided evidence of Li^+-based phase transformation mechanism in MoS_2 as the first step in reversible capacity MoS_2/KB slurries. These measurements led to the first

demonstration of full cell Mg-MoS_2/KB slurry batteries, from which the 10MoS_2-16KB slurry composition demonstrated high, reversible capacity.

- Quantified Mg^{2+} and Li^+ ion contributions in dual-ion electrolyte. Experimental data validated the need for a dual-ion system, via fabrication of cells with Mg^{2+} or Li^+ ions, which both failed to produce significant capacity. The contributions of each ion during cathodic redox reactions was quantified using ICP-OES, revealing that Li^+ is responsible for $\approx$2/3 of the capacity at the cathode. Magnesium was shown to participate reversibly in this redox reaction, establishing that both ions are active at the cathode.

- Benchmarked rate and cycle performance capability of static and flow cell hardware. A capacity of 225mAh/g was measured at low current density (10mA/g), while 42% of this capacity was retained at a 1.2C rate. Both the static and flow cell exhibited similar discharge characteristics. The cycle life of the static and flow cell hardware was evaluated over 135 charge-discharge cycles. Both cell hardware showed low capacity fading after the initial cycles, with the flow cell exhibiting higher capacity than the static cell.

The key result in this work is the use of a low cost anode and cathode material in a high capacity slurry flow battery. We have shown here the rationale behind the slurry and hardware design, and characterized critical aspects of the slurry (rheology, conductivity, reversibility, capacity). The Mg-MoS_2 material system exhibits complexities due to the dual ions in the electrolyte and Mos_2 phase transformation, but demonstrates the promise of pairing low cost post-Li anodes with existing, inexpensive cathode materials. We believe that slurry flow batteries, utilizing existing intercalation/conversion materials that are flowable yet in high volumetric concentrations, are a promising solution to the challenge of low cost, large scale energy storage.

6.2 Future Work

The results in this work present the design and performance of a novel Mg-MoS_2 slurry. The focus was to provide a foundation on which future work could be built upon, to further understand and optimize slurry flow battery systems. Recommended areas of future work are detailed here, to guide future research and development efforts in this field.

- Characterize agglomerate size as function of dispersion, time, and slurry composition. The slurry flow battery is based upon the formation and stability of agglomerates. Little is understood about the formation, quality, and lifetime of these agglomerates, despite their critical role in particle suspension systems. In addition, the specific pH, particle size, dispersion technique, etc. are expected to strongly affect agglomerate behavior, making generalization across heterogeneous materials systems difficult.

Characterizing the size distribution of agglomerates, ideally as temporally-resolved measurements, would allow the effects of dispersion technique, time-related particle mechanisms, and slurry composition to be understood at a finer level of detail than full cell measurements. Tracking agglomeration across the life cycle of a cell is expected to provide insight about the working principles of slurry systems, and quantify behaviors at the particle length scale. Particle size analyzers are expected to be required, due to the large scale agglomerates that are hypothesized to form within slurry electrodes.

- Explore a broader range of dispersion techniques. The fabrication of a slurry electrode was presented in this work, using probe-tip ultrasonication and homogenization to disperse the MoS_2 and KB particles in the electrolyte. There is room for broader exploration of additional dispersion techniques and parameter spaces within each technique. There is an insufficient understanding of the effects that different techniques (bath sonication, probe-tip sonication, ball milling, etc.) have on the formation of agglomerates and have on the charge/discharge capacity of slurry electrodes. The search for better dispersion techniques may also decrease the need for conductive/rheological additives, or promote higher conductivity/higher utilization particle networks. Previous works use a variety of techniques for suspension dispersion, and a comprehensive investigation including multiple techniques could greatly advance the performance and reproducibility of slurry electrode fabrication.

- Develop a model for pumping losses. Developing a deeper understanding of the effects of flow on the performance and economics of a slurry flow battery are critical to this technology's success. Pumping losses, when substantial, threaten to reduce roundtrip efficiency below levels that are economically viable. Modeling the pumping losses in a general slurry flow battery system would greatly help researchers avoid pumping schemes or slurry compositions that will result in high pumping losses, and focus efforts on strategies to minimize losses in a flow system. It is also not well understood how flow rate affects the capacity of a slurry electrode flow system. Measuring the capacity in a flow cell under continuous flow with varying flow rates would help to understand if flow is desirable for full cell performance, and would inform the pumping losses model as well.

- Ex-situ characterization of cycled cells. Preliminary cycle life studies were conducted in this work, but a more complete post-mortem analysis of cycled cells is warranted. Examining the surface properties and chemistry of the anode and separator powders after cycling, as well as the structural and electrical integrity of the separator, could provide evidence as to the degradation mechanisms at play during long term cycling in this material system. These studies could clarify the charging capacity irregularities seen in static cells undergoing high cycle life testing, and would guide changes to cell or material design in the process.

In summary, the results in this work demonstrate the use of a low cost material system in a slurry flow battery. The foundations for later slurry battery designs are laid here, as the results in this work are expected to extend to a variety of anode, electrolyte, and cathode materials in the battery literature. The high capacities exhibited by optimized slurry compositions are promising, and the characterizations begin to explore the mechanisms by which these capacities are produced. Though substantial work remains to be conducted to validate the many principles of slurry flow batteries, this work extends the material catalog for such systems into a new direction, and extends the data available on slurry electrode systems for flow batteries.

Bibliography

[1] Graeme Hoste. *Matching Hourly and Peak Demand by Combining Different Renewable Energy Sources; A case study for California in 2020*. Accessed: 7-1-2020.

[2] B. Dunn, H. Kamath, and J.-M. Tarascon. "Electrical Energy Storage for the Grid: A Battery of Choices". In: *Science* 334.6058 (Nov. 2011), pp. 928–935. DOI: 10.1126/science.1212741. URL: https://doi.org/10.1126/science.1212741.

[3] Paul Denholm et al. *Overgeneration from Solar Energy in California: A Field Guide to the Duck Chart*. Accessed: 7-1-2020.

[4] IAEA. *Non-baseload Operation in Nuclear Power Plants: Load Following and Frequency Control Modes of Flexible Operation*. Accessed: 7-1-2020.

[5] US Energy Information Administration. *EIA Glossary*. Accessed: 7-1-2020.

[6] Yujiong Gu et al. "Overall review of peak shaving for coal-fired power units in China". In: *Renewable and Sustainable Energy Reviews* 54 (Feb. 2016), pp. 723–731. DOI: 10.1016/j.rser.2015.10.052. URL: https://doi.org/10.1016/j.rser.2015.10.052.

[7] US ARPA-E. *GRIDS Program Overview*. Accessed: 7-1-2020.

[8] M. Milligan and B. Kirby. *Analysis of Sub-Hourly Ramping Impacts of Wind Energy and Balancing Area Size*. Accessed: 7-1-2020.

[9] Maria C. Argyrou, Paul Christodoulides, and Soteris A. Kalogirou. "Energy storage for electricity generation and related processes: Technologies appraisal and grid scale applications". In: *Renewable and Sustainable Energy Reviews* 94 (Oct. 2018), pp. 804–821. DOI: 10.1016/j.rser.2018.06.044. URL: https://doi.org/10.1016/j.rser.2018.06.044.

[10] T. Shigematsu. *Redox Flow Battery for Energy Storage*. Accessed: 7-1-2020.

[11] Peng Qian et al. "A novel electrode-bipolar plate assembly for vanadium redox flow battery applications". In: *Journal of Power Sources* 175.1 (Jan. 2008), pp. 613–620. DOI: 10.1016/j.jpowsour.2007.09.006. URL: https://doi.org/10.1016/j.jpowsour.2007.09.006.

[12] Minjoon Park et al. "Material design and engineering of next-generation flow-battery technologies". In: *Nature Reviews Materials* 2.1 (Nov. 2016). DOI: 10.1038/natrevmats.2016.80. URL: https://doi.org/10.1038/natrevmats.2016.80.

[13] Mihai Duduta et al. "Semi-Solid Lithium Rechargeable Flow Battery". In: *Advanced Energy Materials* 1.4 (May 2011), pp. 511–516. DOI: 10.1002/aenm.201100152. URL: https://doi.org/10.1002/aenm.201100152.

[14] Wei Wang et al. "Recent Progress in Redox Flow Battery Research and Development". In: *Advanced Functional Materials* 23.8 (Sept. 2012), pp. 970–986. DOI: 10.1002/adfm.201200694. URL: https://doi.org/10.1002/adfm.201200694.

[15] Chanyong Choi et al. "A review of vanadium electrolytes for vanadium redox flow batteries". In: *Renewable and Sustainable Energy Reviews* 69 (Mar. 2017), pp. 263–274. DOI: 10.1016/j.rser.2016.11.188. URL: https://doi.org/10.1016/j.rser.2016.11.188.

[16] M. Skyllas-Kazacos. "New All-Vanadium Redox Flow Cell". In: *Journal of The Electrochemical Society* 133.5 (1986), p. 1057. DOI: 10.1149/1.2108706. URL: https://doi.org/10.1149/1.2108706.

[17] Gareth Kear, Akeel A. Shah, and Frank C. Walsh. "Development of the all-vanadium redox flow battery for energy storage: a review of technological, financial and policy aspects". In: *International Journal of Energy Research* 36.11 (May 2011), pp. 1105–1120. DOI: 10.1002/er.1863. URL: https://doi.org/10.1002/er.1863.

[18] Liyu Li et al. "A Stable Vanadium Redox-Flow Battery with High Energy Density for Large-Scale Energy Storage". In: *Advanced Energy Materials* 1.3 (Mar. 2011), pp. 394–400. DOI: 10.1002/aenm.201100008. URL: https://doi.org/10.1002/aenm.201100008.

[19] Cong Ding et al. "Vanadium Flow Battery for Energy Storage: Prospects and Challenges". In: *The Journal of Physical Chemistry Letters* 4.8 (Apr. 2013), pp. 1281–1294. DOI: 10.1021/jz4001032. URL: https://doi.org/10.1021/jz4001032.

[20] M. Kazacos, M. Cheng, and M. Skyllas-Kazacos. "Vanadium redox cell electrolyte optimization studies". In: *Journal of Applied Electrochemistry* 20.3 (May 1990), pp. 463–467. DOI: 10.1007/bf01076057. URL: https://doi.org/10.1007/bf01076057.

[21] F Rahman and M Skyllas-Kazacos. "Solubility of vanadyl sulfate in concentrated sulfuric acid solutions". In: *Journal of Power Sources* 72.2 (Apr. 1998), pp. 105–110. DOI: 10.1016/s0378-7753(97)02692-x. URL: https://doi.org/10.1016/s0378-7753(97)02692-x.

[22] S. Eckroad. *Vanadium Redox Flow Batteries An In-Depth Analysis*. Accessed: 7-1-2020.

[23] Jianlu Zhang et al. "Effects of additives on the stability of electrolytes for all-vanadium redox flow batteries". In: *Journal of Applied Electrochemistry* 41.10 (June 2011), pp. 1215–1221. DOI: 10.1007/s10800-011-0312-1. URL: https://doi.org/10.1007/s10800-011-0312-1.

[24] Birgit Schwenzer et al. "Membrane Development for Vanadium Redox Flow Batteries". In: *ChemSusChem* 4.10 (Oct. 2011), pp. 1388–1406. DOI: 10.1002/cssc.201100068. URL: https://doi.org/10.1002/cssc.201100068.

[25] Christine Minke and Thomas Turek. "Economics of vanadium redox flow battery membranes". In: *Journal of Power Sources* 286 (July 2015), pp. 247–257. DOI: 10.1016/j.jpowsour.2015.03.144. URL: https://doi.org/10.1016/j.jpowsour.2015.03.144.

[26] Ki Jae Kim et al. "A technology review of electrodes and reaction mechanisms in vanadium redox flow batteries". In: *Journal of Materials Chemistry A* 3.33 (2015), pp. 16913–16933. DOI: 10.1039/c5ta02613j. URL: https://doi.org/10.1039/c5ta02613j.

[27] Maria Skyllas-Kazacos et al. "Recent advances with UNSW vanadium-based redox flow batteries". In: *International Journal of Energy Research* 34.2 (Nov. 2009), pp. 182–189. DOI: 10.1002/er.1658. URL: https://doi.org/10.1002/er.1658.

[28] C. Bloch et al. *Breakthrough Batteries: Powering the Era of Clean Electrification*. Accessed: 7-1-2020.

[29] Zheng Li et al. "Air-Breathing Aqueous Sulfur Flow Battery for Ultralow-Cost Long-Duration Electrical Storage". In: *Joule* 1.2 (Oct. 2017), pp. 306–327. DOI: 10.1016/j.joule.2017.08.007. URL: https://doi.org/10.1016/j.joule.2017.08.007.

[30] Jan Winsberg et al. "Redox-Flow Batteries: From Metals to Organic Redox-Active Materials". In: *Angewandte Chemie International Edition* 56.3 (Nov. 2016), pp. 686–711. DOI: 10.1002/anie.201604925. URL: https://doi.org/10.1002/anie.201604925.

[31] Xiaoliang Wei et al. "Materials and Systems for Organic Redox Flow Batteries: Status and Challenges". In: *ACS Energy Letters* 2.9 (Sept. 2017), pp. 2187–2204. DOI: 10.1021/acsenergylett.7b00650. URL: https://doi.org/10.1021/acsenergylett.7b00650.

[32] P. Leung et al. "Recent developments in organic redox flow batteries: A critical review". In: *Journal of Power Sources* 360 (Aug. 2017), pp. 243–283. DOI: 10.1016/j.jpowsour.2017.05.057. URL: https://doi.org/10.1016/j.jpowsour.2017.05.057.

[33] Rylan Dmello et al. "Cost-driven materials selection criteria for redox flow battery electrolytes". In: *Journal of Power Sources* 330 (Oct. 2016), pp. 261–272. DOI: 10.1016/j.jpowsour.2016.08.129. URL: https://doi.org/10.1016/j.jpowsour.2016.08.129.

[34] Zhi Wei Seh et al. "Designing high-energy lithium–sulfur batteries". In: *Chemical Society Reviews* 45.20 (2016), pp. 5605–5634. DOI: 10.1039/c5cs00410a. URL: https://doi.org/10.1039/c5cs00410a.

[35] Arumugam Manthiram et al. "Rechargeable Lithium–Sulfur Batteries". In: *Chemical Reviews* 114.23 (July 2014), pp. 11751–11787. DOI: 10.1021/cr500062v. URL: https://doi.org/10.1021/cr500062v.

[36] Huilin Pan et al. "On the Way Toward Understanding Solution Chemistry of Lithium Polysulfides for High Energy Li-S Redox Flow Batteries". In: *Advanced Energy Materials* 5.16 (Apr. 2015), p. 1500113. DOI: 10.1002/aenm.201500113. URL: https://doi.org/10.1002/aenm.201500113.

[37] Zhen Li et al. "Status and prospects in sulfur–carbon composites as cathode materials for rechargeable lithium–sulfur batteries". In: *Carbon* 92 (Oct. 2015), pp. 41–63. DOI: 10.1016/j.carbon.2015.03.008. URL: https://doi.org/10.1016/j.carbon.2015.03.008.

[38] Frank Y. Fan et al. "Polysulfide Flow Batteries Enabled by Percolating Nanoscale Conductor Networks". In: *Nano Letters* 14.4 (Mar. 2014), pp. 2210–2218. DOI: 10.1021/nl500740t. URL: https://doi.org/10.1021/nl500740t.

[39] Fangyi Cheng and Jun Chen. "Metal–air batteries: from oxygen reduction electrochemistry to cathode catalysts". In: *Chemical Society Reviews* 41.6 (2012), p. 2172. DOI: 10.1039/c1cs15228a. URL: https://doi.org/10.1039/c1cs15228a.

[40] Marina Bockelmann, Ulrich Kunz, and Thomas Turek. "Electrically rechargeable zinc-oxygen flow battery with high power density". In: *Electrochemistry Communications* 69 (Aug. 2016), pp. 24–27. DOI: 10.1016/j.elecom.2016.05.013. URL: https://doi.org/10.1016/j.elecom.2016.05.013.

[41] Jan grosse Austing et al. "Investigation of crossover processes in a unitized bidirectional vanadium/air redox flow battery". In: *Journal of Power Sources* 306 (Feb. 2016), pp. 692–701. DOI: 10.1016/j.jpowsour.2015.12.052. URL: https://doi.org/10.1016/j.jpowsour.2015.12.052.

[42] Xiaopeng Han et al. "Metal-Air Batteries: From Static to Flow System". In: *Advanced Energy Materials* 8.27 (Aug. 2018), p. 1801396. DOI: 10.1002/aenm.201801396. URL: https://doi.org/10.1002/aenm.201801396.

[43] S.S. Hosseiny, M. Saakes, and M. Wessling. "A polyelectrolyte membrane-based vanadium/air redox flow battery". In: *Electrochemistry Communications* 13.8 (Aug. 2011), pp. 751–754. DOI: 10.1016/j.elecom.2010.11.025. URL: https://doi.org/10.1016/j.elecom.2010.11.025.

[44] Zhaoxiang Qi and Gary M. Koenig. "Review Article: Flow battery systems with solid electroactive materials". In: *Journal of Vacuum Science & Technology B, Nanotechnology and Microelectronics: Materials, Processing, Measurement, and Phenomena* 35.4 (July 2017), p. 040801. DOI: 10.1116/1.4983210. URL: https://doi.org/10.1116/1.4983210.

[45] Irene Ruggeri, Catia Arbizzani, and Francesca Soavi. "A novel concept of Semi-solid, Li Redox Flow Air (O2) Battery: a breakthrough towards high energy and power batteries". In: *Electrochimica Acta* 206 (July 2016), pp. 291–300. DOI: 10.1016/j.electacta.2016.04.139. URL: https://doi.org/10.1016/j.electacta.2016.04.139.

[46] Syed Mubeen et al. "Solid Suspension Flow Batteries Using Earth Abundant Materials". In: *ACS Applied Materials & Interfaces* 8.3 (Jan. 2016), pp. 1759–1765. DOI: 10.1021/acsami.5b09515. URL: https://doi.org/10.1021/acsami.5b09515.

[47] Teng-Sing Wei et al. "Biphasic Electrode Suspensions for Li-Ion Semi-solid Flow Cells with High Energy Density, Fast Charge Transport, and Low-Dissipation Flow". In: *Advanced Energy Materials* 5.15 (June 2015), p. 1500535. DOI: 10.1002/aenm.201500535. URL: https://doi.org/10.1002/aenm.201500535.

[48] L. Madec et al. "Electronic vs Ionic Limitations to Electrochemical Performance in Li4Ti5O12-Based Organic Suspensions for Lithium-Redox Flow Batteries". In: *Journal of The Electrochemical Society* 161.5 (2014), A693–A699. DOI: 10.1149/2.035405jes. URL: https://doi.org/10.1149/2.035405jes.

[49] Edgar Ventosa et al. "Non-aqueous semi-solid flow battery based on Na-ion chemistry. P2-type NaxNi0.22Co0.11Mn0.66O2–NaTi2(PO4)3". In: *Chemical Communications* 51.34 (2015), pp. 7298–7301. DOI: 10.1039/c4cc09597a. URL: https://doi.org/10.1039/c4cc09597a.

[50] Mohamed Youssry et al. "Non-aqueous carbon black suspensions for lithium-based redox flow batteries: rheology and simultaneous rheo-electrical behavior". In: *Physical Chemistry Chemical Physics* 15.34 (2013), p. 14476. DOI: 10.1039/c3cp51371h. URL: https://doi.org/10.1039/c3cp51371h.

[51] H. Parant et al. "Flowing suspensions of carbon black with high electronic conductivity for flow applications: Comparison between carbons black and exhibition of specific aggregation of carbon particles". In: *Carbon* 119 (Aug. 2017), pp. 10–20. DOI: 10.1016/j.carbon.2017.04.014. URL: https://doi.org/10.1016/j.carbon.2017.04.014.

[52] Kyle C. Smith et al. "Electroactive-Zone Extension in Flow-Battery Stacks". In: *Electrochimica Acta* 147 (Nov. 2014), pp. 460–469. DOI: 10.1016/j.electacta.2014.09.108. URL: https://doi.org/10.1016/j.electacta.2014.09.108.

[53] Xiangkun Ma et al. "An optimal strategy of electrolyte flow rate for vanadium redox flow battery". In: *Journal of Power Sources* 203 (Apr. 2012), pp. 153–158. DOI: 10.1016/j.jpowsour.2011.11.036. URL: https://doi.org/10.1016/j.jpowsour.2011.11.036.

[54] Julie B. Hipp, Jeffrey J. Richards, and Norman J. Wagner. "Structure-property relationships of sheared carbon black suspensions determined by simultaneous rheological and neutron scattering measurements". In: *Journal of Rheology* 63.3 (May 2019), pp. 423–436. DOI: 10.1122/1.5071470. URL: https://doi.org/10.1122/1.5071470.

[55] Victor E. Brunini, Yet-Ming Chiang, and W. Craig Carter. "Modeling the hydrodynamic and electrochemical efficiency of semi-solid flow batteries". In: *Electrochimica Acta* 69 (May 2012), pp. 301–307. DOI: 10.1016/j.electacta.2012.03.006. URL: https://doi.org/10.1016/j.electacta.2012.03.006.

[56] Zhaoxiang Qi, Aaron L. Liu, and Gary M. Koenig. "Carbon-free Solid Dispersion LiCoO2 Redox Couple Characterization and Electrochemical Evaluation for All Solid Dispersion Redox Flow Batteries". In: *Electrochimica Acta* 228 (Feb. 2017), pp. 91–99. DOI: 10.1016/j.electacta.2017.01.061. URL: https://doi.org/10.1016/j.electacta.2017.01.061.

[57] Elena C. Montoto et al. "Redox Active Colloids as Discrete Energy Storage Carriers". In: *Journal of the American Chemical Society* 138.40 (Sept. 2016), pp. 13230–13237. DOI: 10.1021/jacs.6b06365. URL: https://doi.org/10.1021/jacs.6b06365.

[58] Zhaoxiang Qi and Gary M. Koenig. "A carbon-free lithium-ion solid dispersion redox couple with low viscosity for redox flow batteries". In: *Journal of Power Sources* 323 (Aug. 2016), pp. 97–106. DOI: 10.1016/j.jpowsour.2016.05.033. URL: https://doi.org/10.1016/j.jpowsour.2016.05.033.

[59] Chuankun Jia et al. "High–energy density nonaqueous all redox flow lithium battery enabled with a polymeric membrane". In: *Science Advances* 1.10 (Nov. 2015), e1500886. DOI: 10.1126/sciadv.1500886. URL: https://doi.org/10.1126/sciadv.1500886.

[60] Qing Wang et al. "Redox Targeting of Insulating Electrode Materials: A New Approach to High-Energy-Density Batteries". In: *Angewandte Chemie International Edition* 45.48 (Dec. 2006), pp. 8197–8200. DOI: 10.1002/anie.200602891. URL: https://doi.org/10.1002/anie.200602891.

[61] Jelle Smekens et al. "Influence of Electrode Density on the Performance of Li-Ion Batteries: Experimental and Simulation Results". In: *Energies* 9.2 (Feb. 2016), p. 104. DOI: 10.3390/en9020104. URL: https://doi.org/10.3390/en9020104.

[62] Nam Kwon, Divine Mouck-Makanda, and Katharina Fromm. "A Review: Carbon Additives in LiMnPO4- and LiCoO2-Based Cathode Composites for Lithium Ion Batteries". In: *Batteries* 4.4 (Oct. 2018), p. 50. DOI: 10.3390/batteries4040050. URL: https://doi.org/10.3390/batteries4040050.

[63] Hyun-Jung Choi et al. "Electrical percolation threshold of carbon black in a polymer matrix and its application to antistatic fibre". In: *Scientific Reports* 9.1 (Apr. 2019). DOI: 10.1038/s41598-019-42495-1. URL: https://doi.org/10.1038/s41598-019-42495-1.

[64] Shuhei Nakamura et al. "Percolation Threshold of Carbon Black-Polyethylene Composites". In: *Japanese Journal of Applied Physics* 36.Part 1, No. 8 (Aug. 1997), pp. 5163–5168. DOI: 10.1143/jjap.36.5163. URL: https://doi.org/10.1143/jjap.36.5163.

[65] Bilen Akuzum et al. "Percolation Characteristics of Conductive Additives for Capacitive Flowable (Semi-Solid) Electrodes". In: *ACS Applied Materials & Interfaces* 12.5 (Jan. 2020), pp. 5866–5875. DOI: 10.1021/acsami.9b19739. URL: https://doi.org/10.1021/acsami.9b19739.

[66] W GUOPING et al. "The effect of different kinds of nano-carbon conductive additives in lithium ion batteries on the resistance and electrochemical behavior of the LiCoO2 composite cathodes". In: *Solid State Ionics* 179.7-8 (Apr. 2008), pp. 263–268. DOI: 10.1016/j.ssi.2008.01.015. URL: https://doi.org/10.1016/j.ssi.2008.01.015.

[67] A. Narayanan et al. "Influence of electrochemical cycling on the rheo-impedance of anolytes for Li-based Semi Solid Flow Batteries". In: *Electrochimica Acta* 251 (Oct. 2017), pp. 388–395. DOI: 10.1016/j.electacta.2017.08.022. URL: https://doi.org/10.1016/j.electacta.2017.08.022.

[68] Peng-Cheng Ma et al. "Dispersion and functionalization of carbon nanotubes for polymer-based nanocomposites: A review". In: *Composites Part A: Applied Science and Manufacturing* 41.10 (Oct. 2010), pp. 1345–1367. DOI: 10.1016/j.compositesa.2010.07.003. URL: https://doi.org/10.1016/j.compositesa.2010.07.003.

[69] M. Y. Lin et al. "Universality in colloid aggregation". In: *Nature* 339.6223 (June 1989), pp. 360–362. DOI: 10.1038/339360a0. URL: https://doi.org/10.1038/339360a0.

[70] Yuan Yang, Guangyuan Zheng, and Yi Cui. "A membrane-free lithium/polysulfide semi-liquid battery for large-scale energy storage". In: *Energy & Environmental Science* 6.5 (2013), p. 1552. DOI: 10.1039/c3ee00072a. URL: https://doi.org/10.1039/c3ee00072a.

[71] Kang Dong, Shengping Wang, and Jingxian Yu. "A lithium/polysulfide semi-solid rechargeable flow battery with high output performance". In: *RSC Adv.* 4.88 (2014), pp. 47517–47520. DOI: 10.1039/c4ra08413f. URL: https://doi.org/10.1039/c4ra08413f.

[72] Paul Albertus et al. "Status and challenges in enabling the lithium metal electrode for high-energy and low-cost rechargeable batteries". In: *Nature Energy* 3.1 (Dec. 2017), pp. 16–21. DOI: 10.1038/s41560-017-0047-2. URL: https://doi.org/10.1038/s41560-017-0047-2.

[73] L. Goldie-Scot. *A Behind the Scenes Take on Lithium-ion Battery Prices*. Accessed: 7-1-2020.

[74] G. B. Haxel, J. B. Hedrick, and G. J. Orri. *Rare Earth Elements—Critical Resources for High Technology*. Accessed: 7-1-2020.

[75] Yingwen Cheng et al. "Rechargeable Mg–Li hybrid batteries: status and challenges". In: *Journal of Materials Research* 31.20 (Sept. 2016), pp. 3125–3141. DOI: 10.1557/jmr.2016.331. URL: https://doi.org/10.1557/jmr.2016.331.

[76] Markus Jäckle and Axel Groß. "Microscopic properties of lithium, sodium, and magnesium battery anode materials related to possible dendrite growth". In: *The Journal of Chemical Physics* 141.17 (Nov. 2014), p. 174710. DOI: 10.1063/1.4901055. URL: https://doi.org/10.1063/1.4901055.

[77] Rachel Davidson et al. "Formation of Magnesium Dendrites during Electrodeposition". In: *ACS Energy Letters* 4.2 (Dec. 2018), pp. 375–376. DOI: 10.1021/acsenergylett.8b02470. URL: https://doi.org/10.1021/acsenergylett.8b02470.

[78] Masaki Matsui. "Study on electrochemically deposited Mg metal". In: *Journal of Power Sources* 196.16 (Aug. 2011), pp. 7048–7055. DOI: 10.1016/j.jpowsour.2010.11.141. URL: https://doi.org/10.1016/j.jpowsour.2010.11.141.

[79] Partha Saha et al. "Rechargeable magnesium battery: Current status and key challenges for the future". In: *Progress in Materials Science* 66 (Oct. 2014), pp. 1–86. DOI: 10.1016/j.pmatsci.2014.04.001. URL: https://doi.org/10.1016/j.pmatsci.2014.04.001.

[80] Jaehee Song et al. "Mapping the Challenges of Magnesium Battery". In: *The Journal of Physical Chemistry Letters* 7.9 (Apr. 2016), pp. 1736–1749. DOI: 10.1021/acs.jpclett.6b00384. URL: https://doi.org/10.1021/acs.jpclett.6b00384.

[81] Jun Lu et al. "High-Performance Anode Materials for Rechargeable Lithium-Ion Batteries". In: *Electrochemical Energy Reviews* 1.1 (Mar. 2018), pp. 35–53. DOI: 10.1007/s41918-018-0001-4. URL: https://doi.org/10.1007/s41918-018-0001-4.

[82] Min-Sik Park et al. "Recent Advances in Rechargeable Magnesium Battery Technology: A Review of the Field's Current Status and Prospects". In: *Israel Journal of Chemistry* 55.5 (Mar. 2015), pp. 570–585. DOI: 10.1002/ijch.201400174. URL: https://doi.org/10.1002/ijch.201400174.

[83] Qirong Liu et al. "Multi-ion strategies towards emerging rechargeable batteries with high performance". In: *Energy Storage Materials* 23 (Dec. 2019), pp. 566–586. DOI: 10.1016/j.ensm.2019.03.028. URL: https://doi.org/10.1016/j.ensm.2019.03.028.

[84] Yanliang Liang et al. "Interlayer-Expanded Molybdenum Disulfide Nanocomposites for Electrochemical Magnesium Storage". In: *Nano Letters* 15.3 (Mar. 2015), pp. 2194–2202. DOI: 10.1021/acs.nanolett.5b00388. URL: https://doi.org/10.1021/acs.nanolett.5b00388.

[85] Minglei Mao et al. "A critical review of cathodes for rechargeable Mg batteries". In: *Chemical Society Reviews* 47.23 (2018), pp. 8804–8841. DOI: 10.1039/c8cs00319j. URL: https://doi.org/10.1039/c8cs00319j.

[86] Lihua Chen et al. "Electrochemical Stability Window of Polymeric Electrolytes". In: *Chemistry of Materials* 31.12 (May 2019), pp. 4598–4604. DOI: 10.1021/acs.chemmater.9b01553. URL: https://doi.org/10.1021/acs.chemmater.9b01553.

[87] Pallavi Verma, Pascal Maire, and Petr Novák. "A review of the features and analyses of the solid electrolyte interphase in Li-ion batteries". In: *Electrochimica Acta* 55.22 (Sept. 2010), pp. 6332–6341. DOI: 10.1016/j.electacta.2010.05.072. URL: https://doi.org/10.1016/j.electacta.2010.05.072.

[88] Ran Attias et al. "Anode-Electrolyte Interfaces in Secondary Magnesium Batteries". In: *Joule* 3.1 (Jan. 2019), pp. 27–52. DOI: 10.1016/j.joule.2018.10.028. URL: https://doi.org/10.1016/j.joule.2018.10.028.

[89] Adam Z. Weber et al. "Redox flow batteries: a review". In: *Journal of Applied Electrochemistry* 41.10 (Sept. 2011), pp. 1137–1164. DOI: 10.1007/s10800-011-0348-2. URL: https://doi.org/10.1007/s10800-011-0348-2.

[90] Tao Gao et al. "Hybrid Mg2/LiBattery with Long Cycle Life and High Rate Capability". In: *Advanced Energy Materials* 5.5 (Nov. 2014), p. 1401507. DOI: 10.1002/aenm.201401507. URL: https://doi.org/10.1002/aenm.201401507.

[91] Hyun Deog Yoo et al. "High Areal Capacity Hybrid Magnesium–Lithium-Ion Battery with 99.9% Coulombic Efficiency for Large-Scale Energy Storage". In: *ACS Applied Materials & Interfaces* 7.12 (Mar. 2015), pp. 7001–7007. DOI: 10.1021/acsami.5b01206. URL: https://doi.org/10.1021/acsami.5b01206.

[92] Lamuel David, Romil Bhandavat, and Gurpreet Singh. "MoS2/Graphene Composite Paper for Sodium-Ion Battery Electrodes". In: *ACS Nano* 8.2 (Jan. 2014), pp. 1759–1770. DOI: 10.1021/nn406156b. URL: https://doi.org/10.1021/nn406156b.

[93] Jie Xiao et al. "Exfoliated MoS2Nanocomposite as an Anode Material for Lithium Ion Batteries". In: *Chemistry of Materials* 22.16 (Aug. 2010), pp. 4522–4524. DOI: 10.1021/cm101254j. URL: https://doi.org/10.1021/cm101254j.

[94] Ibrahim Saana Amiinu et al. "Multifunctional Mo-N/C@MoS2 Electrocatalysts for HER, OER, ORR, and Zn-Air Batteries". In: *Advanced Functional Materials* 27.44 (Sept. 2017), p. 1702300. DOI: 10.1002/adfm.201702300. URL: https://doi.org/10.1002/adfm.201702300.

[95] Xin Fan et al. "A Hybrid Mg2/Li Battery Based on Interlayer-Expanded MoS2 /Graphene Cathode". In: *Advanced Energy Materials* 7.19 (May 2017), p. 1700317. DOI: 10.1002/aenm.201700317. URL: https://doi.org/10.1002/aenm.201700317.

[96] Zhanyu Li et al. "Rechargeable Aluminum-Ion Battery Based on MoS2 Microsphere Cathode". In: *ACS Applied Materials & Interfaces* 10.11 (Feb. 2018), pp. 9451–9459. DOI: 10.1021/acsami.8b00100. URL: https://doi.org/10.1021/acsami.8b00100.

[97] Tyler Stephenson et al. "Lithium ion battery applications of molybdenum disulfide (MoS2) nanocomposites". In: *Energy Environ. Sci.* 7.1 (2014), pp. 209–231. DOI: 10.1039/c3ee42591f. URL: https://doi.org/10.1039/c3ee42591f.

[98] Cheng-Jui Hsu et al. "MoS2/graphene cathodes for reversibly storing Mg2 and Mg2/Li in rechargeable magnesium-anode batteries". In: *Chemical Communications* 52.8 (2016), pp. 1701–1704. DOI: 10.1039/c5cc09407k. URL: https://doi.org/10.1039/c5cc09407k.

[99] Mingxiao Ye et al. "Recent Advancement on the Optical Properties of Two-Dimensional Molybdenum Disulfide (MoS2) Thin Films". In: *Photonics* 2.1 (Mar. 2015), pp. 288–307. DOI: 10.3390/photonics2010288. URL: https://doi.org/10.3390/photonics2010288.

[100] M. A. Py and R. R. Haering. "Structural destabilization induced by lithium intercalation in MoS2 and related compounds". In: *Canadian Journal of Physics* 61.1 (Jan. 1983), pp. 76–84. DOI: 10.1139/p83-013. URL: https://doi.org/10.1139/p83-013.

[101] Oren Mizrahi et al. "Electrolyte Solutions with a Wide Electrochemical Window for Rechargeable Magnesium Batteries". In: *Journal of The Electrochemical Society* 155.2 (2008), A103. DOI: 10.1149/1.2806175. URL: https://doi.org/10.1149/1.2806175.

[102] Xiaowei Miao et al. "Electrospun V 2 MoO 8 as a cathode material for rechargeable batteries with Mg metal anode". In: *Nano Energy* 34 (Apr. 2017), pp. 26–35. DOI: 10.1016/j.nanoen.2017.02.014. URL: https://doi.org/10.1016/j.nanoen.2017.02.014.

[103] Jae-Hyun Cho et al. "Controlling the Intercalation Chemistry to Design High-Performance Dual-Salt Hybrid Rechargeable Batteries". In: *Journal of the American Chemical Society* 136.46 (Nov. 2014), pp. 16116–16119. DOI: 10.1021/ja508463z. URL: https://doi.org/10.1021/ja508463z.

[104] Ye Zhang et al. "Dual-Salt Mg-Based Batteries with Conversion Cathodes". In: *Advanced Functional Materials* 25.47 (Nov. 2015), pp. 7300–7308. DOI: 10.1002/adfm.201503639. URL: https://doi.org/10.1002/adfm.201503639.

[105] Albert L. Lipson et al. "Practical Stability Limits of Magnesium Electrolytes". In: *Journal of The Electrochemical Society* 163.10 (2016), A2253–A2257. DOI: 10.1149/2.0451610jes. URL: https://doi.org/10.1149/2.0451610jes.

[106] Yingwen Cheng et al. "Electrochemically stable cathode current collectors for rechargeable magnesium batteries". In: *J. Mater. Chem. A* 2.8 (2014), pp. 2473–2477. DOI: 10.1039/c3ta15113a. URL: https://doi.org/10.1039/c3ta15113a.

[107] Lion Speciality Chem. *KETJENBLACK Highly Electro-Conductive Carbon Black*. Accessed: 7-1-2020.

[108] Celgard LLC. *Celgard High Performance Battery Separators*. Accessed: 7-1-2020.

[109] Yanliang Liang et al. "Rechargeable Mg Batteries with Graphene-like MoS2 Cathode and Ultrasmall Mg Nanoparticle Anode". In: *Advanced Materials* 23.5 (Dec. 2010), pp. 640–643. DOI: 10.1002/adma.201003560. URL: https://doi.org/10.1002/adma.201003560.

[110] Yongchang Liu, Li-Zhen Fan, and Lifang Jiao. "Graphene intercalated in graphene-like MoS 2 : A promising cathode for rechargeable Mg batteries". In: *Journal of Power Sources* 340 (Feb. 2017), pp. 104–110. DOI: 10.1016/j.jpowsour.2016.11.060. URL: https://doi.org/10.1016/j.jpowsour.2016.11.060.

[111] Thermo Fisher Scientific. *Labware Chemical Resistance Table*. Accessed: 7-1-2020.

[112] Eihab Jaber et al. "Network formation in polymer nanocomposites under shear". In: *Soft Matter* 7.8 (2011), p. 3852. DOI: 10.1039/c0sm00990c. URL: https://doi.org/10.1039/c0sm00990c.

[113] Aditya Narayanan, Frieder Mugele, and Michael H. G. Duits. "Mechanical History Dependence in Carbon Black Suspensions for Flow Batteries: A Rheo-Impedance Study". In: *Langmuir* 33.7 (Feb. 2017), pp. 1629–1638. DOI: 10.1021/acs.langmuir.6b04322. URL: https://doi.org/10.1021/acs.langmuir.6b04322.

[114] C.L Barrie et al. "Rheology of aqueous carbon black dispersions". In: *Journal of Colloid and Interface Science* 272.1 (Apr. 2004), pp. 210–217. DOI: 10.1016/j.jcis.2003.12.004. URL: https://doi.org/10.1016/j.jcis.2003.12.004.

[115] Yuzi Zhang, Joseph P. Sullivan, and Arijit Bose. "Rheological and microstructural characterization of aqueous suspensions of carbon black and reduced graphene oxide". In: *Colloids and Surfaces A: Physicochemical and Engineering Aspects* 592 (May 2020), p. 124591. DOI: 10.1016/j.colsurfa.2020.124591. URL: https://doi.org/10.1016/j.colsurfa.2020.124591.

[116] Jordi Jacas Biendicho et al. "Static and Dynamic Studies on LiNi1/3Co1/3Mn1/3O2-Based Suspensions for Semi-Solid Flow Batteries". In: *ChemSusChem* 9.15 (June 2016), pp. 1938–1944. DOI: 10.1002/cssc.201600285. URL: https://doi.org/10.1002/cssc.201600285.